UNIVERSITY OF OXFORD

The dosimetry of small, megavoltage photon fields: correction factors, dose area products and detector designs

by

Tracy Underwood

A thesis submitted in partial fulfillment for the
degree of Doctor of Philosophy

in the
Gray Institute for Radiation Oncology and Biology
Medical Sciences Division

April 2013

UNIVERSITY OF OXFORD

Abstract

Gray Institute for Radiation Oncology and Biology
Medical Sciences Division

Doctor of Philosophy

by Tracy Underwood

In recent years, small fields have come to play a key role in advanced radiotherapy, yet protocols to perform dosimetry under small field conditions are still in their infancy. In 2008, the IAEA and AAPM published a formalism [Med. Phys. 35, 5179-5186] recommending the use of point-dose correction factors. This thesis uses Monte Carlo simulations to demonstrate that the values of these correction factors depend strongly on both detector design and field size, as well as other variables such as detector off-axis position and detector azimuthal angle.

Mass density is found to be the principal determinant of detector water non-equivalence. Furthermore, it is shown that it is possible to compensate for the mass-density of a detector cavity by incorporating additional components of contrasting mass-density into that detector's design. For small cavities, such design modifications enable the detector's small- to large- field response ratio to be matched to that of a "point-like" water-structure: ideal detector performance can be achieved across a variety of irradiation conditions.

For existing commercial detectors, a Dose Area Product (DAP) formalism is also developed and shown to be much more robust than the point-dose correction factor approach.

In conclusion, correction factor values for existing detector designs depend on a host of variables and their calculation typically relies on the use of time-intensive Monte Carlo methods. This thesis indicates that future moves towards density-compensated detector designs or DAP-based protocols can simplify the methodology of small field dosimetry.

Acknowledgements

My deepest gratitude goes to my supervisors: Dr Mark Hill, who has been there all along; Dr Helen Winter, who gave up her Saturdays and always allowed me to make "one more measurement"; and Dr John Fenwick who has provided the vision, the challenge and often the answer. They have given me much of their valuable time and have shown me kindness in abundance.

My thanks also go to Dr Alison Scott for useful discussions and to my examiners, Dr Hugo Palmans and Dr Mike Partridge, for their detailed comments. Jamie Thompson and Thiru Natarajan kindly assisted with aspects of the experimental work, and Ernesto Mainegra-Hing, Frédéric Tessier (both of EGSnrc) and Jörg Wulff provided me with invaluade software advice.

From day one, Dr Claire Timlin and Dr Wilson welcomed me with such kindness. My sincere gratitude also goes to Prof Bleddyn Jones. It was great to share the DPhil experience with Dan Warren and Daniel Abler. Thanks to Prof Ken Peach for supporting us all and to Prof Roger Dale for his advice and encouragement over the years.

I would like to acknowledge the MRC and Cancer Research UK for funding my studentship. The computationally intensive simulations described in this thesis were made possible by the Oxford Supercomputing Centre and the IRIDIS HPC facility (provided by the e-Infrastructure South Centre for Innovation).

With my friends in the RRI - Sara Hackett, Sam Warren, Nadia Falzone, Dan McGowan and Dan Liu - there is never a dull day. I will miss them all. The encouragement of my Dad, my Mum, Sis and Michael has long been my elixir and without it I wouldn't have contemplated this course. And of course thanks to Ben, for eveything.

Tsz, you remain an inspiration and as I leave Oxford I think of you.

Contents

Abbreviations

AAPM	**A**merican **A**ssociation of **P**hysicists in **M**edicine
BIPM	**B**ureau **I**nternational des **P**oids et **M**esures
CAM	**C**losest **A**pproach **M**etric
CPE	**C**harged **P**article **E**quilibrium
CSDA	**C**ontinuous **S**lowing **D**own **A**pproximation
CT	**C**omputed **T**omography
DAP	**D**ose **A**rea **P**roduct
DCA	**D**istance of **C**losest **A**pproach
DLP	**D**ose **L**ength **P**roduct
FWHM	**F**ull **W**idth **H**alf **M**aximum
GBBS	**G**rid **B**ased **B**oltzmann **S**olvers
IAEA	**I**nternational **A**tomic **E**nergy **A**gency
IMRT	**I**ntensity **M**odulated **R**adiation **T**herapy
IPEM	**I**nstitute of **P**hysics and **E**ngineering in **M**edicine
LEE	**L**ateral **E**lectronic **E**quilibrium
LBTE	**L**inear **B**oltzmann **T**ransport **E**quations
MC	**M**onte **C**arlo
MLC	**M**ulti **L**eaf **C**ollimator
MOF	**M**easurement **O**utput **F**actor
MSR	**M**achine **S**pecific **R**eference
MU	**M**ontitor **U**nits
NPL	**N**ational **P**hysical **L**aboratory
PSDL	**P**rimary **S**tandards **D**osimetry **L**aboratory
QC	**Q**uality **C**ontrol
SBRT	**S**tereoractic **B**ody **R**adiation **T**herapy
SRS	**S**tereotactic **R**adiation **S**urgery
SSD	**S**ource to **S**urface **D**istance
TPS	**T**reatment **P**lanning **S**ystem

Chapter 1

Introduction

Over recent decades, developments in medical imaging and accelerator technology have led to improvements in the physical accuracy and precision of radiotherapy. Traditionally, radiotherapy treatment fields ranged from $4\times4\,\mathrm{cm}^2$ to $40\times40\,\mathrm{cm}^2$ but modern machines are able to generate radiation beams with sub-centimetre widths. These beams can be used to (i) conform radiation dose-distributions more tightly to tumour shapes, minimising radiation doses delivered to normal tissues, and (ii) treat smaller early-diagnosed lesions. Fields of size $3\times3\,\mathrm{cm}^2$ or smaller are now employed by a host of radiotherapy modalities and machines. Two broad classes of technique where they are found can be defined: stereotactic radiotherapies and intensity-modulated radiotherapies (see Table 1.1).

It is the role of the clinical physicist to ensure that, as new techniques are developed, accurate knowledge of the dose delivered to the patient is maintained. Due to the sigmoidal shape of dose-response curves for both tumours and normal tissues, relatively small errors in dosimetry can lead to serious (i) underdosage of the tumour, or (ii) normal tissue complications.

However, for many modern treatment scenarios (particularly ones which use small radiation fields) the implementation of dosimetry is a challenging task. A small field scenario may be defined [1] as one in which:

1. source occlusion occurs: from the detector's eye view the primary photon source is partially shielded. Overlapping penumbra mean that measurement of the full width half maximum (FWHM) gives a wider field than expected according to the collimator opening due to a reduction in central axis dose. And/or
2. lateral electronic equilibrium does not hold in the vicinity of the detector sensitive cavity

Intensity Modulated Radiation Therapy In IMRT, non-uniform fields are composed of many small elementary fields (beamlets).	**Static gantry:** typically 5-7 fixed beam-angles are employed. The treatment is delivered by a conventional clinical linac using small tungsten Multi-Leaf Collimators (MLCs), with a minimum leaf width of ∼5 mm. These MLCs either collimate the radiation by operating dynamically throughout the beam-on period, or the beam is turned off whilst the MLCs move, so that dose is delivered in a "step-and-shoot" fashion.
	Arc-based: here a conventional linac is used, but the leaves of the MLC move and the dose rate / gantry speed is varied as the gantry rotates, such that the IMRT is delivered over a continuous arc of beam angles.
	Helical tomotherapy: in tomotherapy units a linear accelerator is combined with a ring gantry to produce a unit capable of delivering megavoltage radiotherapy and obtaining megavoltage CT scans (for both pre-treatment patient set-up and *in-vivo* dosimetric verification). A fan beam of width 40 cm is collimated by a tungsten MLC system where each leaf is either closed or open. Additional collimating jaws can limit the slice thickness to 5 mm. As the ring gantry rotates, the patient is translated through the treatment unit. The 360° beam delivery employs thousands of targeted beamlets so that a highly conformal helical delivery pattern is achieved.
Stereotactic Radiotherapies combine a small target volume with very accurate and precise delivery techniques. Hypofractionation is employed (typically using 1-5 fractions).	**Static gantry:** here a conventional linac is employed, but Stereotactic Radiation Surgery (SRS) / Stereotactic Body Radiation Therapy (SBRT) fields may be defined either using standard linac MLCs, 'microMLCs' or fixed beam applicators.
	Helical tomotherapy: as described in the IMRT section above.
	Gamma Knife: the latest Gamma Knife model (Perfexion) consists of 192 cobalt-60 sources arranged in a cylindrical configuration in five concentric rings. These sources are distributed over eight sectors, each of which can move independently across three different collimators producing beams of isocentric diameter 4, 8, or 16 mm. The sources in a given sector may also be blocked entirely. Depending on the size and shape of the target volume, appropriate collimation is used for each "shot" (isocentre position). Multiple shots together form the complete dose plan.
	Cyberknife: here a MV linac is mounted on a flexible robotic arm. Typical treatments use several hundred beam directions (from a choice of almost 2000).

TABLE 1.1: Summary of radiotherapy modalities which may utilise small fields / fields exhibiting non-equilibrium conditions

Detectors designed for conventional large field scenarios (such as Farmer ionisation chambers, with sensitive volume dimensions >10 mm) are of limited value in small field scenarios: electronic disequilibrium across their large cavities renders their readings unrepresentative. As an example, between April 2006 and April 2007, 145 French patients were found to have experienced systematic misadministration of their head and neck SRS due to inappropriate usage of Farmer chambers [2]. All patients were treated using a newly set-up radiosurgery service where dosimetric measurements for a $6\times6\,mm^2$ field were performed using a Farmer chamber with sensitive volume 23 mm long: *i.e.* the detector's sensitive volume spanned an area much larger than the homogeneous part of the beam profile. As a consequence, the dose measured was smaller than the true dose on the beam axis, leading to an overestimation of the number of linac monitor units to be delivered for a given prescribed dose (and consequently, patient overdosage).

In the case of the French incident, a particularly inappropriate dosimeter was used in the commissioning of a stereotactic radiotherapy treatment unit. But even the sensitive volumes of detectors designed for stereotactic radiotherapy dosimetry typically have widths of ∼2 mm and measurements of heterogeneous dose distributions are consequently averaged over these finite sensitive volumes, a potentially serious issue. Furthermore, many detector components (sensitive volumes, electrodes and casings) perturb the lateral scatter of electrons on a scale that can substantially bias dose measurements in very small fields.

The optimal strategy to avoid dosimetric errors in small field therapies would be to commission each radiotherapy treatment planning system with experimental data obtained using (i) a dosimeter with very high spatial resolution and (ii) a robust, internationally accepted Code of Practice to account for the dosimeter's remaining perturbative effects and link its output back to that of a primary standard[1] at a National Standards Laboratory. In Spring 2013, neither of these ideals are yet available. This thesis examines current small field dosimetric practice and analyses the potential for improvements in both dosimeter and protocol design.

The remainder of this chapter is divided into two introductory sections (specific to megavoltage photon radiotherapy) which describe:

1. The physics of dose deposition
2. Clinical dosimetric practice

[1] Primary standards provide the reference absorbed dose unit without any previous calibration, i.e. by absolute measurement. They must be verified internationally through comparisons with similar instruments at (i) the BIPM, an international laboratory set up under the Metre Convention of 1875, or (ii) other Primary Standard Dosimetry Laboratories (PSDLs).

1.1 The physics of dose deposition in photon radiotherapy

In the UK, external beam radiotherapy typically employs photon beams with nominal energies 6-15 MV[2]. The most commonly used nominal beam energy (and therefore the focus of this work) is 6 MV. A photon energy spectrum for such a beam is included as Figure 1.1.

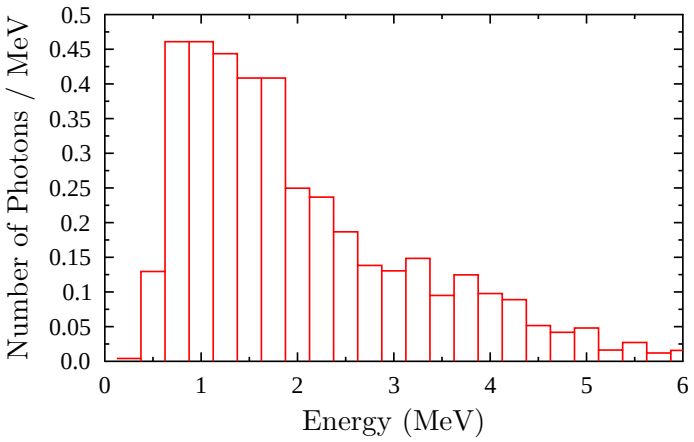

FIGURE 1.1: Photon energy spectra for a 6 MV beam from a Varian Clinac ($10\times10\,cm^2$ field) Data from Mohan *et al.*[3].

Such a beam transfers energy to matter in a two stage process:

1. the photons liberate charged particles mainly via Compton scattering, the photo-electric effect and pair production (as outlined in Table 1.2).

2. the resultant charged particles impart energy to matter via collisional and radiative losses (as outlined in Table 1.3).

[2]The nominal energy is the approximate energy of electrons incident on the target of the linac where the photon beam is generated via bremsstrahlung.

Photon interaction process	**Charged particles liberated**
Elastic scattering: in Thomson and Rayleigh scattering the photon is elastically scattered from a single atomic electron or an ensemble of atomic electrons respectively. Nuclear Thomson scattering can also occur.	None
Photo-excitation: here the photon is absorbed by an atom, exciting that atom to a higher state (this effect resonates at photon energies corresponding to atomic transitions).	An Auger electron may be emitted
Photo-electric effect: the photon is absorbed by an atom which expels an electron 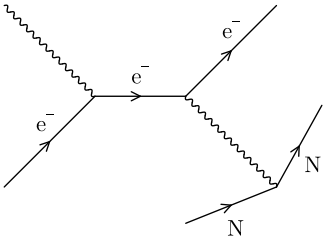	An electron
Compton scattering: here the photon scatters from an electron. The electron recoils and carries off a fraction of the photon's energy. A scattered photon also leaves the interaction with reduced energy. 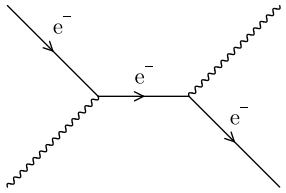	An electron
Pair production: photons with energy greater than twice the rest mass of an electron may create an electron and positron pair in the field of a nucleus (which absorbs surplus momentum). 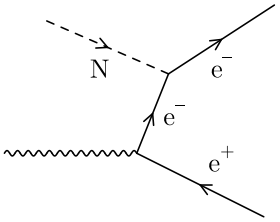	An electron / positron pair

TABLE 1.2: Main photon interaction processes (for more information on photon interaction processes, see Chapter 4 of reference [4].)

Collisional Interactions	here charged particles interact with atomic electrons: energy is dissipated as ionisation/excitation in or near the original charged particle track. Most interactions involve small energy losses in line with the Continuous Slowing Down Approximation (CSDA). In some cases, collisional interactions result in δ-rays: secondary electrons with sufficient energy to leave the immediate vicinity of the original track and produce distinguishable tracks of their own.
Radiative Interactions	here charged particles interact with atomic nuclei: (i) x-ray photons (bremsstrahlung or "braking radiation") are emitted as the charged particle decelerates, (ii) photons are emitted during positron annihilation or (iii) photons are emitted during fluorescence. In all cases, the emitted photons are relatively penetrating compared to electrons and carry their energy far away from the original charged particle track.
	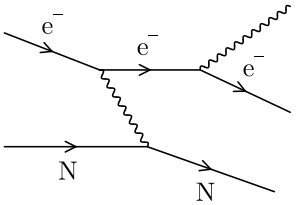 Bremsstrahlung
	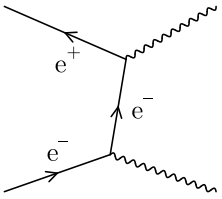 e^-/e^+ annihilation

TABLE 1.3: The two classes of charged particle interaction [5].

1.1.1 Energy transfer stage 1: kerma

The first of these stages may be described by a quantity called kerma, an acronym for Kinetic Energy Released per unit MAss. It considers the expectation value of the kinetic energy transferred from neutral particles to charged particles in a volume of material of mass dm:

$$K = \frac{\mathrm{d}\overline{E_{\mathrm{tr}}}}{\mathrm{d}m} \tag{1.1}$$

Kerma can be formulated in terms of the energy-transfer coefficient of the medium and the photon fluence, as outlined in Figure 1.2. Figure 1.2 also demonstrates how kerma can be partitioned into two components [4]:

$$K = K^{\mathrm{col}} + K^{\mathrm{rad}} \tag{1.2}$$

In low atomic number materials (including air, water and soft tissue) the majority of electrons liberated by the photon beam will dissipate their energy through inelastic collisions with atomic electrons, but some will instead be involved in radiative interactions

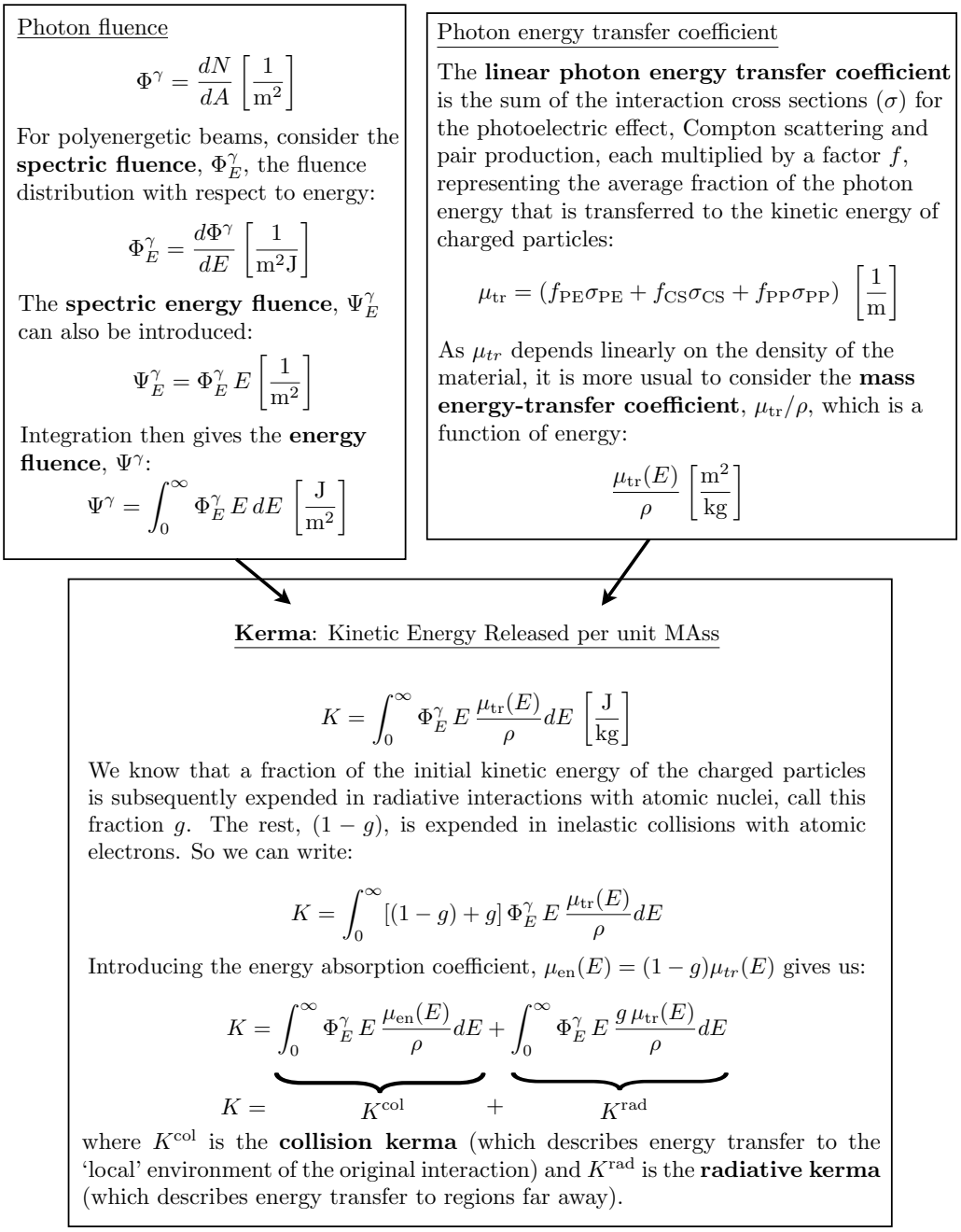

FIGURE 1.2: Mathematical formulation of photon energy transfers per unit mass.

with atomic nuclei. Energy described by the **collisional** component K^{col} will typically be deposited in the "local" environment of the original interaction, while the **radiative** energy (described by K^{rad}) will be deposited far away. The fraction of energy expended in radiative interactions, g, is small (≈0.3% for 1 MeV photons, rising to ≈0.4% for 10 MeV photons in water [6]).

1.1.2 Energy transfer stage 2: collisional and radiative losses → absorbed dose

In photon radiotherapy, the physical parameter most widely linked to biological effect is 'absorbed dose': the mean energy absorbed per unit mass by an elementary volume.

$$D = \frac{d\bar{\epsilon}}{dm} \tag{1.3}$$

1.1.2.1 The relationship between kerma and absorbed dose

Both kerma and absorbed dose are measured in Gray [J/kg]. However, unlike kerma, absorbed dose cannot be determined directly from photon fluence:

> "Absorbed dose is the energy imparted per unit mass in the neighbourhood of a point by electrons arising in the entire volume from which electrons can reach the point. Since absorbed dose can depend on the photon fluence throughout that volume, it is in general not uniquely determined by the photon fluence at the point [7]."

At a single point, let β be the quotient of absorbed dose and K^{col} [7]:

$$\beta = D/K^{\text{col}} \tag{1.4}$$

Equation 1.4 formulates absorbed dose in terms of collision kerma, rather than total kerma, as it is assumed that energy expended to radiative photons (in the form of radiative kerma) escapes the region of interest.

Three cases can then be defined [7]:

$\beta < 1$ this occurs near the entrance surface when a broad photon beam enters a new medium (e.g. water) from air. **It also occurs for small photon fields with diameters less than the maximum electron range in the medium.**

$\beta = 1$ if a photon beam were to undergo zero attenuation, this condition would exist at depths greater than the maximum electron range. This state is known as **Charged Particle Equilibrium** (CPE).

$\beta > 1$ In reality, complete CPE does not occur, but at depths greater than one maximum electron range there will exist a region of transient CPE. Here the effects of beam attenuation and electron forward scatter combine to result in $\beta > 1$.

1.1.2.2 The relationship between charged particle fluence and absorbed dose

Let us now shift our focus away from the original photons and their associated kerma, to the liberated charged particles. Restricting ourselves once again to collision interactions, energy losses per unit path length are described by the linear stopping power $S = dE/dx$. Some collisional energy is transferred to δ-rays which will transport energy outside the region of interest, but under the condition of δ-ray equilibrium, dose can be obtained from charged particle fluence and medium stopping power, as outlined in Figure 1.3.

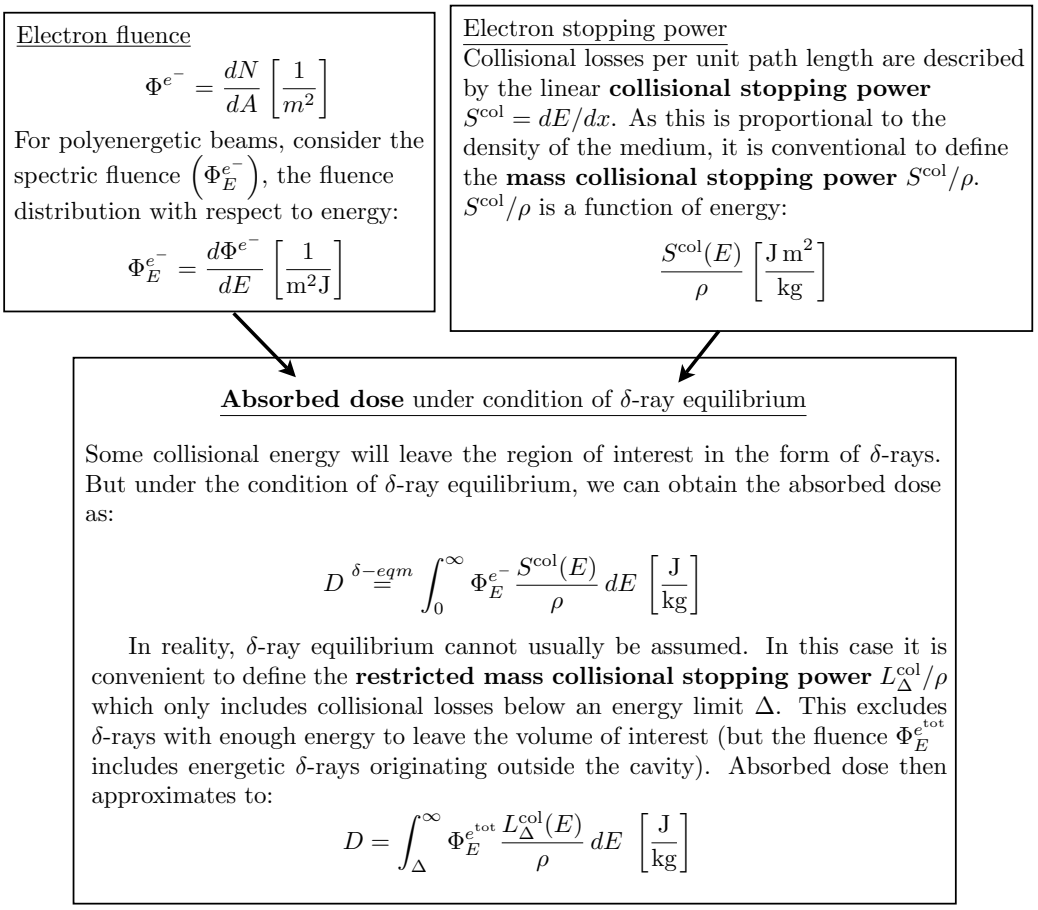

FIGURE 1.3: Charged particle transfers per unit mass (in actuality, the term 'electron' should be taken to encompass both electrons and positrons).

From Figure 1.3, it is worth emphasising that, under the condition of δ-ray equilibrium, absorbed dose is obtained as:

$$D = \int_0^\infty \Phi_{\mathrm{E}}^{e^-} \frac{S^{\mathrm{col}}(E)}{\rho}\, dE \tag{1.5}$$

ICRU report 37 [8] defines the mass collisional stopping power for electrons and positrons as:

$$\frac{S^{\text{col}}(E)}{\rho} = \frac{2\pi {r_e}^2 mc^2}{u}\frac{1}{\beta^2}\frac{Z}{A}\left[\ln(T/I)^2 + \ln(1+\tau/2) + F^{\pm}(\tau) - \delta\right] \tag{1.6}$$

where

r_e	classical electron radius
mc^2	electron rest energy
u	atomic mass unit
β	velocity of the incident electron/positron relative to the speed of light
Z	atomic number of medium
A	atomic weight of medium
I	mean excitation value of medium (derived experimentally *e.g.* using range measurements in proton beams)
T	kinetic energy of electron/positron
$F^{\pm}$	an auxiliary function for electrons (-) and positrons (+) $F^{-}(\tau) = (1-\beta^2)\left[1 + \tau^2/8 - (2\tau+2)\ln 2\right]$ $F^{+}(\tau) = 2\ln 2 - (\beta^2/12)\left[23 + 14(\tau+2) + 10/(\tau+2)^2 + 4/(\tau+2)^3\right]$
τ	$\tau = T/mc^2$
δ	density-effect correction: as a charged particle passes through a medium, it causes that medium to become polarised, which in turn decreases the electromagnetic field acting on the particle so that its stopping power is reduced. The strength of this effect depends on the density of the medium. Values for this parameter may be obtained using the ESTAR computer code, accessed via http://physics.nist.gov/PhysRefData/Star/Text/ESTAR.html

1.2 Clinical dosimetry

The ICRU state that in clinical radiotherapy the dose applied to the tumour should be within -5% and +7% of the prescribed dose [9][3]. The delivered dose will be subject to uncertainties in a host of areas, including the calculation algorithms which model dose based on each patient's CT scan, patient set-up and motion plus daily linac output-variation. This thesis focuses on uncertainties in the reference and relative stages of the dosimetry chain (Figure 1.4). Analysis suggests that an accuracy of ~3% is required across the dosimetric chain to yield ~5% accuracy in the dose delivered to the patient [10–12]. For very small ($0.5 \times 0.5\,\text{cm}^2$) fields, dosimetric results obtained using different

[3] An asymmetric range being used to account for the fact that under-dosage can prove critical in terms of tumour control probability.

detectors (ion chambers, diodes and diamond detectors) can vary by tens of percent, even for sensitive volumes of 1-3 mm diameter [13–16].

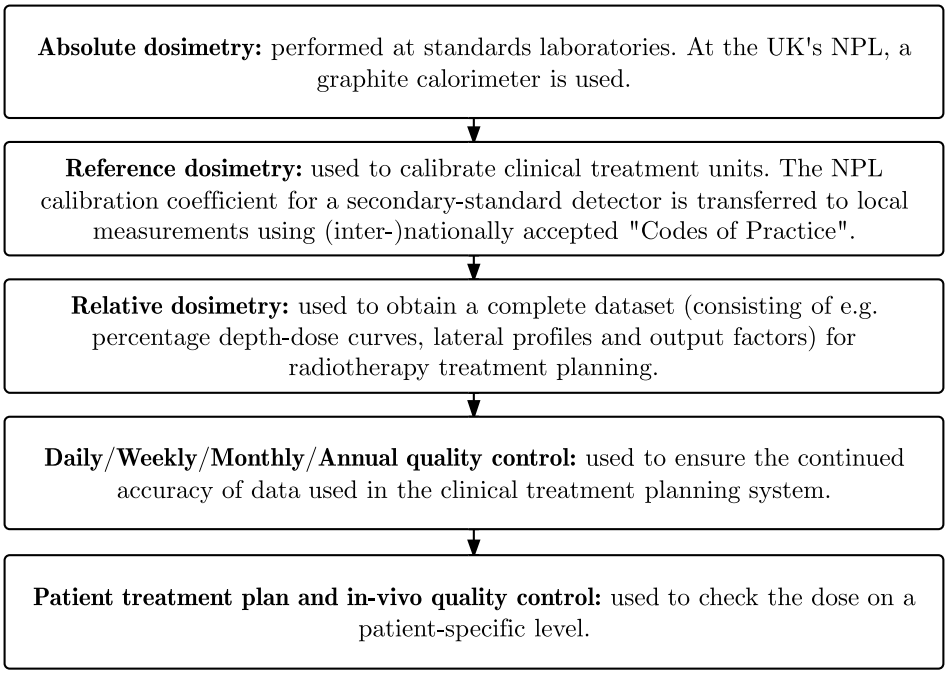

FIGURE 1.4: The implementation of various forms of dosimetry in clinical radiotherapy.

1.2.1 Reference dosimetry

1.2.1.1 Dose to air

Reference dosimetry (used to calibrate clinical linacs) is performed under broad-field conditions which exhibit charged particle equilibrium. This form of dosimetry uses air-filled ionisation chambers known to exhibit long-term stability and reproducibility in their response.

The dose to an air-filled cavity $D_{\text{cav}}(Q)$, can be obtained as [4]:

$$D_{\text{cav}}(Q) = \left[\frac{Q_{\text{ion}}}{\rho V} \cdot \frac{W_{\text{air}}}{e}\right]_{\text{Q}} \tag{1.7}$$

where Q_{ion} is the total charge measured, ρ is the density of the air, V is the volume of the cavity and $\frac{W_{\text{air}}}{e}$ is the mean energy expended in air per ion pair formed[4].

[4] W_{air}/e=33.97 J C^{-1} [4].

However, in radiotherapy we are more interested in the dose to a point in the undisturbed medium (usually water, a good tissue surrogate and a medium in which measurements can be easily performed). We can write:

$$f(Q) = \left(\frac{D_{\text{wat}}}{D_{\text{cav}}}\right)_Q \tag{1.8}$$

and

$$D_{\text{wat}}(Q) = D_{\text{cav}}(Q) \cdot f(Q) \tag{1.9}$$

where the proportionality constant f (dependent on the beam quality, Q) may be determined using cavity theories. Different theories have been developed for different cavity sizes, cavity size being characterised relative to the range of secondary electrons. Here we focus on the Bragg-Gray and Spencer-Attix-Nahum theories for small cavities.

1.2.1.2 Bragg-Gray and Spencer-Attix-Nahum cavity theories

The Bragg-Gray cavity theory considers the case where [4, 5]:

1. the cavity is sufficiently small compared to the range of electrons crossing it that it does not perturb the fluence of charged particles (including its distribution in energy) in the medium
2. the absorbed dose is deposited entirely by charged particles crossing the cavity

This means that the electron fluence Φ_{E}^{e-} will be the same for both media. Assuming either that (i) the δ-ray range is negligible compared to the size of the cavity, so that long-range energy transfers can be discounted or (ii), that δ-ray equilibrium exists, then from equation 1.5 and equation 1.8, we can write:

$$f(Q) = \frac{\int_0^\infty \left(\frac{S^{\text{col}}(E)}{\rho}\right)_{\text{wat}} dE}{\int_0^\infty \left(\frac{S^{\text{col}}(E)}{\rho}\right)_{\text{cav}} dE} \tag{1.10}$$

$$= \left(\frac{\overline{S^{\text{col}}}}{\rho}\right)_{\text{cav}}^{\text{wat}} \tag{1.11}$$

where $\left(\frac{\overline{S^{\text{col}}}}{\rho}\right)^{\text{wat}}_{\text{cav}}$ is the ratio of the mass collisional stopping powers of the medium and the cavity, which, in each case have been averaged over the charged particle energy fluence.

In Bragg-Gray cavity theory, it is assumed that each electron which traverses the cavity loses energy in infinitesimal steps at a rate S^{col}. Thus Bragg-Gray cavity theory considers CSDA losses only: all energy lost by the primary electron is regarded as being dissipated locally. The theory does not take into account the fact that many collisions generate a fast secondary electron (with an appreciable range).

In order to extend Bragg-Gray theory, Spencer and Attix proposed a compartmentalisation of the electron spectrum into "fast" and "slow" elements [17]. Under their framework, electrons with energy $\geq \Delta$ are classified as fast. Then [17]:

1. the mass collisional stopping power is replaced by the **restricted mass collisional stopping power** $L^{\text{col}}_{\Delta}/\rho$ which includes only energy losses $< \Delta$. This means that collisions are considered to dissipate their energy locally only if they result in energy transfers less than an energy Δ.

2. the electron spectrum is changed to explicitly include secondary as well as primary electrons.

3. the integral extends only over the fast electron spectrum i.e. from Δ to ∞ rather than from 0 to ∞: a balance between incoming and outgoing slow electrons (with no net energy transfer) is assumed.

Such that the local dose can be formulated as:

$$D = \int_{\Delta}^{\infty} \Phi_{\text{E}}^{e\text{tot}} \frac{L^{\text{col}}_{\Delta}(E)}{\rho} dE \tag{1.12}$$

In the Spencer-Attix case, slow electrons (with energy $<\Delta$) that are *generated* within the cavity are not considered to form part of the fluence, their dissipative energy losses are assumed to be local under the restricted stopping power. However, initial electrons that formed part of $\Phi_{\text{E}}^{e\text{tot}}$ (both primary and secondary) may slow down sufficiently within the cavity that their energy tips just below Δ. At this stage their impact and energy dissipation is not considered under the Spencer-Attix formulation.

In order to consider their contribution to dose, Nahum added a track-end term [18]:

$$\text{Track-end term} = \left[\Phi_{\text{E}}^{e\text{tot}}(\Delta) \cdot \frac{S^{\text{col}}_{\Delta}(\Delta)}{\rho} \cdot \Delta\right] \tag{1.13}$$

which takes the form of integral 1.12 evaluated at a single energy Δ. For electrons of energy Δ, $S^{\text{col}}/\rho = L^{\text{col}}_{\Delta}/\rho$.

Thus under the Spencer-Attix-Nahum theory, the total dose deposited locally is [4]:

$$D = \int_{\Delta}^{\infty} \Phi_{\text{E}}^{e^{\text{tot}}} \frac{L^{\text{col}}_{\Delta}(E)}{\rho} dE + \left[\Phi_{\text{E}}^{e^{\text{tot}}}(\Delta) \cdot \frac{S^{\text{col}}_{\Delta}(\Delta)}{\rho} \cdot \Delta \right] \tag{1.14}$$

which leads to the Spencer-Attix-Nahum stopping power ratio:

$$f(Q) = \frac{\displaystyle\int_{\Delta}^{\infty} \Phi_{\text{E}}^{e^{\text{tot}}} \left(\frac{L^{\text{col}}_{\Delta}(E)}{\rho} \right)_{\text{wat}} dE + \left[\Phi_{\text{E}}^{e^{\text{tot}}} \cdot \left(\frac{S^{\text{col}}_{\Delta}(\Delta)}{\rho} \right)_{\text{wat}} \cdot \Delta \right]}{\displaystyle\int_{\Delta}^{\infty} \Phi_{\text{E}}^{e^{\text{tot}}} \left(\frac{L^{\text{col}}_{\Delta}(E)}{\rho} \right)_{\text{cav}} dE + \left[\Phi_{\text{E}}^{e^{\text{tot}}} \cdot \left(\frac{S^{\text{col}}_{\Delta}(\Delta)}{\rho} \right)_{\text{cav}} \cdot \Delta \right]} = s^{SA}_{\text{wat,cav}} \tag{1.15}$$

1.2.1.3 Alternative cavity theories

The Bragg-Gray and Spencer-Attix-Nahum theories described above both assume a cavity size that is small relative to the secondary electron range. In cases where the cavity size is large compared to this range, charged particle equilibrium will exist throughout almost all of the cavity volume, such that the local dose can broadly be equated to the collision kerma. From Figure 1.2, this gives:

$$f(Q) = \frac{\displaystyle\int_{0}^{\infty} \Phi_{\text{E}}^{\gamma} E \left(\frac{\mu_{\text{en}}(E)}{\rho} \right)_{\text{wat}} dE}{\displaystyle\int_{0}^{\infty} \Phi_{\text{E}}^{\gamma} E \left(\frac{\mu_{\text{en}}(E)}{\rho} \right)_{\text{cav}} dE} \tag{1.16}$$

which is often written in shorthand as:

$$f(Q) = \left(\frac{\overline{\mu}_{\text{en}}}{\rho} \right)_{\text{wat,cav}} \tag{1.17}$$

However, if is not always possible to classify a cavity as large or small relative to the range of secondary electrons. Instead of equation 1.16 or equation 1.15, a weighted sum of the two (theories for large and small cavities respectively) can be considered:

$$f(Q) = d \cdot s^{SA}_{\text{wat,cav}} + (1 - d) \left(\frac{\overline{\mu}_{\text{en}}}{\rho} \right)_{\text{wat,cav}} \tag{1.18}$$

Equation, 1.18 describes Burlin cavity theory [4]. It is applicable to solid-state detectors where the relatively high density of the sensitive media reduces the electron electron range.

1.2.1.4 Dose to water

Returning to our analysis of air-filled ionisation chambers, the Bragg-Gray and Spencer-Attix theories are only valid for ideal small cavities. In practice, several other corrections are needed for real small cavities as found in clinical detectors. For example, an air-filled cavity usually will cause less attenuation than the surrounding medium, effectively shifting the point of measurement upstream from the centre of the chamber. Additionally, all cavities average charged particle fluence (and hence dose) over their volumes. These effects are accounted for using a gradient correction factor p_{gr}. The steeper the dose gradient, or the larger the chamber radius, the larger the correction. Furthermore, the insertion of the cavity media will change the charged particle fluence, leading to the correction factor p_{fl}. The charged particle fluence will also be affected by the atomic composition of both the cavity wall and the central electrode, which must be accounted for using the correction factors p_{wall} and p_{cel} respectively. Considering these correction factors and equations 1.7, 1.9 and 1.15, the dose at a point in water can be written as [4]:

$$D_{\mathrm{wat}}(Q) = \left[\frac{Q_{\mathrm{ion}}}{\rho V} \cdot \frac{W_{\mathrm{air}}}{e}\right]_{\mathrm{Q}} \left[s^{SA}_{\mathrm{wat,cav}}\right]_{\mathrm{Q}} \left(p_{\mathrm{wall}}\, p_{\mathrm{cel}}\, p_{\mathrm{gr}}\, p_{\mathrm{fl}}\right)_{\mathrm{Q}} \tag{1.19}$$

or

$$D_{\mathrm{wat}}(Q) = \left[\frac{Q_{\mathrm{ion}}}{\rho V} \cdot \frac{W_{\mathrm{air}}}{e}\right]_{\mathrm{Q}} \left[s^{SA}_{\mathrm{wat,cav}}\right]_{\mathrm{Q}} p_{\mathrm{det,Q}} \tag{1.20}$$

where p_{det} accounts for **all** departures of the cavity from ideal Spencer-Attix conditions.

However, in practice it is much easier to calibrate a detector experimentally than to employ equation 1.20 (the volume of the cavity may not be known with sufficient accuracy and p_{det} is difficult to determine theoretically). Clinical detector calibration is performed against an absolute dosimeter at a PSDL (in the case of the UK, a graphite calorimeter is used at the NPL). Under the IAEA formalism, the reference dose D_{wat} to a point of water in a beam of quality Q is then determined as [12]:

$$D_{\mathrm{wat}}(Q) = M(Q)\, N_{D_{\mathrm{w}},Q_0} k_{Q,Q_0} \tag{1.21}$$

where $M(Q)$ is the reading of the dosimeter corrected for quantities such as: air pressure, humidity, ion chamber polarity and collection efficiency. N_{D_{w},Q_0} is the detector calibration factor (in terms of absorbed dose to water) provided by the PSDL. k_{Q,Q_0} is the energy spectrum correction factor which accounts for differences between the beam quality at the PSDL (denoted Q_0) and the user beam quality for a reference field of size $10\times10\,\mathrm{cm}^2$[5].

The quality correction factor k_{Q,Q_0} is defined as the ratio of calibration coefficients in beam qualities Q and Q_0. From equation 1.20 this is:

$$k_{Q,Q_0} = \frac{\left[\frac{W_{\mathrm{air}}}{e}\right]_Q \left[s^{SA}_{\mathrm{wat,cav}}\right]_Q p_{\mathrm{det,Q}}}{\left[\frac{W_{\mathrm{air}}}{e}\right]_{\mathrm{Q_0}} \left[s^{SA}_{\mathrm{wat,cav}}\right]_{\mathrm{Q_0}} p_{\mathrm{det,Q_0}}} \tag{1.22}$$

Which, assuming that the mean energy expended in air per ion pair does not change with beam quality, can be written as:

$$k_{Q,Q_0} = \frac{\left[s^{SA}_{\mathrm{wat,cav}}\right]_Q p_{\mathrm{det},Q}}{\left[s^{SA}_{\mathrm{wat,cav}}\right]_{Q_0} p_{\mathrm{det},Q_0}} \tag{1.23}$$

Considering the validity of k_{Q,Q_0} with changing field size

Collisional stopping power is a function of charged particle energy spectrum (note the dependence of the theoretical stopping power, equation 1.6, on the kinetic energy of the charged particle). As field size decreases, the average energy of the charged particle energy spectrum increases (fewer low energy electrons are scattered into the beam). However, computational studies have demonstrated that this effect is limited [13, 14, 16, 20, 21] and Spencer-Attix restricted mass collision stopping powers published for broad ($10\times10\,\mathrm{cm}^2$) fields remain relatively accurate for the dosimetry of small and composite fields[6]. However, the perturbation factors p_{det} strongly vary for different detectors used within small radiation fields [1]: it is mainly the variation of these factors that invalidates the use of k_{Q,Q_0} (and hence the key reference dosimetry equation, equation 1.21) under small field conditions.

[5] In the UK, $N_{D_{\mathrm{w}},Q}$ and k_{Q,Q_0} are combined into a single factor [19].

[6] A study by Sanchez-Doblabo *et al.* found a difference of just 0.3% between the on-axis Spencer-Attix stopping power ratio for a $10\times10\,\mathrm{cm}^2$ 6 MV beam and that for a 0.3 cm diameter 6 MV beam [22].

1.2.2 The IAEA/AAPM formalism for reference dosimetry in small static MV photon fields

In 2008, the IAEA/AAPM small fields dosimetry working group [23, 24] proposed a formalism (Alfonso *et al* [25]) for reference dosimetry in small fields, composite fields and non-standard beam-delivery systems. Under their framework, f_{ref} denotes a conventional reference field (of quality Q) for which the calibration coefficient of an ionisation chamber has been provided by a standards laboratory. f_{msr} denotes a machine-specific-reference field (of quality Q_{msr}) that is used instead of f_{ref} for those units that cannot establish conventional (broad-field) reference conditions. f_{clin} denotes a small clinical field (of quality Q_{clin}).

Step 1: Reference dosimetry

Initially, a simple extension of equation 1.21 enables reference dosimetry to be implemented for machines unable to deliver a conventional $10\times10\,\text{cm}^2$ beam [25]:

$$D_{\text{w},Q_{\text{msr}}}^{f_{\text{msr}}} = M_{Q_{\text{msr}}}\, N_{\text{D,w},Q_0}\, k_{Q,Q_0}\, k_{Q_{\text{msr}},Q}^{f_{\text{msr}},f_{\text{ref}}} \tag{1.24}$$

here the factor $k_{\text{Q}_{\text{msr}},\text{Q}}^{f_{\text{msr}},f_{\text{ref}}}$ accounts for the detector's difference in dose-response due to variations in geometry and beam quality conditions between an intermediate msr calibration field and the conventional reference field [25].

Step 2: Relative dosimetry

Next, a clinical field f_{clin} is considered. Here the absorbed dose to a point of water can be obtained as [25]:

$$D_{\text{w,Q}_{\text{clin}}}^{f_{\text{clin}}} = D_{\text{w,Q}_{\text{msr}}}^{f_{\text{msr}}} \times \frac{M_{\text{Q}_{\text{clin}}}^{f_{\text{clin}}}}{M_{\text{Q}_{\text{msr}}}^{f_{\text{msr}}}} \times k_{\text{Q}_{\text{clin}},\text{Q}_{\text{msr}}}^{f_{\text{clin}},f_{\text{msr}}} \tag{1.25}$$

where $D_{\text{w,Q}_{\text{x}}}^{f_{\text{x}}}$ is the dose to a "point-like" structure of water in field x and $M_{\text{Q}_{\text{x}}}^{f_{\text{x}}}$ is the dosimeter measurement in field x (x $\in$ clin,msr). The small-field point-dose correction factor, $k_{\text{Q}_{\text{clin}},\text{Q}_{\text{msr}}}^{f_{\text{clin}},f_{\text{msr}}}$, is given by:

$$k_{\text{Q}_{\text{clin}},\text{Q}_{\text{msr}}}^{f_{\text{clin}},f_{\text{msr}}} = \left[\frac{D_{\text{w,Q}_{\text{clin}}}^{f_{\text{clin}}}/M_{\text{Q}_{\text{clin}}}^{f_{\text{clin}}}}{D_{\text{w,Q}_{\text{msr}}}^{f_{\text{msr}}}/M_{\text{Q}_{\text{msr}}}^{f_{\text{msr}}}}\right] \tag{1.26}$$

Absolute dosimetry may be implemented for any clinical field and detector configuration via the Alfonso *et al.* formalism, although determination of small field correction factors

($k_{Q_{clin},Q_{msr}}^{f_{clin},f_{msr}}$) is necessary. This can be achieved using either Monte Carlo simulations [15, 26–32] or experimental methods [30].

Variability of $k_{Q_{clin},Q_{msr}}^{f_{clin},f_{msr}}$

In recent times many groups have investigated the variation of $k_{Q_{clin},Q_{msr}}^{f_{clin},f_{msr}}$ with field size, dosimeter and linac-type [15, 29–32]. The variability of $k_{Q_{clin},Q_{msr}}^{f_{clin},f_{msr}}$ (and hence practicability of the Alfonso *et al.* method) is a topic that is investigated in detail in Chapter 4.

Chapter 2

Using the EGSnrc system to model a linear accelerator and a range of small field detectors

For real radiotherapy scenarios involving multi-media detectors or patients, the dosimetry problem becomes impossible to solve analytically. From Chapter 1, even in the simplest case, determination of dose requires knowledge of electron fluence. The evolution of particle fluence through a volume is described by the Linear Boltzmann Transport Equations (LBTEs) [33, 34]. These are a pair of matched differential equations describing the rate of change (per unit length in the direction $\hat{\Omega}$) in photon and electron fluence respectively.

Photon LBTE:

$$(\hat{\Omega} \cdot \vec{\nabla})\Phi^{\gamma} = -\sigma^{\gamma}\Phi^{\gamma} + q^{\gamma\gamma}\Phi^{\gamma} + q^{e\gamma}\Phi^{e} + q^{\gamma} \tag{2.1}$$

The first two terms on the RHS describe interactions of existing photons, which is why they are linearly proportional to the photon fluence (Φ^{γ}); the third term is proportional to the electron fluence (Φ^{e}) because it describes interactions produced by the existing electrons. Further details on each term are included below:

$-\sigma^{\gamma}\Phi^{\gamma}$	photons lost in collisions
$+q^{\gamma\gamma}\Phi^{\gamma}$	photons produced by photon scattering events
$+q^{e\gamma}\Phi^{e}$	photons produced by bremsstrahlung and annihilation
$+q^{\gamma}$	photons emitted by sources

Electron LBTE:

$$(\hat{\Omega} \cdot \vec{\nabla})\Phi^e = -\sigma^e\Phi^e + q^{\gamma e}\Phi^\gamma + q^{ee}\Phi^e + q^e\Phi^e + \frac{\partial}{\partial E}(S_{\mathrm{R}}\Phi^e) \tag{2.2}$$

where:

$-\sigma^e\Phi^e$	electrons lost in collisions
$+q^{\gamma e}\Phi^\gamma$	electrons produced by photon scattering events
$+q^{ee}\Phi^e$	electrons produced by electron scattering events
$+q^e\Phi^e$	secondary electron production
$+\frac{\partial}{\partial E}(S_{\mathrm{R}}\Phi^e)$	gradual loss of electrons due to interactions with the electric field of the medium. S_{R} is the restricted collisional and radiative stopping power in the medium

Equations 2.1 and 2.2 are coupled, the electron fluence (Φ^e) can create photons through bremsstrahlung (the third term on the right hand side of equation 2.1) and the photon fluence (Φ^γ) can create electrons (the second term on the RHS of equation 2.2).

The LBTEs cannot be solved analytically in any but the simplest of cases, and are instead solved numerically for dosimetry applications. There are two principal techniques which may be applied: Grid-Based Boltzmann Solvers (GBBS) and Monte Carlo methods.

Grid-based Boltzmann solvers work by discretising the target volume in space, angle and particle energy [35]. This system can then be solved exactly, and the result will approach the real solution asymptotically as the resolution of the discretisation increases. In practical terms there is a constant trade-off between speed of calculation and accuracy. The use of GBBS is not yet widespread in radiotherapy but a new clinical algorithm (Acuros® by Varian Inc) has been developed using this method [34]. It is able to significantly optimise the processing time by neglecting the production of photons by bremsstrahlung (remember from Chapter 1 that this accounts for only 0.3-0.4% of expended energy). This makes the photon fluence independent of the electron fluence, allowing equation 2.1 to be solved first and then equation 2.2 solved using the calculated photon fluence, rather than having to iteratively solve the two coupled equations. Acuros has performed well in a variety of validation studies [36–40] and in future, it seems likely that GBBS will play an increased role in radiotherapy dose calculation.

The path of an individual particle through the volume of interest is governed by a set of interactions sampled randomly from appropriate probability distributions - it is only when the combined effects of a very large number of particles are considered that

a precise and predictable dose distribution emerges. This is the process that Monte Carlo methods seek to emulate, calculating the trajectories of individual particles. The result will converge on the same answer as GBBSs if the number of particles simulated is large enough, but the error in a Monte Carlo simulation is stochastic in nature, whereas the errors in a coarse grid GBBS solution are systematic. Having been used in medical physics for over fifty years [41], Monte Carlo is currently considered the gold-standard transport simulation method for external beam radiotherapy, brachytherapy and radionuclide therapy. A variety of different codes exist to enhance and optimise the performance of Monte Carlo simulations for different particles and different energy ranges, the most widely used for medical applications being MCNP [42], GEANT [43], GATE [44], FLUKA [45], Penelope [46] and EGSnrc [47]. EGSnrc was chosen for this work as it has a sophisticated macro language that was developed especially for external beam photon radiotherapy applications.

2.1 Monte Carlo methods

In Monte Carlo modelling of particle transport, random numbers play an essential role in numerous aspects of every simulation. An individual photon will travel from interaction point to interaction point, with the travel distance randomly sampled from a distribution about its mean free path in the medium. At the interaction point an interaction type is selected randomly based on the differential cross sections for the various interaction mechanisms. The energies and directions of the resulting particles are also chosen at random from the appropriate distribution. Despite all this randomness, when enough particles are considered together a very precise overall dose distribution will emerge. For a set of N individual particles, the statistical uncertainty (standard deviation) of the calculated dose will be proportional to $1/\sqrt{N}$[1].

Based on the review article of Rogers [48], let us consider a simple case of a 6 MV photon beam entering a block of water. Figure 2.1 demonstrates that in water, for energies >1 MeV, basically only two interaction processes need to be considered: Compton scattering (with cross-section Σ_{compton}) and pair production (with cross-section Σ_{pair})[2]. For each photon entering the Monte Carlo simulation, values are required for two parameters: (i) the distance travelled to the first interaction site (ii) the type of interaction that takes place.

[1] Additionally, the calculated dose will be subject to systematic uncertainties in parameters related to (i) the interaction cross-sections employed by the Monte Carlo code, (ii) the geometries and material compositions of the real objects modelled by the user.

[2] In higher Z materials (such as Lead, as considered in Figure 2.1), the situation would be more complex as coherent scattering and the photoelectric effect would also be of relevance.

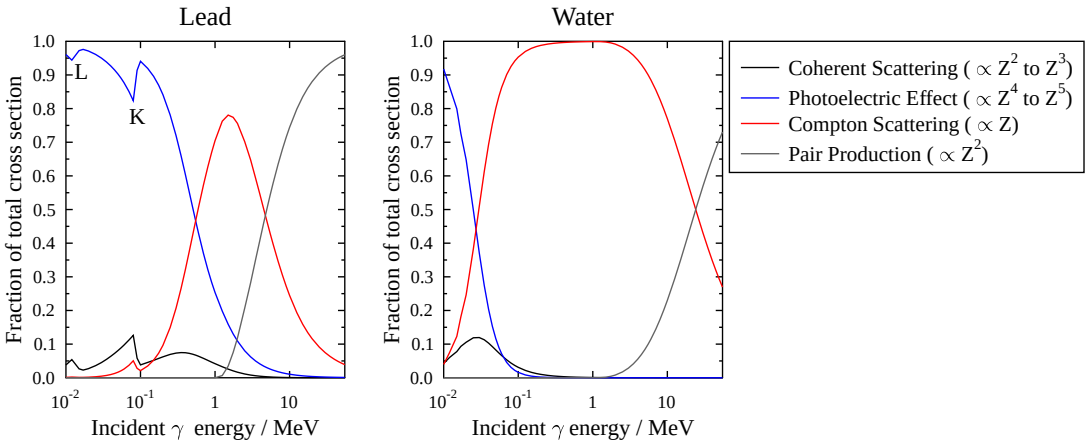

FIGURE 2.1: Plots to show relative occurence of interaction processes with photon energy for lead and water . All probabilities drawn from the ICRU512 cross-section file distributed with EGSnrc. The legend includes, in brackets, the approximate Z-dependence of each cross section.

First we select $R1$, a random number from a uniform distribution between 0 and 1. As photon pathlengths are exponentially distributed, the distance to the first interaction site can be modelled as $x = -ln(R1)/\Sigma_{\text{total}}$[3].

Second, we select random number $R2$ (again distributed uniformly between 0 and 1) and use it to determine which interaction occurs. If $R2 < \Sigma_{\text{compton}}/\Sigma_{\text{total}}$, then a Compton scattering event occurs, otherwise the interaction type is pair production.

The same basic principles are applied to all other aspects of the Monte Carlo simulation. For instance, in order to determine the scattering angle and energy of a secondary electron and associated photon from a Compton scattering event, random numbers are used to sample parameters from the appropriate probability distributions. If the interaction had been pair production, the same process would be applied to select the energies and directions of the resulting electron and positron. Following each interaction the resultant particles are followed as they continue to interact and lose energy until their energy falls bellow predetermined cut-off values. This process is then repeated for a very large number of initial particles.

Of course, the example is not yet complete as no information has yet been stored. The Monte Carlo simulation must keep track of, or "score" quantities of interest. Often the most relevant quantity is dose, which is scored by accumulating the absorbed energy per region.

[3]Here the set of distances sampled is exponentially distributed between 0 and ∞ with a mean of $1/\Sigma_{\text{total}}$.

2.2 The EGSnrc system

The EGS (Electron Gamma Shower) code was developed during the 1970s at the Stanford Linear Accelerator [47]. In the 1980s-1990s, the Omega group within the National Research Council of Canada (NRC) refined the code to improve its applicability to medical physics, particularly focussing on the energy range 10 keV to 50 MeV [47].

Within the EGS system, subroutines handle all of the physics of the simulation so that the user may focus on the geometrical and scoring aspects. A series of radiotherapy-specific "user codes" are included as part of the EGSnrc distribution, including BEAMnrc [49] (for modelling linacs), DOSRZnrc (for calculating dose in arbitrary geometries consisting of cylinders) [50], DOSXYZnrc [51] (for calculating dose to geometries consisting of rectilinear voxels), egs_chamber [52] (a flexible system allowing for the definition of complex geometries and particle sources) and flurznrc (for scoring particle fluence in cylindrical geometries) [50].

The EGSnrc system models a range of interaction processes: annihilation of positrons; inelastic Moller scattering of electrons and Bhabha scattering of positrons (both from atomic electrons); bremsstrahlung by both positrons and electrons; elastic multiple and single scattering of electrons and positrons from nuclei and atomic electrons; pair production; Compton scattering; Photoelectric interactions; Rayleigh scattering; and atomic relaxation by production of fluorescent x-rays and Auger electrons [47].

2.2.1 Variance reduction and efficiency enhancement techniques

Within Monte Carlo codes, variance reduction techniques are optional modifications to the main particle transport algorithms which reduce the computing time required (per history) without introducing any bias into the simulation results.

As radiotherapy simulations can prove extremely time consuming, it is often necessary to utilise additional *approximate* "efficiency enhancement techniques"[4].

By default, EGSnrc employes three approximate techniques: condensed histories, range-rejection and energy cut-offs. In this work two real variance reduction techniques - directional bremsstrahlung splitting and photon cross-section enhancement - were also utilised.

[4]Where, if the user opts to use input parameters which fall outside of the recommended set, simulation bias may be introduced.

2.2.1.1 Condensed histories

As neutral particles photons are relatively uninteracting: photons of therapeutic energies have mean free paths of the order of 10 cm in human tissue and water [53]. Electrons on the otherhand are highly interacting: they slow down and undergo hundreds of thousands of scattering events involving slight deflections but virtually no energy loss. Thus complete simulations of charged particle histories typically require much more processor time than complete simulations of photon histories. To enable simulations to be completed in a practical timeframe, complete electron histories may be "condensed" into a series of larger steps, each considering the effect of many events at once. During a condensed history step, an electron continuously loses energy due to low energy "soft" interactions which are simulated implicitly using linear restricted stopping powers. "Hard" interactions (involving energy transfers above a certain threshold) are all simulated explicitly as in the photon case. This method forms the basis of all MC codes used for radiotherapy [53]. It was originally developed by Berger in 1963 [54] and was implemented in the EGSnrc code system by Karakow in 2000 [55].

2.2.1.2 Range rejection

Upon simulating an interaction, EGSnrc uses restricted stopping power tables to calculate the residual range of each charged particle involved (according to the media and particle energies). Range rejection can be used to terminate the histories of charged particles with insufficient range to leave the current region, and the remaining energy of the particle is deposited immediately [56]. As the dose is calculated on a region by region basis, this generally makes no difference to the overall dose distribution. However this assumption neglects the possibility that some terminated electrons might have generated bremsstrahlung photons which would then carry some energy outside of the region.

2.2.1.3 Energy cut-offs

Monte Carlo simulations may, in principle, track each particle from birth to death. In practice, for low energy particles, it is more efficient to deposit dose at the point when the particle energy drops below a pre-assigned cut-off. The EGSnrc code system enables users to define one cut-off for electrons/positrons (ECUT[5]) and another for photons (PCUT).

[5] Which includes the rest mass of the electron.

2.2.1.4 Directional bremsstrahlung splitting

Directional bremsstrahlung splitting (as employed in BEAMnrc) is used to increase the number of particles in "important" regions and decrease the number of particles in "unimportant" regions [57]. At every bremsstrahlung interaction site, N photons are generated, and each allocated a weighting of $1/N$. Those photons aimed into the field of interest (defined by the user) are always followed, whereas those aimed outside the field of interest undergo Russian Roulette, where the weighting of each surviving photon is increased by the splitting factor.

2.2.1.5 Photon cross sectional enhancement

For simulations of small detector cavities inside large water phantoms, it can be useful to artificially increase the total photon cross sections in the region around the detector, making the photon mean free path shorter and increasing the number of interactions. An incident photon will be split into an interacting portion (fraction $[1/b]$) and a non-interacting portion (fraction $[1 - 1/b]$) [56]. All particles emergent from an interaction are weighted w_0/b, where w_0 is the weight of the original photon. However, whilst all electrons are further transported (there are b times as many electrons compared to without cross sectional enhancement), photons are terminated with probability $1/b$: if they survive they have the original weight w_0 [56].

2.2.2 Parallelisation

Monte Carlo simulations are inherently a highly parallelisable form of computation because the history of each particle is independent of all the others: there is no dependency or communication required between computation threads once each thread has received the initial geometry and beam data. All of the EGSnrc user codes have been designed to run in parallel on an arbitrary number of CPUs. This research utilised the Oxford Supercomputing Centre and the IRIDIS HPC facility (provided by the e-Infrastructure South Centre for Innovation) where single simulations could be distributed over hundreds of CPUs.

2.3 Modelling a linac using BEAMnrc

2.3.1 Geometrical considerations

In clinical linacs, electrons are emitted by an electron gun, accelerated by a static electric field and injected into an accelerating waveguide. After leaving the waveguide, the electron beam is deflected by a series of electromagnets and strikes a two-layer tungsten and copper target. Within the target, bremsstrahlung photons are produced.

The linac components downstream from the bremsstrahlung target together form the "treatment head": the system designed to deliver a clinically useful beam.

This work modelled a Varian 2100 iX (available for use at the Oxford Cancer Centre, shown schematically in Figure 2.2). Within the treatment head:

1. the primary collimator limits the angle of the initial beam of bremsstrahlung photons
2. the flattening filter is used to homogenise the photon fluence across the beam
3. the ion chamber is a dual, sealed parallel-plate chamber which is used to monitor the beam output - in terms of Monitor Units (MU)
4. a light-field mirror is used, together with a lamp positioned to one side, to reflect light through 45° enabling a surrogate radiation field to be visualised on the patient/phantom
5. the secondary collimators determine the size of rectangular/square fields
6. the multi-leaf collimators (MLCs) consist of many tungsten leaves which move independently to shape the beam.

Linear accelerator modelling for Monte Carlo simulations is a topic reviewed extensively by Verhaegen and Seuntjens [58] and Reynaert *et al* [59]. In this study, each component labelled in Figure 2.2 was modelled using a separate module within BEAMnrc. Values for geometrical and chemical-composition input parameters were drawn from confidential specifications provided by Varian Medical Systems.

2.3.2 Monte Carlo considerations

Variance reduction was performed within the flattening filter via Directional Bremsstrahlung Splitting (DBS) using a splitting factor of 1000 and, for all fields of side length 10 cm

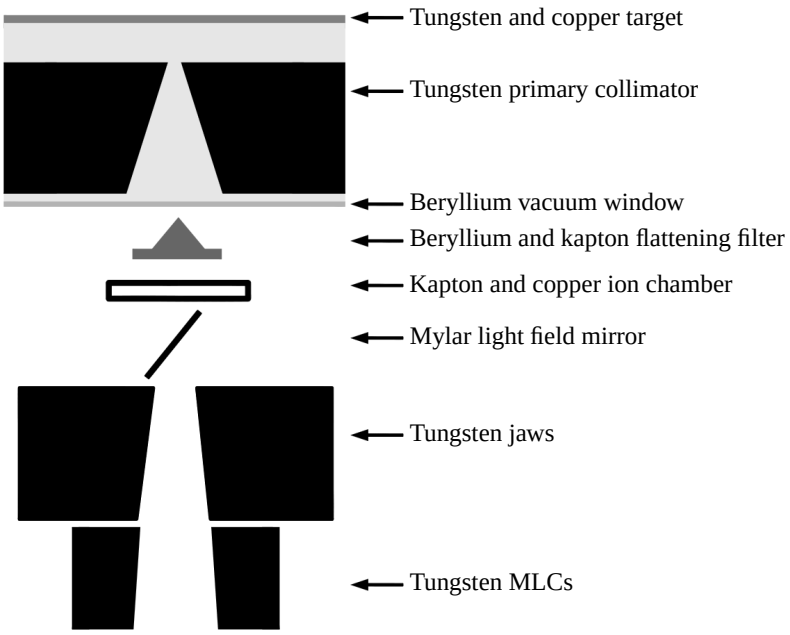

FIGURE 2.2: Diagram to show the various component modules included in the BEAMnrc linac model .

or less, a DBS radius of 10 cm; for larger fields, the DBS radius was set to the field side length. In all cases, DBS electron splitting was also applied and electron range rejection was implemented. BEAMnrc simulations were performed using total electron and photon cut-off energies (ECUT and PCUT) of 0.7 MeV (corresponding to a kinetic energy of 0.189 MeV) and 0.01 MeV respectively. As for many of the EGSnrc codes, within BEAMnrc it is possible to store a (very large) 'phase space' file at any plane. Phase space files contain the energy, direction, position and type for all particles crossing the plane. In this work, phase spaces were scored at a distance of 100 cm from the source and were subsequently used as input for the DOSXYZnrc [51] and egs_chamber codes [52]. As per the standard output for the EGS codes, all simulated doses were recorded as the dose per incident electron on the linac bremsstrahlung target.

2.4 Modelling small-field detectors

A range of different radiation detectors exist to measure relative dose distributions for therapeutic photon beams. Table 2.1 lists the main types of radiation detectors, and the quantities they measure.

	Type	**Measured quantity.** Details.
1	Calorimeters	**Temperature.** Used for absolute radiation dosimetry at national standards laboratories.
2	Ionisation chambers	**Charge.** The most stable and widely used class of dosimeter in radiotherapy.
3	Silicon diode detectors	**Charge.** Highly sensitive, based upon a p-n junction.
4	Diamond detectors	**Charge.** Almost energy independent with low dark current.
5	MOSFETS	**Threshold voltage.** The sensitive region can be made very small (with sub-mm dimensions) for use in *in-vivo* dosimetry.
6	Scintillation detectors	**Light intensity.** Can achieve an excellent degree of water equivalence.
7	Thermo Luminescence detectors (TLDs)	**Light intensity.** Compact dosimeters often used for monitoring staff exposure.
8	Gel dosimeters	**Chemical change.** 3D dosimeters, analysed using an imaging technique (*e.g.* MRI).
9	Film	**Chemical change.** May be radiographic (requiring development) or radiochromic (with no need for chemical processsing).

TABLE 2.1: Main types of dosimeter used in radiotherapy

This thesis only considers dosimeter types 2-4 (Table 2.1), since they are (a) the most commonly used in acquiring small-field data and (b) were available for study at the Oxford Cancer Centre[6]. The specific detector models were: the unshielded Electron Diode (Ediode) 60012, the PinPoint chamber 31006, the Diamond detector 60003 and the MicroLion chamber 31018, all manufactured by PTW (PTW Freiburg, Germany). The sensitive region properties of these detectors are shown in Table 2.2.

2.4.1 Basic principles of operation

Gas-filled ionisation chambers (PinPoint 31006)

The PTW PinPoint 31006 is an air-filled ionisation chamber. Radiation entering the air-filled cavity causes ionisation, the resulting ion pairs are collected by charged electrodes. The voltage across the chamber is such that almost all ion pairs produced by the impinging radiation are collected.

Liquid-filled ionisation chambers (MicroLion 31018)

Within gas-filled cavities the number of electron-ion pairs generated is relatively small, in part due to the number of target atoms per unit volume. In order to obtain high resolution measurements in low radiation environments, liquid filled ionisation chambers

[6]Additionally radiochromic film could have been studied [60], but for small field dosimetry noise can prove problematic and scanning techniques also require considerable optimisation.

	Medium & density (g/cm^3)	**Shape**	**Side-length /diameter (mm)**	**Thickness (mm)**
Ediode 60012	Silicon $\rho = 2.33$	Very thin cylinder which rests towards the top of a larger cuboid of silicon	1.000	0.0025
MicroLion 31018	Isooctane $\rho = 0.69$	Thin cylinder	2.500	0.3500
Diamond 60003	Diamond $\rho = 3.52$	Thin, square-faced cuboid	2.770	0.2600
PinPoint 31006	Air $\rho = 0.0013$	Long cylinder topped with a hemisphere	2.000	5.000

TABLE 2.2: Sensitive region properties for the PTW radiation detectors considered in this study. In the case of the Diamond 60003, the sensitive region dimensions quoted are specific to the instrument at the Oxford Cancer Centre (these parameters were drawn from an individual detector certificate supplied by PTW). More generally for this model, PTW quote a sensitive volume range of 1 to 6 mm^2, with a typical thickness of 0.3 mm (http://www.ptw.de/2268.html).

can be used to increase the probability of charge pair production. In the case of the PTW MicroLion 31018, the liquid used is isooctane.

Solid-state detectors: diamond detector and silicon diode (Diamond 60003 and Ediode 60012) In solid media, covalent bonding between atoms creates a series of discrete energy levels which can be categorised into 'valence' and 'conduction' bands (the conduction band containing the higher energy levels). These two bands are separated by a forbidden gap. Whilst insulators such as diamond have a very large energy gap between bands, for conductors the band gap is non-existent.

Diamond's band gap is $\approx 5.5\,eV$ (large compared to Silicon's band gap of $1.12\,eV$). Crossing the diamond, a charged particle or photon with energy above the band gap produces electron/hole pairs which are separated by an electric field applied between two electrodes.

Silicon diodes consist of two Si structures in contact with each other: a p-doped one (containing a small amount of an electron acceptor, e.g. Boron) and an n-doped one (containing electron donor atoms, e.g. Phosphorous). At the junction between the two structures, electrons migrate from the n-doped region to the p-doped region, leaving behind fixed positive charges. Holes migrate to the n-doped region. This results in (i) a potential gradient and (ii) a "depleted" junction where a negligible number of charge carriers remain. Radiation with energy above the band gap produces electron-hole pairs in the depleted region. Due to the original potential gradient (no voltage is applied to

the PTW Ediode 60012), charge is collected as electrons are attracted to the n-side and holes are attracted to the p-side. The PTW diode is a 'p-type': holes are the majority carrier.

2.4.1.1 Summary of detector properties

Table 2.3 summarises the relative performance of small field detectors considered in this study.

2.4.2 Producing EGSnrc compatible detector models

2.4.2.1 Geometrical modelling

The geometry of the four detectors was modelled using the EGS++ macro-language according to confidential specifications provided by PTW.

3D renderings of the geometrical models are shown in Figure 2.3.

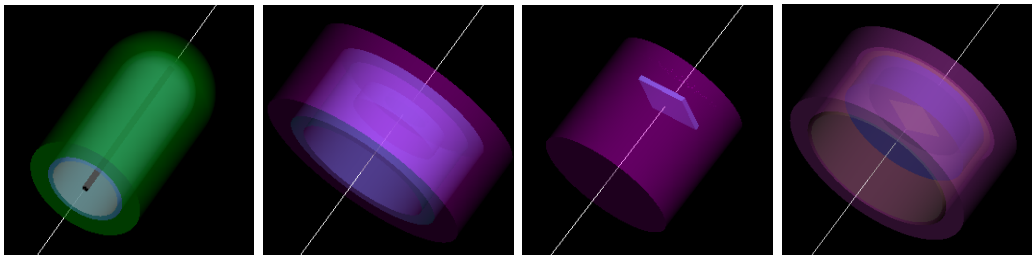

(a) PinPoint (b) MicroLion (c) Diamond (d) Ediode

FIGURE 2.3: Diagram to show EGS++ models of the four detectors considered in this study

2.4.2.2 Interaction modelling

Cross-section files

Certain detector materials included in the PTW detector specifications do not form part of the standard ICRU database (Isooctane for the MicroLion, and PEEK, Epoxy and FR4 for the Ediode). For these materials, cross-section files were generated using the EGSnrc pegs4 executable [61]. Using this executable it is possible to specify unique materials according to their relative atomic weights in order to collate appropriate attenuation data at various energies (compounds and mixtures are dealt with in the same manner). In generating these new cross section files a minimum total electron energy of 512 keV was considered along with a minimum photon energy of 1 keV. The NIST XCOM cross-section database (the EGSnrc default) was used.

Detector	Operation parameters used	Penumbra precision	Out of field precision	Dose stability	Dose rate independence	Energy response (MeV)
PinPoint, PTW 31006 	Reference point: 3.4 mm below front Voltage: +300 V Pre-irradiation: 2 Gy	++	++++ The response to low-energy scattered radiation is excellent (in contrast to silicon diodes)	++++	++++	++++
MicroLion, PTW 31018 	Reference point: 0.975 mm below front Voltage: +800 V Pre-irradiation: 5 Gy	+++	+++	++++	++++	++++
Ediode, PTW 60012 	Reference point: 0.6 mm below front Voltage: 0 V Pre-irradiation: none	++++ Due to the relatively high density of atoms in silicon, a small sensitive volume can be afforded	++	++ There is a degradation of response with dose - relatively frequent recalibrations are necessary	+++	+++
Diamond, PTW 60003 	Reference point: 1 mm below front Voltage: +100 V Pre-irradiation: 9 Gy	+++	+++	++++	++ Impurities can act as traps and create an electric field that is opposed to the applied voltage. This leads to a slightly non-linear dose-rate dependence.	+++ The carbon-to-water stopping power ratio is approximately constant over 1-20 MeV [62]. However, impurities can lead to deviations.

TABLE 2.3: Selection criteria for small field dosimeters, based upon PTW's application guide [63]. ++++ excellent +++ very good ++ good. In each case the "reference point" refers to the location of that detector's effective point of measurement.

PEEK and Isooctane are compounds with defined compositions: $C_{19}H_{12}O_3$ and C_8H_{18} respectively. Unfortunately, PTW were not able to supply chemical compositions for their specific forms of Epoxy and FR4. A number of different Epoxy compositions can be found online, including $C_6H_6O_5$ and $C_{21}H_{25}O_5Cl$. Cross section files were generated for both of these compositions. Figure 2.4(a) demonstrates that the restricted electron stopping powers were found to be very similar at all energies. Slight differences were observed in the photon geometric mean free paths, attributable to the effect of the Chlorine k-edge (Figure 2.4(b)). In the absence of evidence for the exact PTW Epoxy composition, the simpler form of Epoxy was selected for this work.

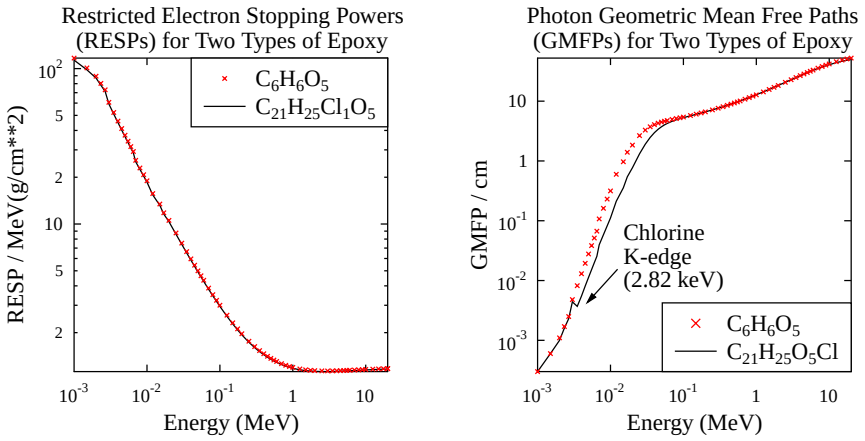

(a) (b)

FIGURE 2.4: Considering the effect of exact Epoxy composition on cross section data

FR4 is a form of glass-reinforced epoxy laminate. In the absence of further information it was here modelled as a single medium with the composition shown in Table 2.4.

Element	% mass
C	15.80
H	1.33
O	38.56
Si	21.77
B	1.32
Al	1.64
Na	3.56
K	6.52
Zn	7.00
Ti	2.32
Sb	0.18

TABLE 2.4: Assumed Chemical Composition of FR4 (taken from SCT end-cap module of the ATLAS project http://hepwww.rl.ac.uk/Atlas-SCT/engineering/material_budget/models/Endcap_Module/ATLAS_ECSCT_Materials.pdf)

Density-effect corrections (due to polarisation of the medium, see theoretical stopping power equation 1.6) were calculated using the NIST e-star database[7] and applied in the cross-section calculation process.

Monte Carlo parameters

Within the egs_chamber Monte Carlo code, a global ECUT of 0.512 MeV (corresponding to an electron kinetic-energy of 1 keV) was used for all point-dose simulations. In order to restrict the duration of some more computationally intensive (dose length product / dose area product) simulations, the ECUT was raised to 0.521 MeV in all detector regions except the air-filled cavity of the PinPoint detector, where it was maintained at 0.512 MeV (the CSDA range of a 10 keV electron is $\approx 2.5\,\mu$m in liquid water, but rises to ≈2 mm in air [62]). Cross-section enhancement [52] was also applied, typically using an enhancement factor of 128 within a shell that extended 1 cm beyond each chamber in all directions.

[7] http://physics.nist.gov/PhysRefData/Star/Text/ESTAR.html

Chapter 3

Optimising and validating the linac model

The results of accelerator treatment head simulations are known to depend strongly on the modelled characteristics of the incident electron beam, namely the electron energy, beam radius and beam angular divergence (AAPM TG report [64]). For a given linac, the values of these parameters are known only approximately such that iterative optimisation should be performed, comparing simulated against measured data.

3.1 Obtaining measured data

Throughout this chapter the measured data stems from 6 MV linac experiments performed using the PTW MP3 water tank system. The PTW MP3 is a large perspex tank (dimensions: 60 cm × 70 cm × 45 cm), with a drive system that allows a range of radiation detectors to be positioned with 0.1 mm precision throughout the tank's volume. Once the tank has been filled with water, stepping motors are used to adjust the distance between the linac head and water surface (with the source to surface distance, SSD, set according to the linac's optical distance indicator). In order to generate lateral profiles and Percentage Depth Dose plots (PDDs), the MP3 tank is used in conjunction with the TANDEM electrometer and the software package MEPHYSTOmc^2 (all manufactured by PTW Freiburg).

3.1.1 Data from linac commissioning

During linac commissioning, the water tank system was used to obtain lateral profiles and PDDs for a range of field sizes between $40\times40\,cm^2$ and $3\times3\,cm^2$[1]. For all fields bar the smallest (the 3 cm field), a Semiflex ion chamber was used (model 30-316 manufactured by PTW Freiburg, with a cavity diameter of 5.5 mm). For the 3 cm field, the PTW PinPoint ion chamber was used (cavity diameter = 2 mm). In all cases, the standard SSD was 100 cm. The data acquired during linac commissioning went on to form the basis of the beam model in the clinical treatment planning system (Varian Eclipse^{TM}) and is thus referred to throughout this chapter as 'Eclipse' data. At the Oxford Cancer Centre a single cross-checked beam model is used for all six Varian 2100 iX machines.

3.1.2 Data obtained during this project

We performed a range of additional small field measurements for this project using a single Cliniac iX at the Oxford Cancer Centre. The detectors used were the PinPoint PTW 31006, MicroLion PTW 31018, Ediode PTW 60012 and Diamond PTW 60003 (for further details on these detectors, please see Chapter 2, *e.g.* page 31).

For this aspect of the work two small field sizes were utilised: the smallest deliverable by the linac jaws (a square field with nominal side-length 0.5 cm) and a slightly larger square field (with nominal side-length 1 cm). A fixed collimator rotation of 0° was used. Field sizes were defined by the linac jaws alone, with the MLCs fully retracted. No reference detector was utilised, being impractical for some of the small fields considered, and instead relatively long detector dwell times (typically of 1 s) were employed for all measurements. Jaw positions were held fixed throughout all measurements made for each field less than 3 cm, and the FWHM values of measured profiles were used to set the jaw positions in the BEAMnrc linac model.

Irradiations were typically performed with the detector axis orientated parallel to the central axis of the radiation beam, with its reference point[2] located at a depth in water of 5 cm, set up at an SSD of 100 cm. The PTW center-check software was used to position the detectors at the centre of the radiation field in the horizontal plane, to a precision of +/-0.1 mm. Manufacturer-recommended biases[3] were applied in all cases. When considering ratios of measurements across two field sizes, a negligible polarity effect was observed for the PinPoint detector utilised here (in line with the findings of Chung *et*

[1] Diagonal profiles were also obtained for a $40\times40\,cm^2$ field.

[2] Effective point of measurement. Manufacturer recommended values were used as included in the table on on page 31.

[3] See the table on on page 31 for these values.

al.[65]), and so all relevant measurements described in this study were performed with a positive polarity setting[4].

"Measurement Output Factor" ($\mathrm{MOF}_{\mathrm{det}}^{f_{\mathrm{clin}}}$), an experimentally-obtained quantity, was defined as:

$$\mathrm{MOF}_{\mathrm{det}}^{f_{\mathrm{clin}}} = \frac{M_{\mathrm{Q_{clin}}}^{f_{\mathrm{clin}}}(\text{depth} = 5\,\text{cm, SSD} = 100\,\text{cm, MU} = 100)}{M_{\mathrm{Q_{msr}}}^{f_{\mathrm{msr}}}(\text{depth} = 5\,\text{cm, SSD} = 100\,\text{cm, MU} = 100)} \tag{3.1}$$

i.e. the ratio of the readings M from a given detector in (i) a clinical small field f_{clin} of beam quality Q_{clin} and (ii) a machine specific reference field, f_{msr} of beam quality Q_{msr}, where in both cases, the detector is located centrally within the horizontal beam, at a depth of 5 cm in a water phantom set up at an SSD of 100 cm and irradiated with 100 Monitor Units (MU).

MOF measurements were averaged over a series of at least three repeated readings. $3\times3\,\mathrm{cm}^2$ was chosen as a convenient machine specific reference field (f_{msr}) as it is both sufficiently large (on the scale of the detectors considered here) to avoid the key problems associated with small field dosimetry, and sufficiently small to allow relatively fast Monte Carlo simulation.

3.2 Finding the optimum value for the electron beam mean energy

The following sections describe the optimisation of the BEAMnrc linac model.

As shown by Sheikh-Bagheri and Rogers, depth-dose curves are sensitive to the electron beam energy but show no sensitivity to the FWHM of the electron beam intensity distribution [66]. For this reason, PDD simulations for energies ranging from 5.5 MeV to 6.4 MeV were performed (in 0.1 MeV increments) to optimise the electron beam kinetic energy.

For all PDDs, the normalisation factors used to scale the Monte Carlo data to the Eclipse data corresponded to those which gave the minimum square deviation between the two over the full data range.

Considering the lower axes in Figure 3.1, it is clear that a kinetic energy of 6.0 MeV results in the best solution: here all local percent differences between the simulated

[4] Additionally, since we were only interested in relative dose data, no other correction factors (*e.g.* for pressure or temperature) were applied to detector readings.

and measured data points lie centrally within $\pm 1\%$ bounds. For simulated energies $< 6.0\,\text{MeV}$, as the depth is increased the MC simulations underestimate the dose relative to the Eclipse values, whereas for energies higher than 6.0 MeV, the reverse is true.

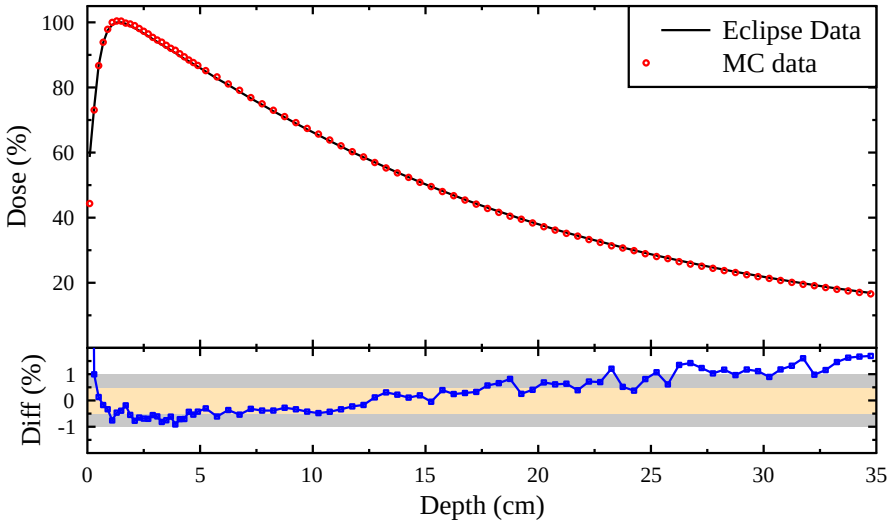

(a) 5.8 MeV MC model, 10 cm x 10 cm field

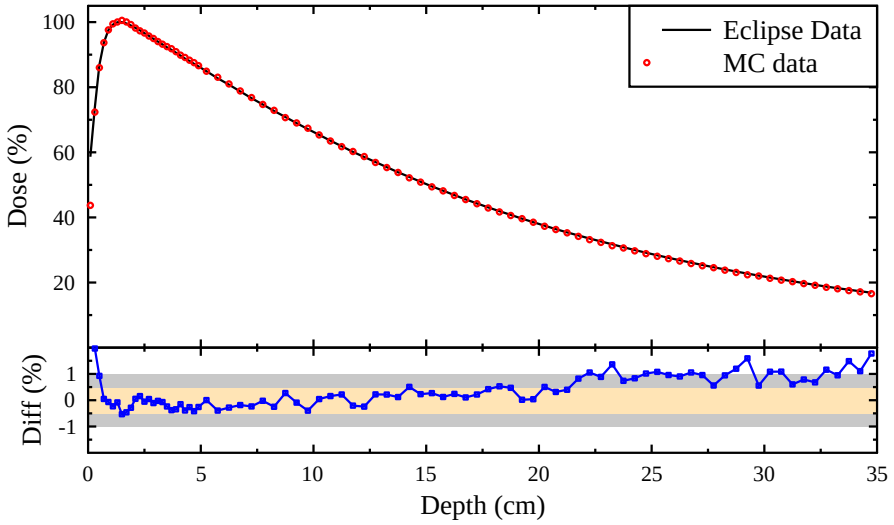

(b) 5.9 MeV MC model, 10 cm x 10 cm field

FIGURE 3.1: Part 1. Comparison of simulated (MC) to measured (Eclipse) PDD data for modelled electron beams of various energies. In each case the electron beam radius is 1mm. The lower axes show the difference between the measured and simulated data points as a percentage of the local measured value. The statistical uncertainties associated with the MC data points were all <0.2% of the maximum dose.

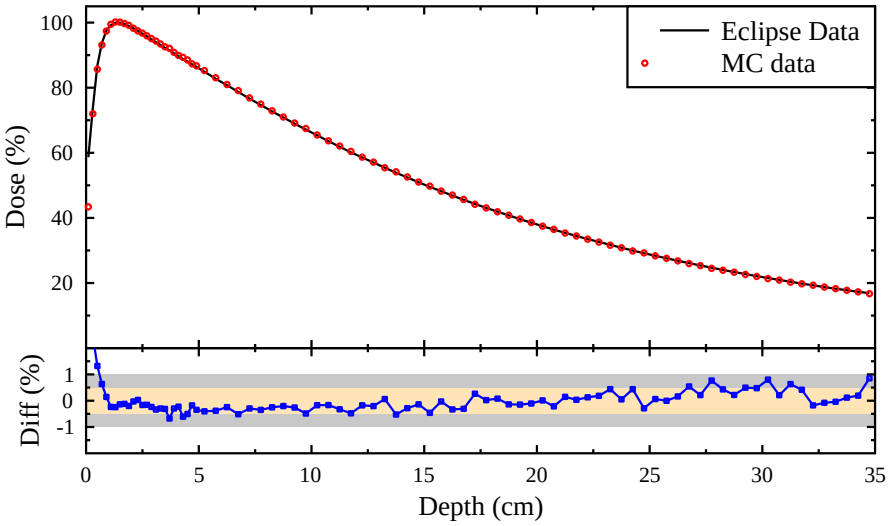

(c) 6.0 MeV MC model, 10 cm x 10 cm field

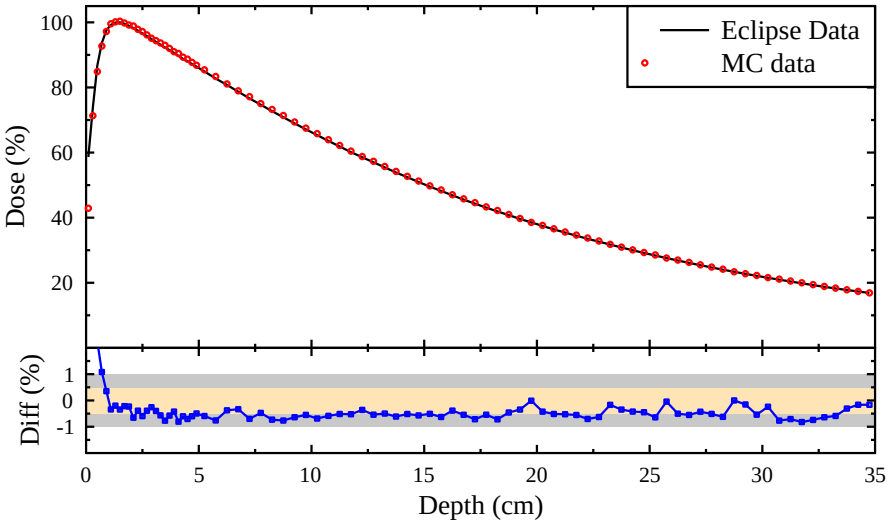

(d) 6.1 MeV MC model, 10 cm x 10 cm field

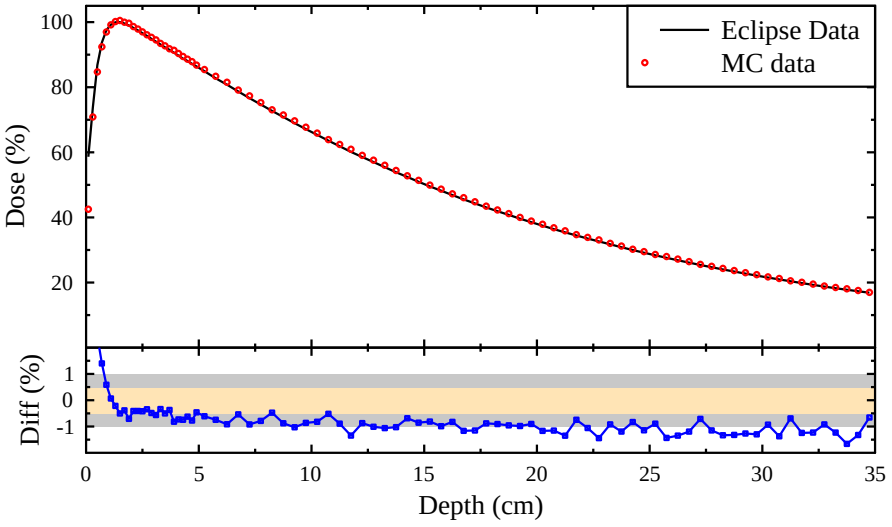

(e) 6.2 MeV MC model, 10 cm x 10 cm field

FIGURE 3.1: Part 2. Comparison of simulated (MC) to measured (Eclipse) PDD data for modelled electron beams of various energies. In each case the electron beam radius is 1mm. The lower axes show the difference between the measured and simulated data points as a percentage of the local measured value. The statistical uncertainties associated with the MC data points were all <0.2% of the maximum dose.

3.2.1 Metrics to compare simulated versus measured data across the range of input energies

In their 2006 study entitled "Determination of the initial beam parameters in Monte Carlo linac simulation" [67], Aljarrah *et al.* tested several cost functions for comparing measured against simulated data. A brief description of each cost function they considered is included below:

1. The χ^2 function: a commonly used cost function defined as: $\chi^2 = \frac{1}{n}\sum_{i=1}^{n}(D_i{}^{(m)} - D_i{}^{(s)})^2$, where $D_i{}^{(m)}$ are the measured data points and $D_i{}^{(s)}$ are the simulated data points.
2. The mean absolute error (MAE), defined as: $\text{MAE} = \frac{1}{n}\sum_{i=1}^{n}|(D_i{}^{(m)} - D_i{}^{(s)})|$
3. The slope of difference: the slope of a straight line that fits the dose difference between the calculated and measured points
4. The absolute dose difference at two pre-defined points near the beam edge (for lateral profiles)
5. A new cost function, κ_α: the fraction of the voxels with absolute dose difference less than $\alpha\%$ of the maximum measured dose

All of the cost functions tested by Aljarrah *et al.* [67] consider the discrepancy between simulated and measured data in one dimension only: the dose dimension. Whilst such metrics are adequate for the analysis of spatial regions with low dose gradients, it is also desirable to perform "distance to agreement" analyses in spatial regions with high dose gradients (e.g. PDD build-up regions and lateral profile penumbral regions). In 1998, Low *et al.* [68] published a composite quantitative comparison technique that considered both dose difference and distance to agreement: γ-analysis. γ-analysis has already been applied to Monte Carlo model commissioning by Pena *et al.* [69] amongst others. However, the quantity gamma degenerates to the dose-difference and distance-to-agreement tests in shallow and very steep dose gradient regions respectively [70]. This degeneration limits its utility.

Here a new approach is tested which aims to produce a two-dimensional cost-function applicable to all PDD / profile regions. The cost function is based upon the principle of calculating the distance of closest approach between each simulated data point and an interpolated line between the measured data points. The vector algebra calculation principle is as defined on the next page.

1. Define line segment vectors between each pair of measured data points (marked by circles) to interpolate the measured data set

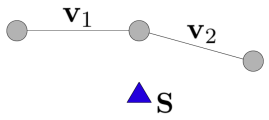

2. Find the two adjacent points in the measured dataset that lie closest to the simulated point of interest, S

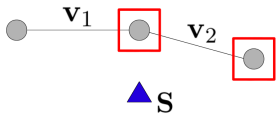

   Consider $\mathbf{v}_2$, the line segment vector that spans these two points. The point on the interpolated measured data set that lies closest to S will fall on $\mathbf{v}_2$

3. Calculate the normal vector $\mathbf{n}$ for the line segment $\mathbf{v}_2$, using $\mathbf{n} = \mathbf{v}_2 \times [\mathbf{0}, \mathbf{0}, \mathbf{1}]$ and normalise the result: $\mathbf{n}_u = \mathbf{n}/|\mathbf{n}|$

4. Define a vector r between S and the first of the two closest measured points

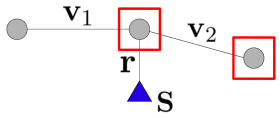

5. Calculate the Distance of Closest Approach (DCA) between the simulated point and the measured dataset, using the dot product of the vectors obtained in stages 3 & 4: DCA$= \mathbf{r} \cdot \mathbf{n}_u$

6. Repeat stages 2-5 to find the DCA for each calculated data point

7. Square, sum and square root all of the DCA values: this gives the Closest Approach Metric (CAM) which should be as small as possible

Figure 3.2 utilises many of the metrics detailed in Section 3.2.1 to compare the Eclipse versus MC data plotted in Figures 3.1. For all cost-functions shown in this plot, minimisation is desired, although in this case only the Closest Approach Metric appears to fall to a true minimum (which corresponds to the same optimum energy value of 6.0 MeV that would be selected via visual inspection). These initial results (Figure 3.2) suggest that, for MC model energy selection, the novel CAM developed here may be more robust that those previously considered by other groups [67], [69].

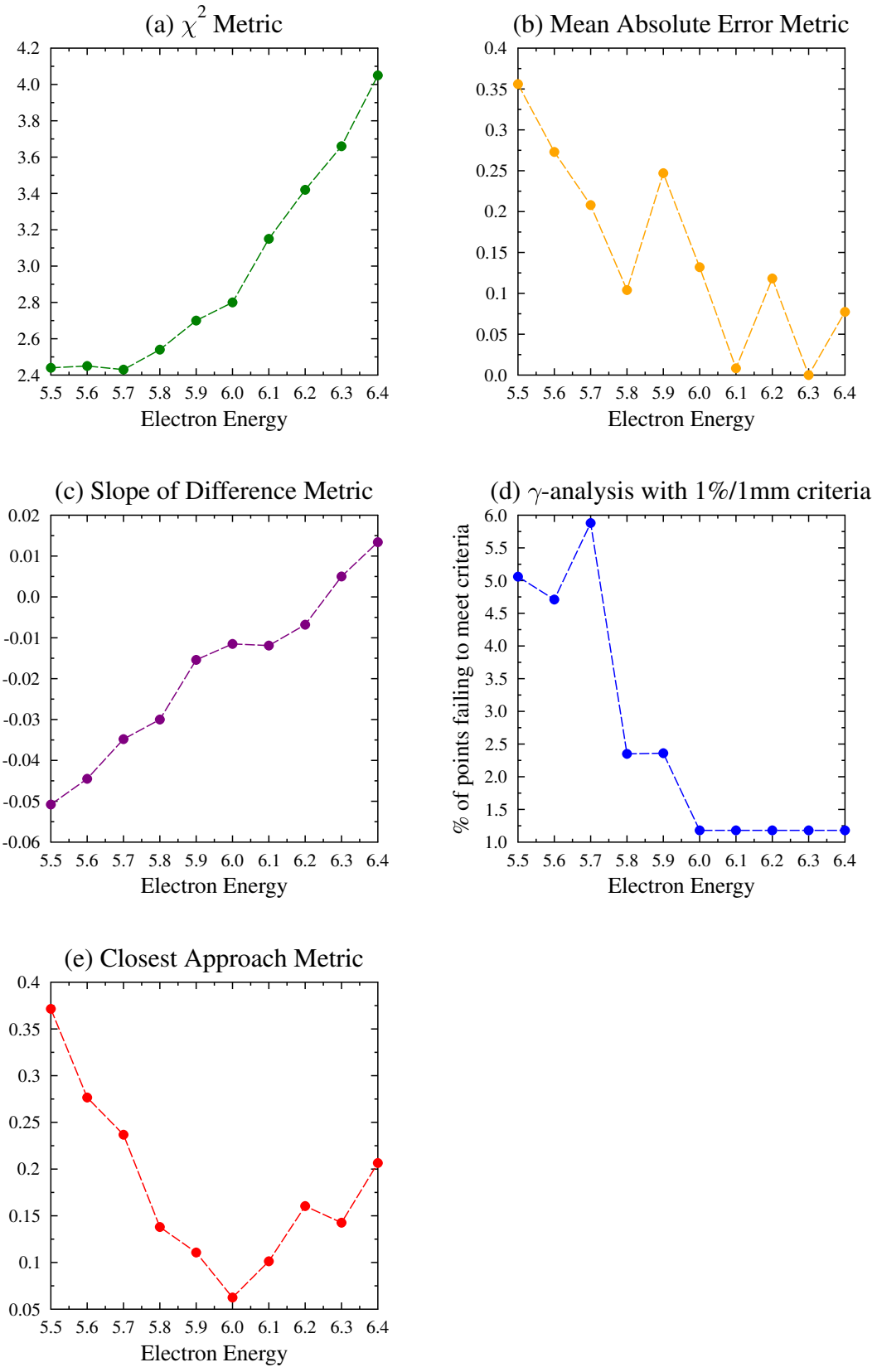

FIGURE 3.2: Optimising the input energy: plots to show the variation of different cost-functions with modelled electron energy.

3.3 Refining the model to accurately match the shape of measured lateral profiles

As shown in Figure 3.3(a), for a parallel beam of electrons striking the linac target, the central (on-axis) regions of simulated broad-field lateral profiles appear too intense relative to the profile peripheries (the regions most distal from the central axis).

This discrepancy between simulated and measured data could be attributable: (i) differences between the manufacturer's specifications and the geometry of the real linac flattening filter; (ii) angular variation amongst electrons hitting the linac target; (iii) an error in another unknown parameter or (iv) some combination of the above. The decision was taken to adjust a single parameter and ensure that the resulting beam model was fully validated against measured data for a very broad range of irradiation conditions. The selected parameter was the angular distribution of electrons striking the target[5].

In 2000, Sheikh-Bagheri *et al.* developed a BEAMnrc source module which, rather than assuming a parallel beam, allowed users to model an angular distribution amongst electrons hitting the target [71]. To achieve such a distribution, the source module (ISOURC=5) sweeps the primary electron (parallel circular) beam around an imaginary cone, with half-angle GAMMA or γ [72]. The module was here investigated for γ angles of 1°, 1.5° and 2°. In each case the radius of the beam (spot size) was maintained at 1 mm.

For a given field size, the same normalisation factor was applied to lateral profile data simulated at d_{max} (the depth of maximum dose, 1.5 cm for a 6 MV beam) and 10 cm deep, reflecting the fact that the same number of MU would have been applied during measurement of both sets of commissioning data. The mean value of normalisation factors calculated over the central 80% of the profiles was considered.

It is shown in Figure 3.3 that as the γ angle is increased, the periphery of the profile (the region most distal from the central axis) becomes more intense relative to the central (on-axis) region[6]. For the simulated angles $< 1.5°$, the central region of the profile is too intense relative to the peripheral region. For angles $> 1.5°$, the situation is reversed: 1.5° best matched the Eclipse data and was thus selected as the optimum γ angle.

[5] It is possible that the physical reality would have been better represented by instead adjusting the geometry of the flattening filter, but iterative geometrical optimisation of this form would undoubtedly have proved very time consuming. Additionally, it is likely that both methods would ultimately have similarly affected the distributions of off-axis and angular photon fluence post-flattening-filter.

[6] Due to the normalisaton method employed here - which takes an average over the central 80% of the profile - the central region correspondingly decreases in intensity.

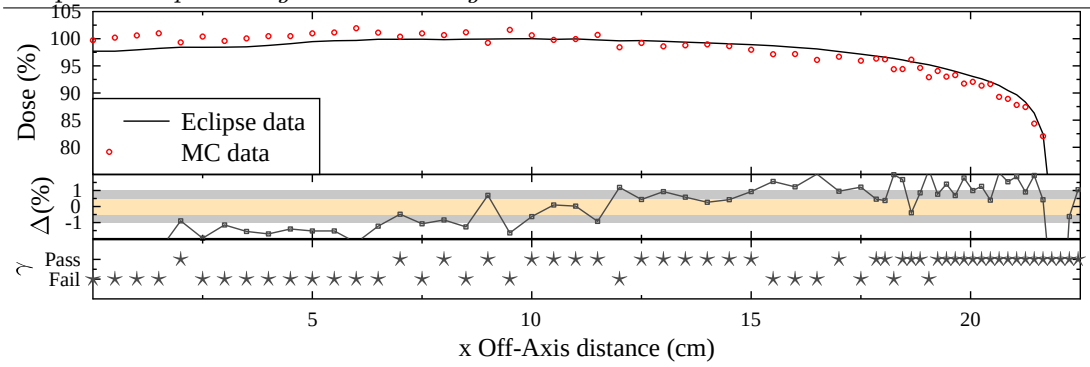

(a) $\gamma = 0°$

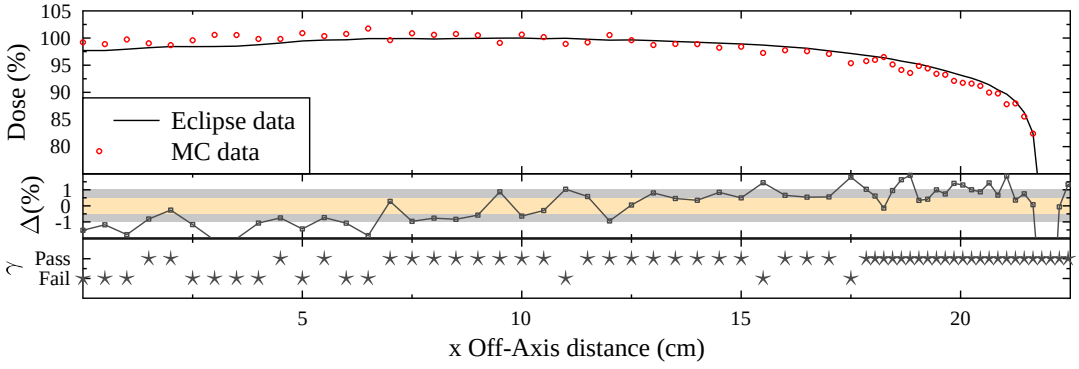

(b) $\gamma = 1°$

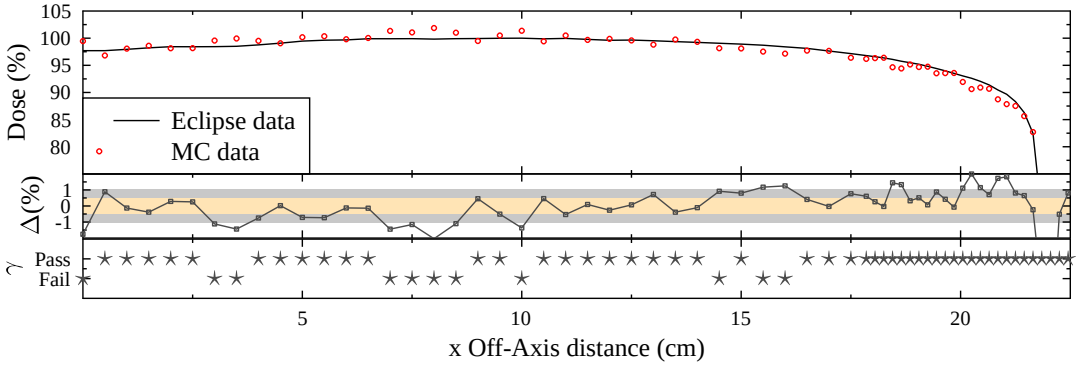

(c) $\gamma = 1.5°$

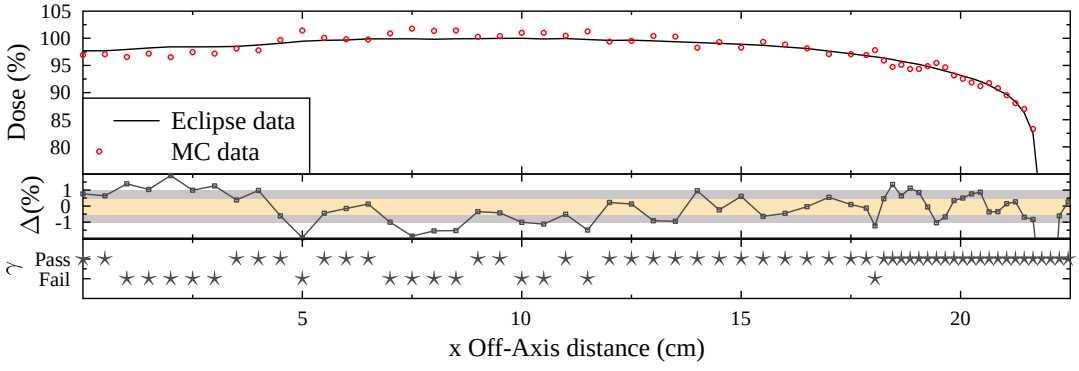

(d) $\gamma = 2°$

FIGURE 3.3: Comparison of simulated (MC) to measured (Eclipse) $40\times40\,\text{cm}^2$ field lateral profiles (obtained at a depth of 10 cm) for modelled electron beams with different γ angles. In each case a 6.0 MeV MC model, with 1 mm focal spot size is used. The central axes show the difference between the measured and simulated data points as a percentage of the local measured value, the lower axes show the voxels that passed/failed a gamma analysis criteria of 1%/1 mm. The statistical uncertainties associated with the Monte Carlo data points were all $< 0.5\%$ of the maximum dose.

3.4 Selecting the optimal radius for the electron beam

As described in Subsection 3.3, for the BEAMnrc source module here utilised (Source 5), the input electron beam is parallel and circular, such that the free parameters are the γ angle and the radius. Radii of 0.7 mm, 1 mm and 1.3 mm were tested for $40\times40\,cm^2$ field profiles at Dmax and 10 cm deep (results for 10 cm deep profiles shown in Figure 3.4). Very similar results were obtained for the 0.7 mm and 1 mm radii, whereas for the 1.3 mm spot size, the shoulder fall-off appeared to be too rapid. Further calculations utilise a beam radius of 1 mm.

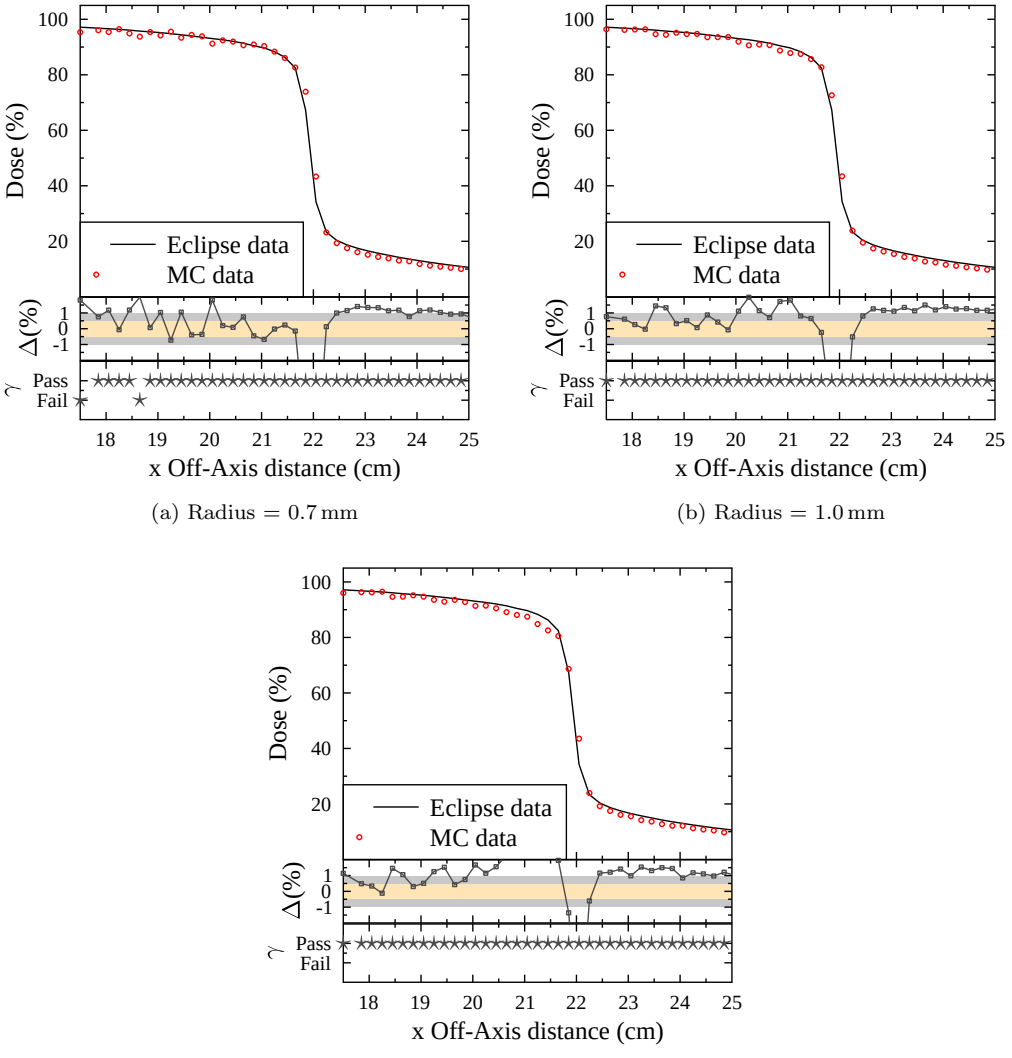

(a) Radius = 0.7 mm

(b) Radius = 1.0 mm

(c) Radius = 1.5 mm

FIGURE 3.4: Comparison of simulated (MC) to measured (Eclipse) $40\times40\,cm^2$ field lateral profiles (obtained at a depth of 10 cm) for modelled electron beams with different spot sizes. In each case a 6.0 MeV MC model, with 1.5° γ-angle was used. The central axes show the difference between the measured and simulated data points as a percentage of the local measured value, the lower axes show the voxels that passed/-failed a gamma analysis criteria of 1%/1 mm. The statistical uncertainties associated with the Monte Carlo data points were all $< 0.5\%$ of the maximum dose.

3.5 Testing the refined model for additional field sizes

In review, from the $10\times10\,\mathrm{cm}^2$ field PDDs, the optimal beam energy was found to be 6.0 MeV. From the $40\times40\,\mathrm{cm}^2$ lateral profiles, the optimal beam γ angle was found to be 1.5° and the optimal beam radius, 1 mm. The refined model (6.0 MeV, 1 mm beam radius, 1.5° γ angle) was then tested on PDDs for a $40\times40\,\mathrm{cm}^2$ field, with results shown in Figure 3.5, where agreement within 2% is obtained.

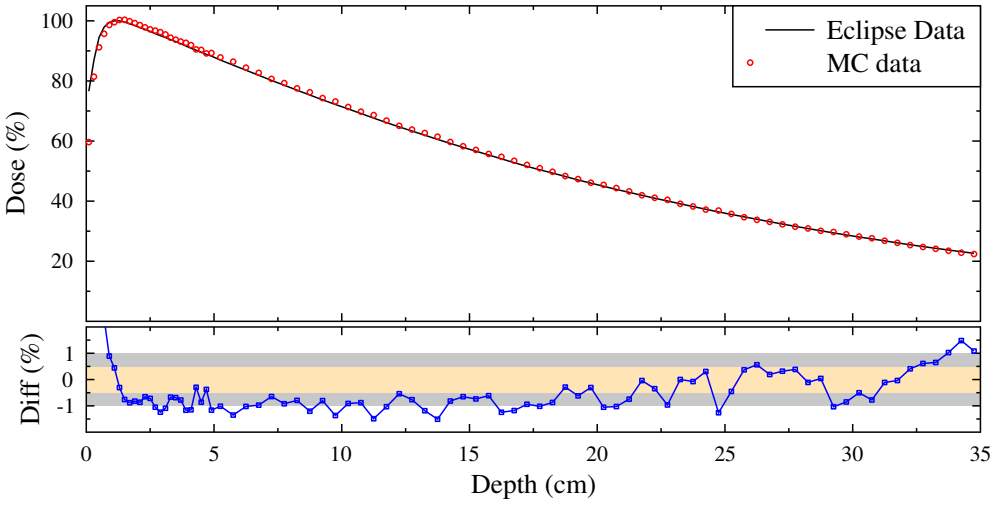

FIGURE 3.5: Comparison of simulated (MC) to measured (Eclipse) PDD data for 6.0 MeV MC model, $40\times40\,\mathrm{cm}^2$ field, 1 mm electron beam radius, 1.5° γ angle. The lower axes show the difference between the measured and simulated data points as a percentage of the local dose. Number of histories = 10 billion. The errors associated with the Monte Carlo data points were all $< 0.5\%$ of the maximum dose.

The model was also tested on $10\times10\,\mathrm{cm}^2$ and $3\times3\,\mathrm{cm}^2$ field lateral profiles (Figure 3.6).

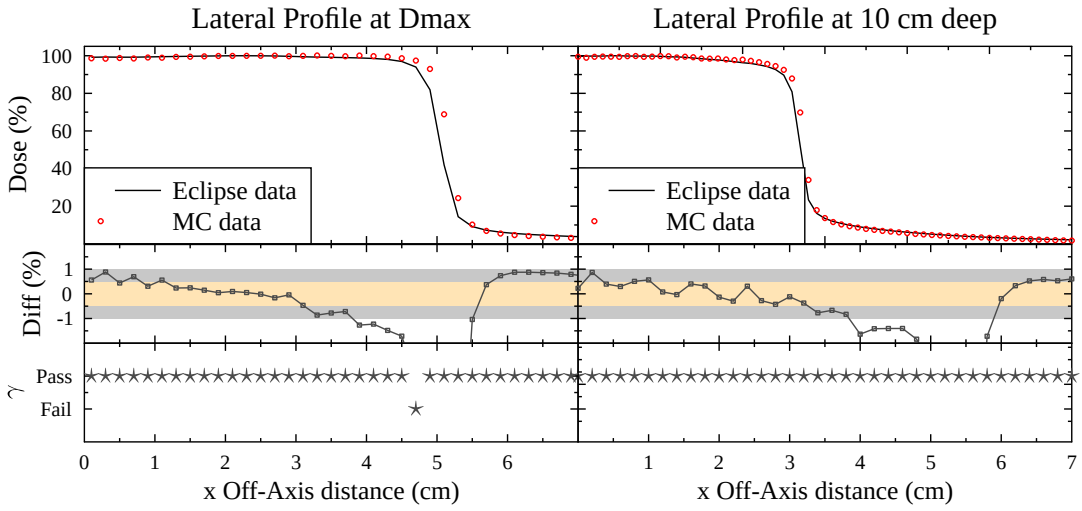

(a) $10\times10\,\mathrm{cm}^2$ field lateral profiles

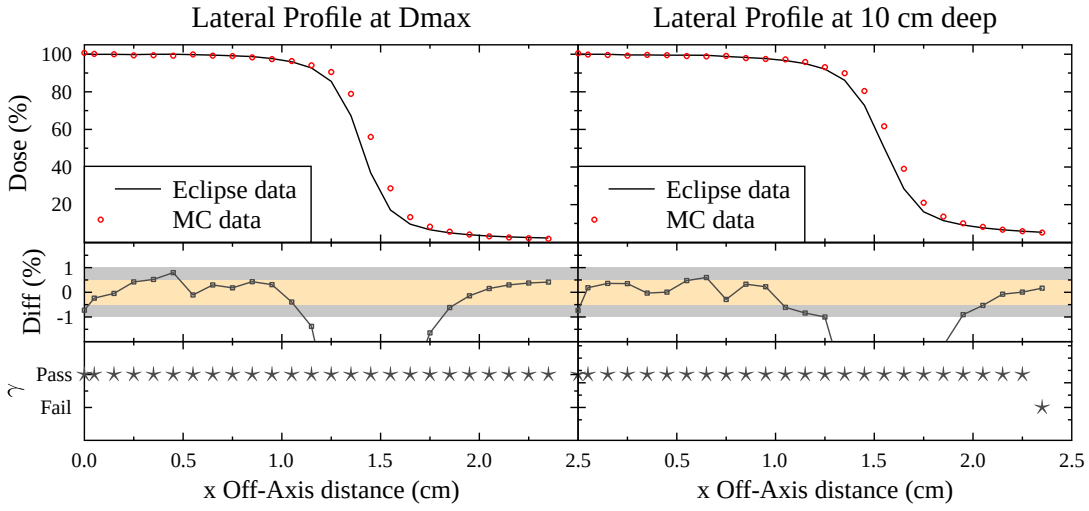

(b) $3\times3\,\mathrm{cm}^2$ field lateral profiles

FIGURE 3.6: Comparison of simulated (MC) to measured (Eclipse) lateral profile data for 6.0 MeV MC model, 1 mm focal spot size, 1.5° γ angle. For each field size, the second set of axes show the difference between the measured and simulated data points as a percentage of the maximum dose across the profile. The third set of axes show the voxels that passed/failed a gamma criteria of 2%/2 mm. The statistical uncertainties associated with the Monte Carlo data points were all $< 0.5\%$ of the maximum dose.

3.5.1 Inaccuracies in the linac Jaw Settings

Whilst plot 3.5 indicates excellent agreement between measured and simulated PDDs for the refined model (6.0 MeV, 1 mm electron beam radius, 1.5° γ angle), Figure 3.6 indicates a discrepancy between the modelled and measured FWHM field values. This discrepancy is due to the fact that the calculated FWHM values for the Eclipse profiles fall short of the nominal values requested at the linac[7].

3.5.1.1 Investigating jaw over-closure for Varian 2100 iX number 3 at the Oxford Cancer Centre

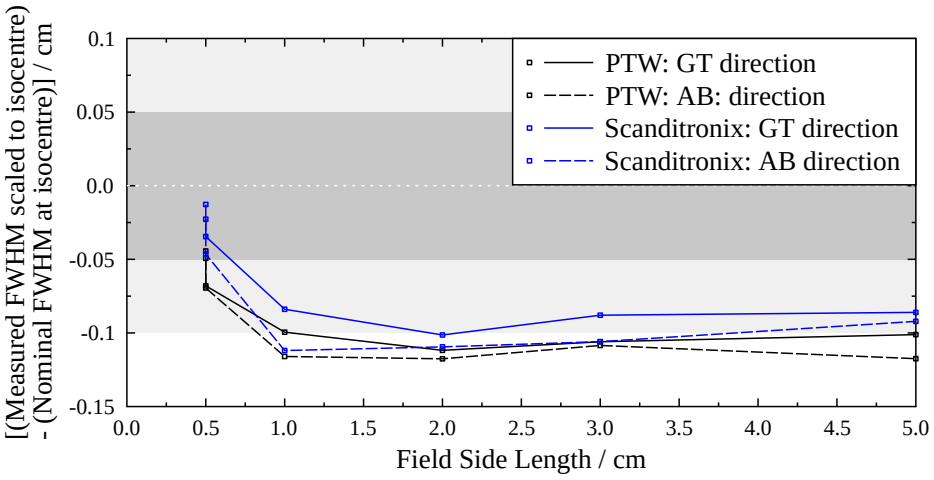

FIGURE 3.7: Investigating FWHM discrepancies for profiles measured at 5 cm deep: experimental results obtained from measurements using PTW and Scanditronix electron-diodes. For perfect agreement between the nominal FWHM field size requested at the linac and that measured using the diode / water-tank system, in this plot y-values would be expected to be zero for all field sizes.

Figure 3.7 indicates that, for electron diode data obtained using Varian linac 3 during this project (for all field sizes considered), measured FWHM values are consistently smaller than the nominal FWHM-based field sizes requested at the linac. For field sizes of $1\times1\,cm^2$ - $5\times5\,cm^2$, the linac jaws always over-close, such that the field size falls around 1 mm short at the isocentre. For the $0.5\times0.5\,cm^2$ field, the jaw over-closure effect is somewhat counterbalanced by a competing effect of source-occlusion: at such small fields overlapping penumbra mean that measurement of the FWHM gives a wider field than expected according to the projected collimator opening, due to a reduction in central axis dose.

[7]The movement of each jaw is controlled using a potentiometer, calibrated using light field position measurement (with verified light/radiation coincidence) during linac commissioning.

3.5.1.2 Adapting the Monte Carlo commissioning strategy

In order to test the performance of the refined Monte-Carlo model in the penumbral region of lateral profiles despite the jaw over-closure issue, FWHM values at the isocentre were calculated for PTW Ediode measurements obtained in this project. The simulated Monte Carlo FWHM values were then set to match these, rather than the nominal values requested at the linac.

In the case of a nominal $3\times 3\,\mathrm{cm}^2$ field, the PTW Ediode profile FWHM at the isocentre was found to be 2.90 cm. This value was set as an input in the Monte Carlo simulation, in order to produce Figure 3.8. Here excellent agreement between simulated and measured data is evident. For all further small field simulations, measured FWHM values were similarly used to set the simulated jaw positions.

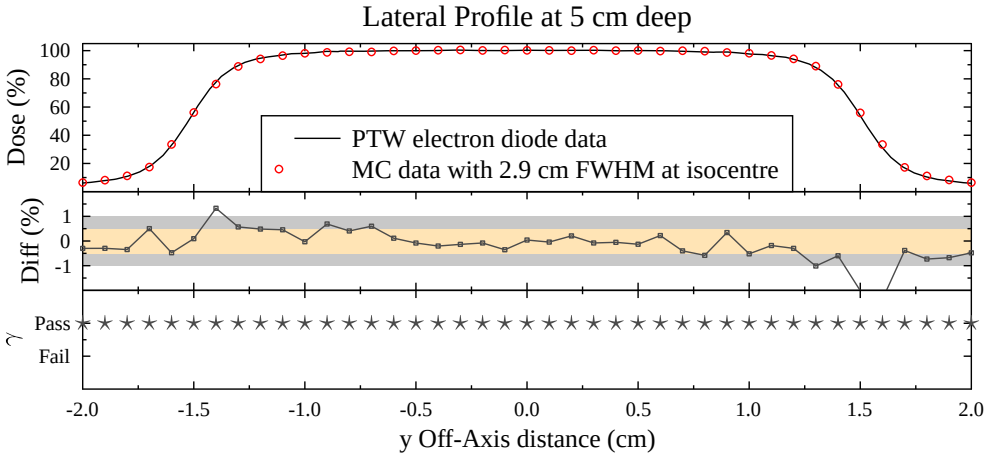

FIGURE 3.8: Comparison of simulated (MC) to measured (PTW electron diode) lateral profile data (obtained at a depth of 5 cm). The nominal linac field size was $3\times3\,\mathrm{cm}^2$, which resulted in an actual (and here simulated) field size of 2.898 cm. The 6.0 MeV MC model, with 1 mm electron beam radius and 1.5° γ angle was used. The statistical uncertainties associated with all Monte Carlo data points were $< 0.5\%$ of the maximum dose. The middle axes show the difference between the measured and simulated data points as a percentage of the local measured value. The lower axes demonstrate that all points passed 1%/1 mm gamma analysis criterion.

3.6 Verifying the model for small field applications

Thus far, this chapter has described the adaptation of the BEAMnrc linac model to fit measured data obtained during the process of linac commissioning at the Oxford Cancer Centre. The commissioning data only considered a minimum field side-length of 3 cm. This section demonstrates how additional small-field data (obtained using the method detailed in Section 3.1.2) was used to further verify the model.

It was first proposed by Francescon *et al.* [15], that the best way to optimise a MC linac model for small field applications might be to iteratively adjust the radius of the electron beam in order to attain excellent agreement between MOF values (see equation 3.1) calculated using simulations and measured experimentally. This method was implemented here (compete detector models were simulated) and ultimately a radius of 0.095 cm was selected as that which gave the best agreement across four different detectors (the MicroLion, PinPoint, Diode and Diamod) and two detector orientations. Measured and simulated $\mathrm{MOF}_{\mathrm{det}}^{f_{0.5\,\mathrm{cm}}}$ and $\mathrm{MOF}_{\mathrm{det}}^{f_{1\,\mathrm{cm}}}$ values for the final model (beam energy = 6.0 MeV, electron source γ-angle = 1.5° and radius = 0.095 cm) are compared in Figure 3.9.

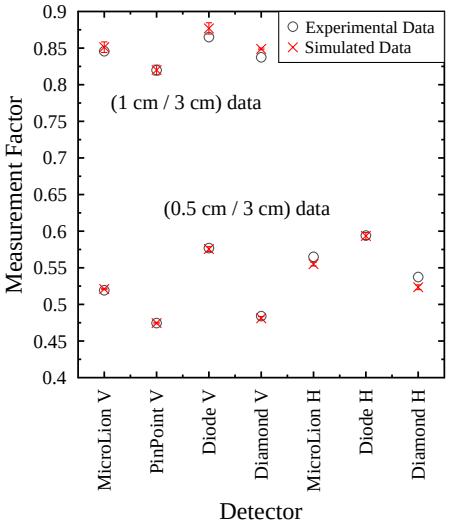

FIGURE 3.9: Comparison of simulated and measured 0.5 cm and 1 cm measurement factors. 'V' indicates vertical (parallel to beam central axis) detector orientation, 'H' indicates horizontal (perpendicular to beam central axis) detector orientation. Due to the long length of its sensitive volume (5 mm) the PinPoint was not utilised horizontally.

For a 0.5 cm field, the maximum percentage difference between Monte Carlo and experimental MOF data for vertically orientated detectors was 0.6%, while for a 1 cm field, the vertical detector maximum difference was 1.4%. Measurements were also made with detectors aligned horizontally, with their stems perpendicular to the beam axis. In this case simulated/measured differences of 2.6% and 1.8% were found for the Diamond detector and the MicroLion respectively. Further investigations using various collimator and detector rotations suggested that the pre-target electron beam was not rotationally symmetric as modelled, but instead, slightly elliptical. Such a discrepancy between the simulated and real linacs might be expected to affect the horizontal detector data more significantly than it would vertical detector data, due to the smaller beam's eye view cross-section presented by the detector in the horizontal case. Since ellipticity cannot be directly factored into the BEAMnrc electron source model used here (source 5) no further adjustment of the linac model was performed. Despite this limitation, however,

MOFs generated for 0.5 cm and 1 cm fields by Monte Carlo modelling of the linac and detector response are all accurate to better than 3% for four different detectors and two detector orientations.

Figures 3.10(a-d) show simulated and measured normalised x-axis lateral-profiles for a nominal 0.5 cm field; similar results were obtained for y-axis lateral profiles. For all detectors and both x-axis and y-axis profiles, discrepancies between simulated and measured profile full width half maximum (FWHM) values were <0.05 cm. Discrepancies between simulated and measured 20%:80% profile penumbral distances were all <0.02 cm.

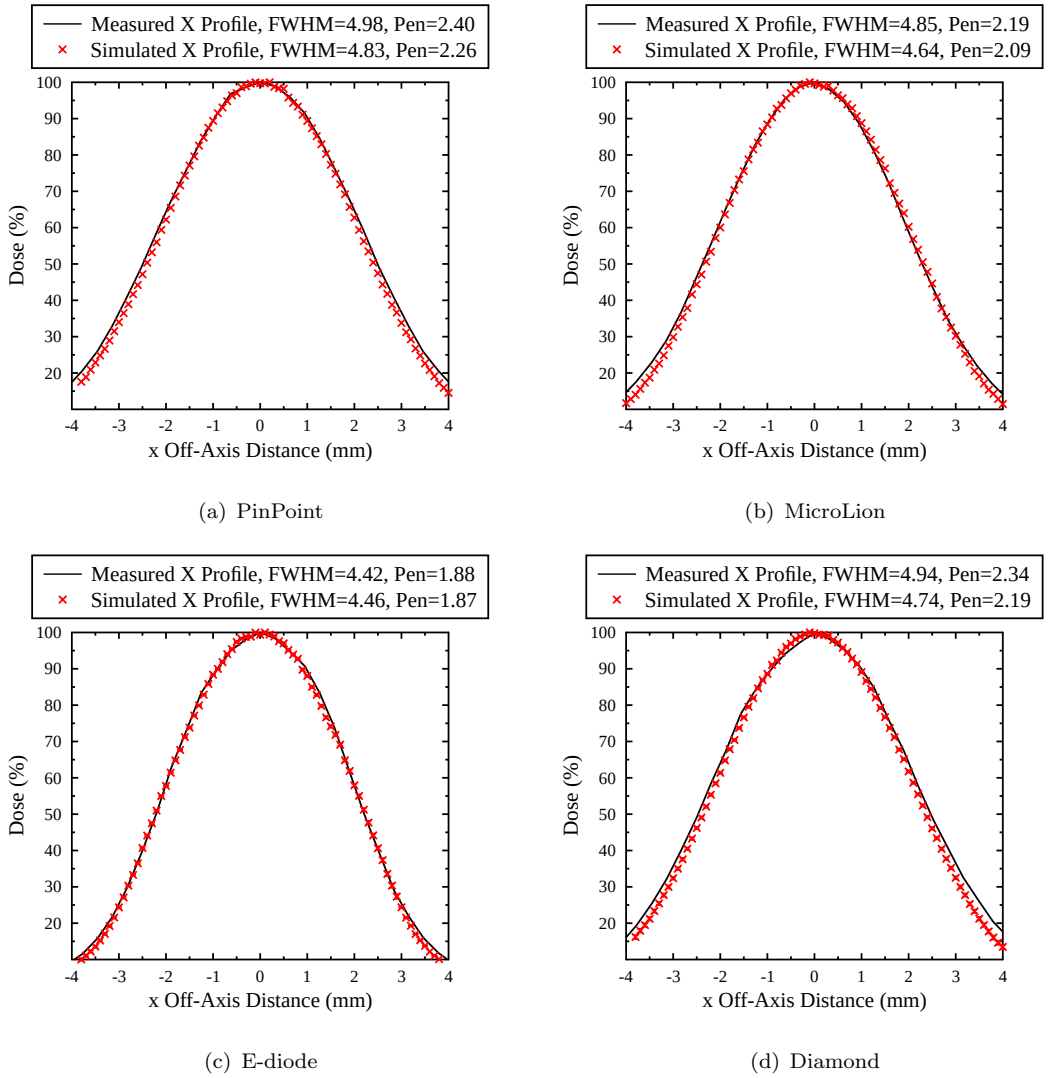

(a) PinPoint (b) MicroLion

(c) E-diode (d) Diamond

FIGURE 3.10: Comparison of simulated x-axis lateral profiles and those measured using various detectors for a nominal 0.5 cm field (with fixed jaw positions) at a depth of 5 cm. MC 1 s.d. statistical uncertainties are all <0.5% of maximum dose. Full width half maximum (FWHM) and 80% to 20% penumbral distances (Pen) are displayed in millimetres in the Figure legends.

For the final (small-field optimised) model, simulated and measured (a) lateral half-profiles and (b) PDDs, for a $40\times40\,\mathrm{cm}^2$ field are compared in Figures 3.11a and 3.11b and agree to within 2%/2 mm using a γ-analysis [68] criteria.

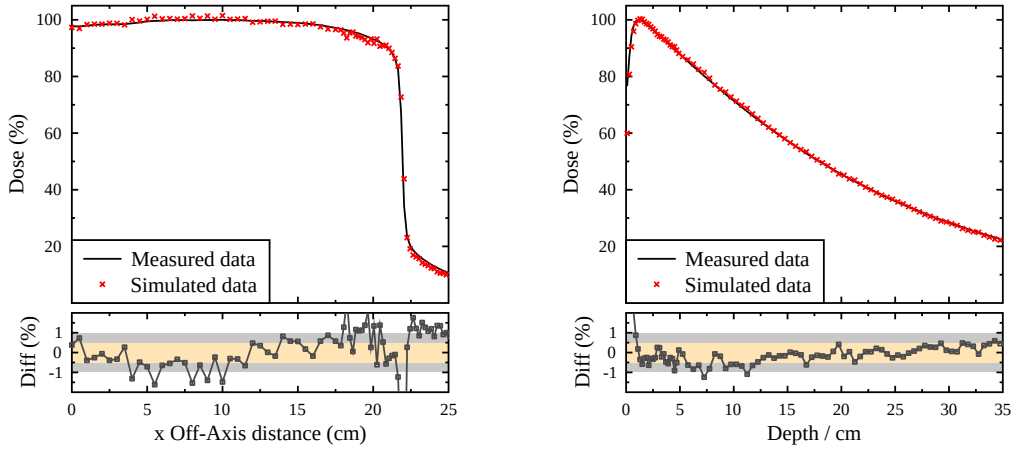

(a) X-axis profile at a depth of 10 cm. MC 1 s.d. uncertainties all <1% of maximum dose.

(b) PDD. MC 1 s.d. uncertainties all <0.5% of maximum dose.

FIGURE 3.11: Comparison of data simulated (in water) and measured (using the PTW Semiflex Ionisation Chamber) for a $40\times40\,\mathrm{cm}^2$ field.

Experimental uncertainties: in this work experimental uncertainties due to jaw position reproducibility were essentially eliminated through use of a fixed set of jaw positions for each small field size. All measurements were averaged over a series of at least three repeat readings, but short-term variation in linac output was found to be negligible. Via repeats of the same experiment at the start and the end of each measurement session, the combined uncertainty due to detector positioning and linac output fluctuation was estimated to be small (<0.5%).

Systematic uncertainties in the Monte Carlo simulations: Francescon *et al* [15] performed a detailed analysis of the systematic uncertainties in Monte Carlo simulations of detectors (including the PTW Ediode simulated in this study and a similar model of the PTW PinPoint) positioned centrally within a $0.5\times0.5\,\mathrm{cm}^2$ field. They considered possible discrepancies in cross-section, detector geometry and wall density (both relative to the manufacturer's specifications), estimating the total systematic uncertainty on their small field correction factors to be less than 0.7%.

3.7 Conclusions

This chapter demonstrates that the final 6 MV BEAMnrc linac model generated here (electron beam energy = 6.0 MeV, electron source γ-angle = 1.5°, radius = 0.095 cm) accurately represents the Eclipse beam model used at the Oxford Cancer Centre across a range of field sizes (from $40\times40\,cm^2$ to $3\times3\,cm^2$) to within 2%/2 mm. Furthermore, the MC model has been refined to mimic the performance of one particular treatment machine (Oxford Cancer Centre Varian 2100 iX number 3) under small-field conditions, accurately modelling MOF's for $0.5\times0.5\,cm^2$ and $1\times1\,cm^2$ fields to better than 3% for four different detectors and two detector orientations. Small systematic differences are evident in the small field profile penumbra[8], suggesting that a perfect representation of the physical reality of this particular linac has not quite been achieved. However, as no further direct comparisons between experimental and computational data are utilised in this thesis, this very slight systematic discrepancy should have negligible impact upon the results presented in the chapters that follow.

[8] See Figure 3.10, all measured penumbra are slightly larger than their simulated counterparts but agree to within 0.02 cm.

Chapter 4

Small field point-dose correction factors: a tenable solution?

4.1 Introduction

4.1.1 The IAEA/AAPM formalism for reference dosimetry in small static MV photon fields

For some time, the development of new protocols for small field dosimetry has been viewed by the radiotherapy community as a high priority. Standard Codes of Practice for reference dosimetry (e.g. IAEA TRS-398 [12] and AAPM TG-51 [73]) are based on broad radiation fields (typically, $10\times10\,\mathrm{cm}^2$) in which Lateral Electronic Equilibrium (LEE) holds. In small fields, however, LEE breaks down, preventing the direct use of dosimetric methods based on broad fields. For certain modern techniques this problem can be worsened by the inability of specialised non-standard delivery systems to generate broad field reference conditions.

To address these problems, an international working group was formed by the IAEA in collaboration with the AAPM. As outlined in Chapter 1, the first working group document was published in 2008 by Alfonso *et al* [25], who formalised a system linking small field dosimetry protocols back to broad-beam calibrations. For treatment machines unable to deliver standard $10\times10\,\mathrm{cm}^2$ beams, Alfonso *et al* introduced the concept of intermediate, machine specific reference (msr) fields. Absolute dosimetry for a small field may then be established by coupling the calibration of this msr field, rather than a conventional $10\times10\,\mathrm{cm}^2$ reference field, with additional correction factors specific to the clinical field under consideration.

Under the formulation of Alfonso et al (equation 1.25):

$$D^{f_{\text{clin}}}_{\text{w,Q}_{\text{clin}}} = D^{f_{\text{msr}}}_{\text{w,Q}_{\text{msr}}} \times \frac{M^{f_{\text{clin}}}_{\text{Q}_{\text{clin}}}}{M^{f_{\text{msr}}}_{\text{Q}_{\text{msr}}}} \times k^{f_{\text{clin}},f_{\text{msr}}}_{\text{Q}_{\text{clin}},\text{Q}_{\text{msr}}}$$

where $D^{f_{\text{x}}}_{\text{w,Q}_{\text{x}}}$ is the dose to a point of water in field x and $M^{f_{\text{x}}}_{\text{Q}_{\text{x}}}$ is the dosimeter measurement in field x (x $\in$ clin,msr). Here 'clin' is used to denote clinical fields, and 'msr' denotes machine specific reference fields; for treatment machines capable of generating a standard $10\times10\,\text{cm}^2$ reference field - as for the linacs utilised in this project - this is used as the msr. The small-field point-dose correction factor, $k^{f_{\text{clin}},f_{\text{msr}}}_{\text{Q}_{\text{clin}},\text{Q}_{\text{msr}}}$, is given by (equation 1.26):

$$k^{f_{\text{clin}},f_{\text{msr}}}_{\text{Q}_{\text{clin}},\text{Q}_{\text{msr}}} = \left[\frac{D^{f_{\text{clin}}}_{\text{w,Q}_{\text{clin}}}/M^{f_{\text{clin}}}_{\text{Q}_{\text{clin}}}}{D^{f_{\text{msr}}}_{\text{w,Q}_{\text{msr}}}/M^{f_{\text{msr}}}_{\text{Q}_{\text{msr}}}}\right]$$

4.1.2 Purpose of this work

In recent times many groups have investigated the variation of $k^{f_{\text{clin}},f_{\text{msr}}}_{\text{Q}_{\text{clin}},\text{Q}_{\text{msr}}}$ with field size, dosimeter and linac-type [13–15, 29–32]. This work builds upon this foundation and additionally considers the variation of $k^{f_{\text{clin}},f_{\text{msr}}}_{\text{Q}_{\text{clin}},\text{Q}_{\text{msr}}}$ with dosimeter position within the clinical field and dosimeter azimuthal angle. The methods of this chapter are entirely simulation based: the validated linac model of Chapter 3 is used in conjunction with complete virtual models of the four different detectors described in Chapter 2.

Three new $k^{f_{\text{clin}},f_{\text{msr}}}_{\text{Q}_{\text{clin}},\text{Q}_{\text{msr}}}$-related factors are introduced in order to investigate the perturbative effects of various dosimeter components/media. The last of these factors follows on from recent work by Scott *et al* [16], who demonstrated that small-field voxel response is largely determined by the mass density of the media involved, which has a greater influence on the small to large field ratio of voxel-response than does atomic number.

4.2 Methods

For $k^{f_{\text{clin}},f_{\text{msr}}}_{\text{Q}_{\text{clin}},\text{Q}_{\text{msr}}}$ values calculated in this chapter, the "point-like" structure considered was a $0.25\times0.25\times0.25\,\text{mm}^3$ water voxel located on the beam central axis at a depth of 5 cm (SSD=100 cm). For water voxels of this size, volume averaging effects were found to be insignificant for fields with side lengths of 0.5 cm or greater - that is $k^{f_{\text{clin}},f_{\text{msr}}}_{\text{Q}_{\text{clin}},\text{Q}_{\text{msr}}}$ remained constant for a $0.5\times0.5\,\text{cm}^2$ clinical field when test simulations using smaller point-like structures were carried out. Because $M^{f_{\text{clin}}}_{\text{Q}_{\text{clin}}}$ and $M^{f_{\text{msr}}}_{\text{Q}_{\text{msr}}}$ represent detector readings, it follows that if detector response is linearly proportional to the average dose absorbed

by the detector sensitive volume then the detector readings M in equation (1.26) can be replaced by these average detector doses in the clinical and msr fields.

$k^{f_{\text{clin}},f_{\text{msr}}}_{\text{Q}_{\text{clin}},\text{Q}_{\text{msr}}}$ may take a non-unit value for several reasons including:

1. volume averaging over the finite-sized sensitive region of the detector
2. perturbations in the particle or photon fluences due to non-sensitive dosimeter components
3. differences in the particle fluence and photon mean free path due to the (non-water) mass density of the sensitive medium

In order to explore these effects independently, three further $k^{f_{\text{clin}},f_{\text{msr}}}_{\text{Q}_{\text{clin}},\text{Q}_{\text{msr}}}$-related factors were formulated:

$$[k(D_{\text{vol}})]^{f_{\text{clin}},f_{\text{msr}}}_{\text{Q}_{\text{clin}},\text{Q}_{\text{msr}}} = \left[\frac{(D_{\text{vol}})^{f_{\text{clin}}}_{\text{w},\text{Q}_{\text{clin}}}/M^{f_{\text{clin}}}_{\text{Q}_{\text{clin}}}}{(D_{\text{vol}})^{f_{\text{msr}}}_{\text{w},\text{Q}_{\text{msr}}}/M^{f_{\text{msr}}}_{\text{Q}_{\text{msr}}}}\right] \tag{4.1}$$

$$[k(D_{\text{vol}}, M_{\text{sens}})]^{f_{\text{clin}},f_{\text{msr}}}_{\text{Q}_{\text{clin}},\text{Q}_{\text{msr}}} = \left[\frac{(D_{\text{vol}})^{f_{\text{clin}}}_{\text{w},\text{Q}_{\text{clin}}}/(M_{\text{sens}})^{f_{\text{clin}}}_{\text{Q}_{\text{clin}}}}{(D_{\text{vol}})^{f_{\text{msr}}}_{\text{w},\text{Q}_{\text{msr}}}/(M_{\text{sens}})^{f_{\text{msr}}}_{\text{Q}_{\text{msr}}}}\right] \tag{4.2}$$

$$[k(D_{\text{vol}}, M_{\text{sens},\rho=1})]^{f_{\text{clin}},f_{\text{msr}}}_{\text{Q}_{\text{clin}},\text{Q}_{\text{msr}}} = \left[\frac{(D_{\text{vol}})^{f_{\text{clin}}}_{\text{w},\text{Q}_{\text{clin}}}/(M_{\text{sens},\rho=1})^{f_{\text{clin}}}_{\text{Q}_{\text{clin}}}}{(D_{\text{vol}})^{f_{\text{msr}}}_{\text{w},\text{Q}_{\text{msr}}}/(M_{\text{sens},\rho=1})^{f_{\text{msr}}}_{\text{Q}_{\text{msr}}}}\right] \tag{4.3}$$

Their meanings are summarized in Table 4.1.

All three factors (equations 4.1-4.3) consider the dose D_{vol} absorbed by a volume of water having the same dimensions as the dosimeter sensitive region whereas the original $k^{f_{\text{clin}},f_{\text{msr}}}_{\text{Q}_{\text{clin}},\text{Q}_{\text{msr}}}$ considers the dose D absorbed by a point-like water structure. This change alone results in the new factor $[k(D_{\text{vol}})]^{f_{\text{clin}},f_{\text{msr}}}_{\text{Q}_{\text{clin}},\text{Q}_{\text{msr}}}$ of equation 4.1 and media-based dosimetric perturbations to be considered in the context of consistent volume-averaging for both the water structure and the dosimeter sensitive region.

A second change is made in equations 4.2 and 4.3, where each detector meter-reading M in equation 1.26 is replaced by a term M_{sens} simulated as the dose absorbed by the sensitive region of a simplified detector model,comprising of the sensitive volume alone. In this case non-sensitive detector components have been removed whereas in the original $k^{f_{\text{clin}},f_{\text{msr}}}_{\text{Q}_{\text{clin}},\text{Q}_{\text{msr}}}$ formalism each meter-reading was calculated as the dose absorbed by the sensitive region of a *complete* detector model. This second change and the associated factor $[k(D_{\text{vol}}, M_{\text{sens}})]^{f_{\text{clin}},f_{\text{msr}}}_{\text{Q}_{\text{clin}},\text{Q}_{\text{msr}}}$ of equation 4.2 allows the relative impact of the density and the atomic composition of the detector sensitive media to be studied in isolation from the rest of the detector.

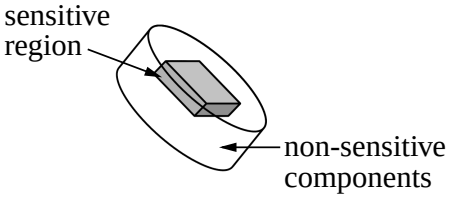

A simple model of a detector consists of (i) the sensitive region (for detectors that respond linearly, readings will be proportional to the average dose absorbed by this region) and (ii) the surrounding auxiliary components. In each row of the table, the left hand diagram shows the detector structure modelled, while the right hand diagram shows the water volume modelled.

$k^{f_{\text{clin}},f_{\text{msr}}}_{\text{Q}_{\text{clin}},\text{Q}_{\text{msr}}}$	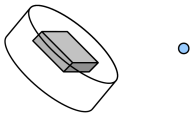	The standard Alfonso *et al* small-field correction factor, which considers dose to a point of water.
$[k(D_{\text{vol}})]^{f_{\text{clin}},f_{\text{msr}}}_{\text{Q}_{\text{clin}},\text{Q}_{\text{msr}}}$	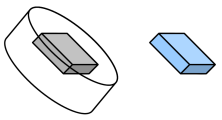	$k^{f_{\text{clin}},f_{\text{msr}}}_{\text{Q}_{\text{clin}},\text{Q}_{\text{msr}}}$ variant with consistent volume averaging enforced for the water structure and detector sensitive region.
$[k(D_{\text{vol}}, M_{\text{sens}})]^{f_{\text{clin}},f_{\text{msr}}}_{\text{Q}_{\text{clin}},\text{Q}_{\text{msr}}}$		$k^{f_{\text{clin}},f_{\text{msr}}}_{\text{Q}_{\text{clin}},\text{Q}_{\text{msr}}}$ variant with consistent volume averaging and a dosimeter modelled as comprising only the sensitive volume.
$[k(D_{\text{vol}}, M_{\text{sens},\rho=1})]^{f_{\text{clin}},f_{\text{msr}}}_{\text{Q}_{\text{clin}},\text{Q}_{\text{msr}}}$	 $\rho = 1$	$k^{f_{\text{clin}},f_{\text{msr}}}_{\text{Q}_{\text{clin}},\text{Q}_{\text{msr}}}$ variant with consistent volume averaging and a dosimeter modelled as comprising only the sensitive volume, whose mass density is set to be that of water (unity).

TABLE 4.1: $k^{f_{\text{clin}},f_{\text{msr}}}_{\text{Q}_{\text{clin}},\text{Q}_{\text{msr}}}$-related factors: summary definitions.

Finally, a third change is made in equation (4.3), replacing M_{sens} with $M_{\text{sens},\rho=1}$ - again the dose absorbed by the sensitive volume-only detector model, but now with the mass density of the sensitive volume set to unity. Consequently the difference between $[k(D_{\text{vol}}, M_{\text{sens}})]^{f_{\text{clin}},f_{\text{msr}}}_{\text{Q}_{\text{clin}},\text{Q}_{\text{msr}}}$ and $[k(D_{\text{vol}}, M_{\text{sens},\rho=1})]^{f_{\text{clin}},f_{\text{msr}}}_{\text{Q}_{\text{clin}},\text{Q}_{\text{msr}}}$ describes the impact of the density of the sensitive region, independent of changes in its atomic composition.

Changing a material's mass density has the potential to change δ, a 'density effect'

correction term, in the collisional mass stopping power equation (equation 1.6) for electrons and positrons [62]. As a charged particle passes through a medium, it causes that medium to become polarised, which in turn decreases the electromagnetic field acting on the particle so that its stopping power is reduced. The strength of this effect depends on the density of the medium. In order to investigate the effects of δ on $[k(D_{\text{vol}}, M_{\text{sens},\rho=1})]^{f_{\text{clin}},f_{\text{msr}}}_{\text{Q}_{\text{clin}},\text{Q}_{\text{msr}}}$, two new sets of cross-section files were generated using egs_gui [61]:

1. a set where δ was maintained as that corresponding to the original non-unity density of the sensitive medium.
2. a set where δ was re-calculated (using the NIST ESTAR website[1]) for sensitive media with the original chemical composition, but altered (unit) density

In the first case, the cross-section files corresponded to new media with altered mass density, but with the mass radiological (interaction) properties of the old media maintained, *as per* the method of Scott *et al* [16]. In the second case, the effects of changing the medium's mass density were propagated fully through to the δ correction and hence the medium's interaction properties.

This work also investigates the variation of $k^{f_{\text{clin}},f_{\text{msr}}}_{\text{Q}_{\text{clin}},\text{Q}_{\text{msr}}}$ with dosimeter position within the clinical field, and with dosimeter azimuthal angle relative to the beam axis. For all Monte Carlo simulations the detectors reference position is taken as 5 cm deep on-axis within a large virtual water phantom, set at an SSD of 100 cm from the virtual source, as for the experimental case.

4.3 Results

4.3.1 Variation with field size of $k^{f_{\text{clin}},f_{3\times3}}_{\text{Q}_{\text{clin}},\text{Q}_{3\times3}}$-related factors

The variation of Monte Carlo calculated $k^{f_{\text{clin}},f_{3\times3}}_{\text{Q}_{\text{clin}},\text{Q}_{3\times3}}$ factors with square field size is shown in Figure 4.1(a) for four different detectors. $k^{f_{\text{clin}},f_{3\times3}}_{\text{Q}_{\text{clin}},\text{Q}_{3\times3}}$ values > 1 indicate that a dosimeter is under responding in small fields relative to a point water dose, whereas $k^{f_{\text{clin}},f_{3\times3}}_{\text{Q}_{\text{clin}},\text{Q}_{3\times3}}$ values < 1 indicate that a dosimeter is over-responding.

Figure 4.1(a) shows an Ediode over-response for small fields, whereas the PinPoint and MicroLion under-responded, in agreement with results presented in Figure 7 of Francescon *et al*.

[1] http://physics.nist.gov/PhysRefData/Star/Text/ESTAR.html

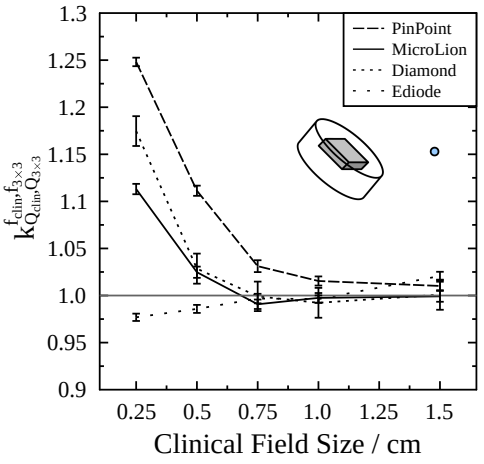

(a) $k^{f_{\text{clin}},f_{\text{msr}}}_{Q_{\text{clin}},Q_{\text{msr}}}$: the standard Alfonso *et al* small-field correction factor.

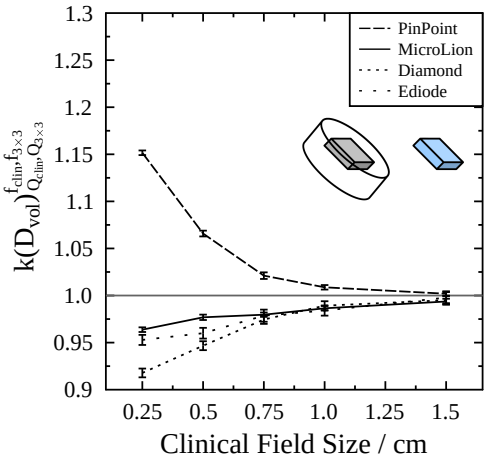

(b) $[k(D_{\text{vol}})]^{f_{\text{clin}},f_{\text{msr}}}_{Q_{\text{clin}},Q_{\text{msr}}}$: a version of $k^{f_{\text{clin}},f_{\text{msr}}}_{Q_{\text{clin}},Q_{\text{msr}}}$ with consistent volume averaging enforced for the water structure and detector sensitive region

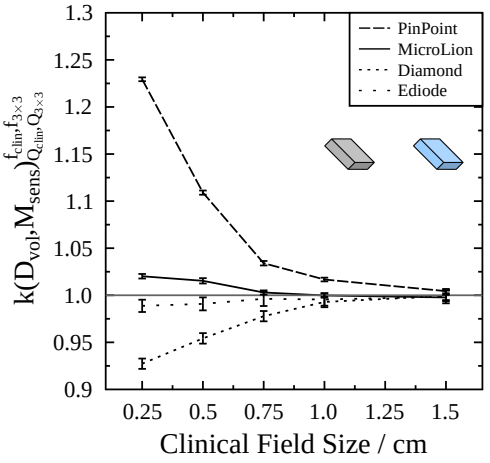

(c) $[k(D_{\text{vol}}, M_{\text{sens}})]^{f_{\text{clin}},f_{\text{msr}}}_{Q_{\text{clin}},Q_{\text{msr}}}$: a version of $k^{f_{\text{clin}},f_{\text{msr}}}_{Q_{\text{clin}},Q_{\text{msr}}}$ with consistent volume averaging and also a dosimeter model that has been stripped of all non-sensitive components

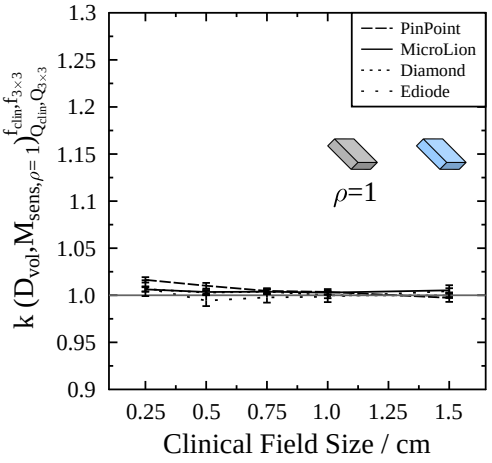

(d) $[k(D_{\text{vol}}, M_{\text{sens},\rho=1})]^{f_{\text{clin}},f_{\text{msr}}}_{Q_{\text{clin}},Q_{\text{msr}}}$: a version of $k^{f_{\text{clin}},f_{\text{msr}}}_{Q_{\text{clin}},Q_{\text{msr}}}$ with consistent volume averaging, a dosimeter model that has been stripped of all non-sensitive components *and* the mass density of the sensitve media set to unity

FIGURE 4.1: Plots of $k^{f_{\text{clin}},f_{\text{msr}}}_{Q_{\text{clin}},Q_{\text{msr}}}$ and related k factors versus field size. The selected machine specific reference field size (msr) was $3\times3\text{cm}^2$. Error bars show $\pm$ 1 standard deviation statistical uncertainties. The two sub figures towards the top right of each plot represent the sensitive detector volume surrounded by other material (left) and water volume (right) for which doses are calculated when determining the k factor.

The $[k(D_{\text{vol}})]^{f_{\text{clin}},f_{\text{msr}}}_{Q_{\text{clin}},Q_{\text{msr}}}$ factor of equation 4.1 represents the response of each full detector relative to a purely water equivalent version of that detector, and is plotted against field size in Figure 4.1(b). Since volume averaging correction factors are defined as a ratio between dose to a point and dose to the detector's sensitive volume, departures of this factor from unity are not due to volume averaging effects, which have been studied extensively, but are rather due to less well characterised perturbations caused by the media from which each detector is constructed. From Figure 4.1(b) it is clear that the

Ediode, diamond detector and MicroLion all over-respond compared to water, whereas the PinPoint under-responds. This means that the MicroLion under-response shown in Figure 4.1(a) and observed by Francescon et al [15] is due to dose averaging within its sensitive volume, and that when the dose absorbed by the sensitive volume is considered against the dose absorbed by an equivalent volume of water, the detector over-responds.

In Figure 4.1(c) the variation of $[k(D_{\text{vol}}, M_{\text{sens}})]^{f_{\text{clin}},f_{\text{msr}}}_{\text{Q}_{\text{clin}},\text{Q}_{\text{msr}}}$ with clinical field size is plotted. The $[k(D_{\text{vol}}, M_{\text{sens}})]^{f_{\text{clin}},f_{\text{msr}}}_{\text{Q}_{\text{clin}},\text{Q}_{\text{msr}}}$ factor of equation 4.2 compares the dose absorbed by simplified detector models consisting of sensitive volumes only to the dose absorbed by water-structures with the same dimensions as the detector sensitive volumes. Thus, this figure shows that, in isolation, the sensitive region of the diamond detector over-responds relative to the same volume of water. In fact, most of the over-response of the complete diamond detector shown in Figure 4.1(b) can be attributed to the over-response of the sensitive volume in isolation (Figure 4.1(c)). The opposite is true of the MicroLion: in total, this detector over-responds ($[k(D_{\text{vol}})]^{f_{\text{clin}},f_{\text{msr}}}_{\text{Q}_{\text{clin}},\text{Q}_{\text{msr}}} < 1$), but in isolation the sensitive volume under-responds ($[k(D_{\text{vol}}, M_{\text{sens}})]^{f_{\text{clin}},f_{\text{msr}}}_{\text{Q}_{\text{clin}},\text{Q}_{\text{msr}}} > 1$ - see Figure 4.1(b) versus 4.1(c)). The complete PinPoint detector under-responds (Figure 4.1(b)), a behaviour that is exacerbated when the sensitive volume is considered in isolation (Figure 4.1(c)). In the case of the Ediode, the complete detector over-reads, as does the sensitive volume in isolation although to a lesser-extent. The data presented in Figure 4.1(c) show that isolated sensitive volumes with less than unit density under-read while isolated sensitive volumes with greater than unit density over-read - results that agree with the recent work of Scott *et al* [16] who found that inter-detector variations in small-field dosimetric response can largely be attributed to the mass densities of the media involved.

Variation of the $[k(D_{\text{vol}}, M_{\text{sens},\rho=1})]^{f_{\text{clin}},f_{\text{msr}}}_{\text{Q}_{\text{clin}},\text{Q}_{\text{msr}}}$ factor of equation 4.3 with field size is plotted in Figure 4.1(d). In simulations of $[k(D_{\text{vol}}, M_{\text{sens},\rho=1})]^{f_{\text{clin}},f_{\text{msr}}}_{\text{Q}_{\text{clin}},\text{Q}_{\text{msr}}}$ the true chemical compositions and mass radiological properties of the sensitive volume are maintained but its mass density is set to unity, and the response of the unit density sensitive volume is considered relative to the response of a water-structure with the same dimensions. The $[k(D_{\text{vol}}, M_{\text{sens},\rho=1})]^{f_{\text{clin}},f_{\text{msr}}}_{\text{Q}_{\text{clin}},\text{Q}_{\text{msr}}}$ correction factors shown in Figure 4.1(d) are much closer to unity than the $[k(D_{\text{vol}}, M_{\text{sens}})]^{f_{\text{clin}},f_{\text{msr}}}_{\text{Q}_{\text{clin}},\text{Q}_{\text{msr}}}$ correction factors shown in Figure 4.1(c): in the case of the PinPoint detector, for a square clinical field with side length 0.25cm, $[k(D_{\text{vol}}, M_{\text{sens}})]^{f_{\text{clin}},f_{\text{msr}}}_{\text{Q}_{\text{clin}},\text{Q}_{\text{msr}}} = 1.224$ whereas $[k(D_{\text{vol}}, M_{\text{sens},\rho=1})]^{f_{\text{clin}},f_{\text{msr}}}_{\text{Q}_{\text{clin}},\text{Q}_{\text{msr}}} = 1.016$. These numerical data (and all data shown in Figure 4.1(d)) were simulated using the first set of cross-section files described in Section 4.2. In these cross section files, the mass density of the sensitive media was changed, but its original mass radiological properties were maintained. Results simulated using the second set of cross-section files, where the polarisation density effect was re-calculated to fully account for the density change (in terms of interaction probabilities), agreed with the data presented in Figure 4.1(d) to

within 2 s.d. of the statistical uncertainties of the simulations. Consequently, it is clear that it is the effect of mass density on photon mean free path that is important in the determination of $k_{Q_{clin},Q_{3\times3}}^{f_{clin},f_{3\times3}}$, rather than the effect of mass density on the electron/positron stopping-power via medium polarisation.

It should be noted that the mass density of detector components other than the sensitive volume can also influence detector response. For example, the over-response of the Ediode is due partly to its sensitive medium having density $>$ unity ($\rho_{\text{silicon}} = 2.33\,\text{g/cm}^3$) but also partly due to the addition of extra, dense media (Figure 4.1(b) versus Figure 4.1(c), in particular the large block of silicon underlying the small sensitive region is problematic). Perhaps most interesting is the case of the MicroLion detector, for which the addition of non-sensitive material with mass density greater than unity has the potential to improve the under-response of the low density sensitive volume ($\rho_{\text{isooctane}} = 0.688\,\text{g/cm}^3$); however the MicroLion graphite electrodes ($\rho_{\text{graphite}} = 1.85\,\text{g/cm}^3$) contain so much high density material, that the complete detector actually over-responds. Consequently the MicroLion might be improved by removing a proportion of its high density graphite or, alternatively, by building additional media with density < 1 into the design.

The potential of density-compensating detector design modifications to reduce the requirement for small-field dosimetric correction factors is highlighted in Table 4.2.

4.3.2 Variation of $k_{Q_{0.5},Q_3}^{f_{0.5},f_3}(\underline{r})$ with off-axis position ($\underline{r}$)

Figure 4.2 shows the variation of $k_{Q_{0.5},Q_3}^{f_{0.5},f_3}(\underline{r})$ with clinical field off-axis position $\underline{r}$, where

$$k_{Q_{0.5},Q_3}^{f_{0.5},f_3}(\underline{r}) = \left[\frac{D_{w,Q_{0.5\times0.5}}^{f_{0.5\times0.5}}(\underline{r})/M_{Q_{0.5\times0.5}}^{f_{0.5\times0.5}}(\underline{r})}{D_{w,Q_{3\times3}}^{f_{3\times3}}/M_{Q_{3\times3}}^{f_{3\times3}}}\right] \tag{4.4}$$

in which $D_{w,Q_{3\times3}}^{f_{3\times3}}$ and $M_{Q_{3\times3}}^{f_{3\times3}}$ are as usual calculated at the centre of the ($3 \times 3\,\text{cm}^2$) machine specific reference field, while $D_{w,Q_{0.5\times0.5}}^{f_{0.5\times0.5}}(\underline{r})$ and $M_{Q_{0.5\times0.5}}^{f_{0.5\times0.5}}(\underline{r})$ are calculated at $\underline{r}$ from the centre of a $0.5 \times 0.5\,\text{cm}^2$ field. Detectors were scanned off-axis at 0.1 cm increments in three different directions along the lines $x = 0$, $y = 0$ and $x = y$.

The variation of calculated $k_{Q_{clin},Q_{msr}}^{f_{clin},f_{msr}}(\underline{r})$ value with off-axis distance is plotted in Figure 4.2 and is consistent with the results of Crop *et al* [14], who found that PinPoint chamber (wall, air-water, volume and total) perturbation factors changed with off-axis distance in small fields, and with data of Scott *et al* [16], showing variation of a (water voxel)/(detector-media voxel) dose factor with off-axis distance.

Dosimeter	**Mass density of sensitive volume**	**Mass density of additional components**	**Do additional components worsen or improve complete response?**
Diamond	> 1 (diamond, ρ =3.52 g/cm^3)	≈ 1 (polystyrene with density similar to water)	Little change
Ediode	> 1 (silicon, ρ =2.33 g/cm^3)	> 1 (additional silicon underlying sensitive volume)	Worsen
MicroLion	< 1 (isooctane, ρ =0.69 g/cm^3)	> 1 (graphite electrode, ρ =1.85 g/cm^3)	Improve, but if less electrode material were used, an even better response would be obtained
PinPoint	$<< 1$ (air, ρ =0.0013 g/cm^3)	> 1 (steel inner electrode with density ρ =8.06 g/cm^3, and graphite outer electrode with density ρ =1.85 g/cm^3)	Improve, but further dense material would improve the response even more.

TABLE 4.2: The influence of mass density on dosimeter response.

However, Figure 4.2 also demonstrates that $k_{Q_{0.5},Q_3}^{f_{0.5},f_3}(\underline{r})$ depends on both the distance moved off axis and the direction of the move, since values are not the same for detectors scanned across $x = 0$, $y = 0$ and $x = y$ profiles. This behaviour can be attributed to the difference in height and thus penumbra width between the linac x and y jaws, and the distance remaining to the field edge when moving diagonally rather than along the x or y axis.

4.3.3 Variation of $k_{Q_{0.5},Q_3}^{f_{0.5},f_3}(\theta)$ with detector azimuthal angle (θ)

Figure 4.3a-d shows the variation of $k_{Q_{0.5},Q_3}^{f_{0.5},f_3}(\theta)$ with detector azimuthal angle (θ), where

$$k_{Q_{0.5},Q_3}^{f_{0.5},f_3}(\theta) = \left[\frac{D_{w,Q_{0.5\times0.5}}^{f_{0.5\times0.5}}(\theta)/M_{Q_{0.5\times0.5}}^{f_{0.5\times0.5}}(\theta)}{D_{w,Q_{3\times3}}^{f_{3\times3}}/M_{Q_{3\times3}}^{f_{3\times3}}} \right] \tag{4.5}$$

in which $D_{w,Q_{0.5\times0.5}}^{f_{0.5\times0.5}}(\theta)$ and $M_{Q_{0.5\times0.5}}^{f_{0.5\times0.5}}(\theta)$ are calculated at the centre of a $0.5 \times 0.5\,\text{cm}^2$ field, with the axis of the detector lying at θ to the beam axis (Figure (e)) while $D_{w,Q_{3\times3}}^{f_{3\times3}}$ and $M_{Q_{3\times3}}^{f_{3\times3}}$ are calculated at the centre of a $3 \times 3\,\text{cm}^2$ field with the detector conventionally aligned with the beam axis. Each dosimeter was rotated about the y-axis through

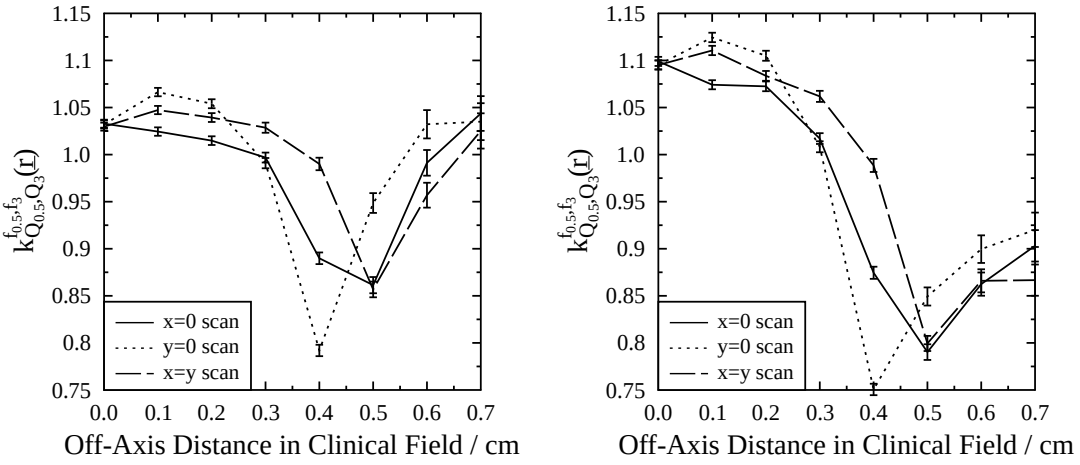

(a) Diamond Detector

(b) PinPoint Detector

FIGURE 4.2: Plots showing the simulated variation of detector $k^{f_{0.5},f_3}_{Q_{0.5},Q_3}(\underline{r})$ with off-axis position ($\underline{r}$) in a $0.5\times0.5\,cm^2$ field. The selected machine specific reference field size (msr) was $3\times3\,cm^2$. Error bars show 1 s.d. statistical uncertainties.

various azimuthal angles, so a 90° rotation aligns the axis of the dosimeter with the x-axis in the linac co-ordinate system.

Figure 4.3a-d also shows the change with θ of the $[k(D_{vol})]^{f_{0.5},f_3}_{Q_{0.5},Q_3}(\theta)$ factor, which represents the variation of the ratio of doses absorbed by the detector sensitive volume and an equivalent volume of water surrounded entirely by water.

The data show that $k^{f_{0.5},f_3}_{Q_{0.5},Q_3}$ and $[k(D_{vol})]^{f_{0.5},f_3}_{Q_{0.5},Q_3}$ change with θ, as well as with field-size and off-axis position. Although the variation with θ is less than the variation with field-size, it too appears to depend on the mass density of the detector sensitive volume.

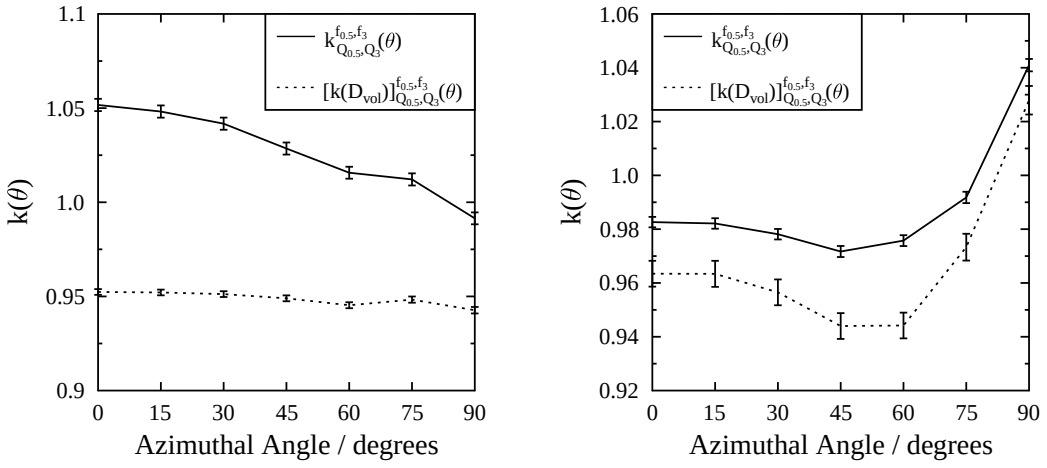

(a) Diamond

(b) Ediode

(c) MicroLion

(d) PinPoint

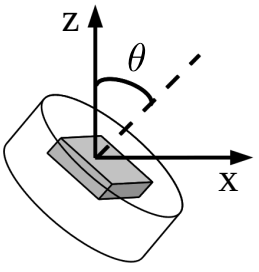

(e) A detector orientated at azimuthal angle θ.

FIGURE 4.3: MC-based investigation of the variation of $k^{f_{0.5},f_3}_{Q_{0.5},Q_3}(\theta)$ and $[k(D_{vol})]^{f_{0.5},f_3}_{Q_{0.5},Q_3}(\theta)$ with θ. Error bars show 1 s.d. statistical uncertainties.

4.4 Conclusions

This chapter has shown that, according to the formulation of Alfonso *et al* [25] single detector position measurements within small fields require $k_{Q_{clin},Q_{msr}}^{f_{clin},f_{msr}}$ correction factors that depend strongly on detector design, field size, detector position and detector azimuthal angle.

The correction factors calculated here are consistent in magnitude with those published by Francescon *et al* [32]. For example, for the same detector model (PTW diode 60012) and a broadly similar experimental set-up[2], Francescon *et al* published a value of ≈0.97 for $k_{Q_{0.5},Q_{10}}^{f_{0.5},f_{10}}$. Here a $k_{Q_{0.5},Q_3}^{f_{0.5},f_3}$ value of 0.98 was calculated. For the PTW MicroLion 31018, the $k_{Q_{0.5},Q_3}^{f_{0.5},f_3}$ value calculated here was 1.03. For this dosimeter, Francescon *et al* obtained a $k_{Q_{0.5},Q_{10}}^{f_{0.5},f_{10}}$ value of ≈1.02. The largest correction factor obtained by Francescon *et al* was $k_{Q_{0.5},Q_{10}}^{f_{0.5},f_{10}} \approx 1.13$ for the PTW PinPoint chamber 31014. In this work (where a smaller minimum field size of $0.25\times0.25\,cm^2$ was considered), the largest correction factor was $k_{Q_{0.25},Q_3}^{f_{0.25},f_3} = 1.25$ for the PinPoint 31006. Numerous other studies in the literature also indicate that for very small fields (∼ 0.5 cm across) point dose measurements obtained using different dosimeters (ion chambers, diodes and diamond detectors) can vary by tens of percent even for small sensitive volumes of 1-3 mm in diameter [74–76].

Accurate $k_{Q_{clin},Q_{msr}}^{f_{clin},f_{msr}}$ values are not easy to obtain, their determination typically requiring time-intensive Monte Carlo simulations calculated using a validated beam model. Consequently, although the correction-factor-based approach of Alfonso et al [25] is conceptually useful its practical implementation presents difficulties.

However it may be possible to reduce the scale of small-field correction factors, or eliminate them altogether, by modifying detector designs. Further to the work of Scott *et al* [16], this chapter shows that, under small field conditions, mass density is the principal determinant of detector water-equivalence. Detectors whose sensitive volume has relatively low density (*e.g.* the MicroLion and the PinPoint) can potentially be improved by adding high density media into the detector design. And conversely, the water-equivalence of solid-state detectors such as the Ediode and Diamond might be improved by adding low density filler media into the detector design. This possibility will be further explored in Chapter 6.

[2] This study utilised a 6 MV beam from a Varian linac, an SSD of 100 cm and a detector depth of 5 cm, whereas the study of Francescon *et al* [32] utilised 6 MV beams from Elekta/Siemens linacs, an SSD of 90 cm, and a detector depth of 10 cm.

Chapter 5

The Dose Area Product Metric

5.1 Introduction

Simulating $k_{Q_{clin},Q_{msr}}^{f_{clin},f_{msr}}$ values for a host of scenarios is a costly enterprise in terms of both researcher and processor hours. Chapter 4 also highlights the challenging nature of reporting absorbed dose at a single location under small-field conditions.

In 2004, Bouchard and Seuntjens demonstrated that a convolution/superposition approach could be used to calculate $k_{Q_{clin},Q_{msr}}^{f_{clin},f_{msr}}$ values [77]. This approach was also utilised by González-Castaño et al in 2012 [78], who showed that ion chamber point-read-outs and lateral profiles could be obtained by convolving spatial dose distributions with two-dimensional, ion chamber response functions. In this chapter, the convolution formulation of González-Castaño et al [78] is extended. The resulting Dose Area Product (DAP) theorem indicates that any dosimeter may be used to accurately measure a 2D spatial integral of small field dose to water, provided that (i) the dosimeter responds linearly with dose-rate (ii) a conventional large-field point calibration factor (which is detector specific) is applied to the dosimeter's integrated reading (iii) the wide field and small field photon spectra do not differ substantially.

The Dose Area Product (DAP) concept has already been advocated for small field dosimetry by Djouguela et al [79], who in 2006 proposed using large-area ionisation chambers (with sensitive cross-sectional area greater than that of the field under consideration) to obtain an integral dose result via a single measurement. Additionally, integral dose measures of another form - dose profiles obtained using scanned chambers - have been proposed as a possible alternative to conventional small beam output factors [16, 80, 81]. This work combines and extends these ideas to develop a DAP formalism for conventional small dosimeters. Here the DAP theorem is tested both experimentally and using Monte Carlo methods for a range of detectors.

5.2 Methods

5.2.1 Dose Area Product (DAP) / Dose Length Product (DLP) theorem

Consider scanning a detector through a series of positions along the x-axis in a large water tank, past a time-invariant pencil beam located at $x = 0$ (Figure 5.1) which delivers an integral dose-rate I per second, sharing the integral dose across all detector dwell positions.

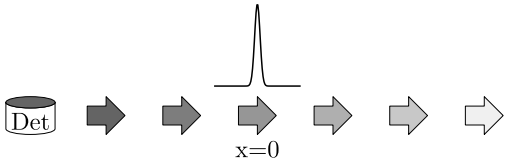

FIGURE 5.1: Fixed pencil beam, scanned detector

The same detector reading would be obtained by holding the detector fixed at $x = 0$ and scanning the time-invariant pencil beam along the $x-$axis (Figure 5.2) through these dwell positions at the same rate, again delivering the same integral dose-rate I.

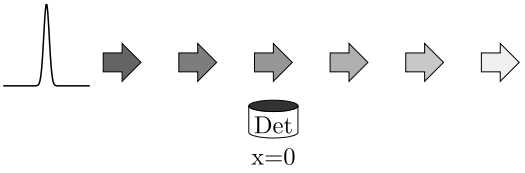

FIGURE 5.2: Fixed detector, scanned pencil beam

However, instead of irradiating the detector using all the beam positions one after the other, the beams can equivalently be applied all together, generating a long, thin field. Extending the argument into two dimensions it is clear that if we scan a detector over x and y across a pencil beam located at the origin, this can be equated to positioning the detector at the origin and exposing it to a wide field composed of identical pencil beams. Exactly the same integral dose would be deposited in the detector sensitive volume. And, provided that the detector's response was linear with dose, the resulting reading would still be exactly the same.

Now the detector could be either a real instrument or a point of water. And consequently the ratio of integrated dose absorbed by the detector sensitive volume to that absorbed by a point of water is the same whether the detector and point of water lie at the centre of a wide field, or are scanned in two dimensions across a pencil beam. Therefore provided that the detector responds linearly with dose-rate, the calibration factor for

a scanned pencil beam is the same as that at the centre of a $10\times10\,\mathrm{cm}^2$ field, and so the Dose Area Product (DAP) in water can be calculated from the detector integrated reading ('Meter-reading Area Product' - MAP) as

$$\mathrm{DAP}_{\mathrm{water}} = \mathrm{MAP}_{\mathrm{detector}} \times [\text{Calibration Factor}]_{\text{scanned pencil beam}} \tag{5.1}$$

$$= \mathrm{MAP}_{\mathrm{detector}} \times [\text{Calibration Factor}]_{10\times10\,\mathrm{cm}^2} \tag{5.2}$$

where

$$[\text{Calibration Factor}]_{10\times10\,\mathrm{cm}^2} = \left[\frac{\text{Dose to on-axis point of water}}{\text{Meter-reading from on-axis detector}}\right]_{10\times10\,\mathrm{cm}^2} \tag{5.3}$$

$$= \left[\frac{D_{\mathrm{w,Q}_{10\times10\,\mathrm{cm}^2}}^{f_{10\times10\,\mathrm{cm}^2}}}{M_{\mathrm{Q}_{10\times10\,\mathrm{cm}^2}}^{f_{10\times10\,\mathrm{cm}^2}}}\right] \tag{5.4}$$

Since any field can be considered to be composed of a set of individual pencil beams, it follows that DAPs of quite general fields can be obtained by multiplying integrated readings throughout the field ('Meter-reading Area Products' - MAPs) by the $10\times10\,\mathrm{cm}^2$ field calibration factor.

Here the theorem is tested both experimentally and using the Monte Carlo method. Experimentally it would be very time consuming to scan a detector across a grid of positions in both the x and y directions, so instead we choose to measure the simpler Dose Length Product (DLP), scanning the detector in a single direction across the short axis of a slit field. Monte Carlo simulations are used to study both DAP and DLP cases.

5.2.1.1 Assumptions made in deriving the theorem

1. The detector responds linearly with dose-rate
2. The scanned pencil beam is time-invariant
3. Profiles of measured fields extend sufficiently beyond the field edge that, at the profile limits, the detector response falls to zero

4. The calibration field varies little in intensity or energy spectrum over an area sufficiently wide[1] that the photon fluence outside it contributes negligibly to the dose absorbed by a detector located at the centre of the field

5.2.2 DLP experimental measurements

Direct experimental testing of the DAP theorem for small field dosimeters is possible, but very time consuming, the numerous detector positions requiring a large amount of beam-on time. In this study, in order to save measurement time the theorem was tested via the DLP: dose length products were measured across a slit field.

The linac jaws were set to $0.5\,\text{cm}\times40\,\text{cm}$ ($x \times y$) and were not re-positioned at any point during the DLP measurement (detector exchange and re-centering was performed for the fixed, initial jaw positions). Using the PTW MP3 water tank, dosimeters were scanned through symmetrical $x-$axis profiles, with an inter-measurement-spacing of 0.2 mm between off-axis distances of 0 and 20 mm. 1 mm inter-measurement spacing was used thereafter out to an off-axis distance of 50 mm. A fixed measurement time of 1 second was employed for all dosimeters / measurement positions. In all cases, the SSD was 100 cm and the dosimeter reference point was positioned at a depth of 5 cm. For each dosimeter, a single, large-field calibration factor was determined from the reading obtained with the detector positioned in the centre of a $10\times10\,\text{cm}^2$ field, irradiated with 100 MU; in this manner the dose measured by each detector corresponded to a fixed water dose (1 Gy in this case) as required by equation 5.4. The complete experiment was repeated twice (using the initial, fixed jaw positions).

5.2.3 Monte Carlo methods

5.2.3.1 DLP

The BEAMnrc linac model was used to generate a phase space file for a $0.5\times40\,\text{cm}^2$ ($x \times y$) slit field, collimated by the linac jaws. Within egs_chamber a lateral dose profile was calculated using a series of simulations in which the complete virtual detector was progressively moved from position to position across the short-axis of the field. In order

[1] The Monte Carlo based study of Sheikh-Bagheri and Rogers estimated that, at an SSD of 100 cm, direct photons (photons which do not interact between the linac target and the scoring plane) form around 95% of the total photon fluence for a $10\times10\,\text{cm}^2$ field produced by a 6 MV Varian Clinac [82]. Amongst the direct photons, the energy spectrum varies little with changing off-axis position (the average photon energy falling by ∼5% between off-axis distances of 0 and 20 cm) [82]. Additionally, even amongst the small fraction of indirect photons where the off-axis change in energy spectrum is larger (∼ 25% [82]), the overall impact on the photon mass energy absorption coefficient and electron mass collisional stopping power should be small (see data from http://www.nist.gov/pml/index.cfm).

to reduce the computational burden, half-profiles were simulated (profile symmetry was assumed). From the central axis out to an off-axis distance of 1 cm, an inter-positional spacing of 0.25 mm was employed. Thereafter, the inter-positional spacing was set to 2 mm, out to an off-axis distance of 3 cm.

Each simulated integral dose was multiplied by a large-field calibration factor unique for the detector utilised, equation 5.4. Within equation 5.4 the 'Meter-reading from on-axis detector' was calculated as the dose absorbed by the sensitive volume of the complete virtual detector, irradiated by a $10\times10\,cm^2$ field generated by the BEAMnrc linac model while the dose to water was calculated in the same manner but with the complete virtual detector model replaced by a water-equivalent version (equivalently, a single very small water voxel could have been used to simulate the dose to water for all detector calibrations, the effect of averaging over the dosimeter sensitive volume being insignificant for a $10\times10\,cm^2$ field).

A $0.25\times0.25\times5\,mm^3$ water voxel was also scanned through the set of detector profile positions, to obtain a reference water DLP (with a calibration factor of unity).

5.2.3.2 DAP

Monte Carlo testing of the DAP theorem was initially performed for a series of small, square fields. The BEAMnrc linac model was used to generate phase space files for $0.25\times0.25\,cm^2$, $0.5\times0.5\,cm^2$ and $1\times1\,cm^2$ fields, all collimated using the linac jaws. In order to reduce the required computation time, virtual detectors were translated over positions spanning a single quadrant of the field, two-way field symmetry being assumed. The series of detector positions employed for the $0.25\times0.25\,cm^2$ field DAP simulation are shown in Figure 5.3.

Similar sets of dosimeter positions (again spanning a single field quadrant) were used for the $0.5\times0.5\,cm^2$ and $1\times1\,cm^2$ field simulations. For each detector, the simulated doses were multiplied by the appropriate large-field calibration factor, as described above for the DLP simulations. In all DAP simulations in this study, simulated doses from detector positions in low resolution grid areas were scaled up (according to the area each measurement covered) in order to ensure uniform sampling across the whole radiation field.

A $0.25\times0.25\times5\,mm^3$ water voxel was also scanned through the set of detector positions shown in Figure 5.3, to obtain a reference water DAP (with a calibration factor of unity).

In order to test the DAP methodology for a more complex (irregular and modulated) clinical small field scenario, the BEAMnrc linac model was also used to generate a phase

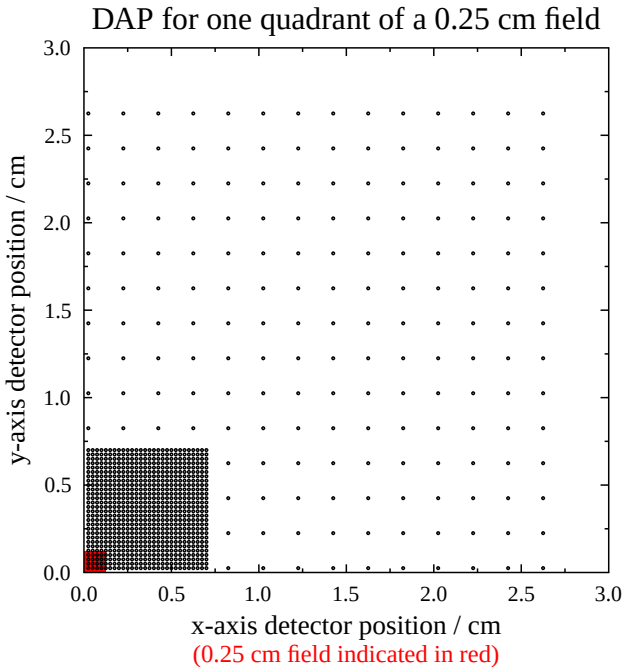

FIGURE 5.3: Complete set of detector grid positions used in Monte Carlo simulations of DAP for a single quadrant of a $0.25\times0.25\,\mathrm{cm}^2$ field. From the origin out to an off-axis distance of 7 mm, the inter-measurement spacing was 0.25 mm. Thereafter, out to an off-axis distance of 26 mm an inter-measurement spacing of 2 mm was used.

space file for a clinical IMRT breast field taken from the IMPORT (Intensity Modulated Partial Organ Radiotherapy) clinical trial [83]. In this case the $0.25\times0.25\times5\,\mathrm{mm}^3$ water voxel DAP was calculated along with the DAPs for two dosimeters, the dense Diamond detector and the air-filled PinPoint chamber.

5.3 Results and Discussion

5.3.1 Experimental DLP

Figure 5.4 shows static field experimental DLP results obtained for the PinPoint and Diamond detectors and for two different electron diodes - the unshielded PTW 60012 diode used throughout this study, and additionally an IBA Electron Field Detector (EFD^{3G} diode). The reading per monitor unit multiplied by the calibration factor (dose per reading) obtained in a $10\times10\,\mathrm{cm}^2$ field is plotted along the left-hand y-axis in Figure 5.4(a), while off-axis distance is plotted on the x-axis. The right hand axis of Figure 5.4(a) compares the areas (DLPs) under the complete calibrated profiles obtained using the diamond detector and two electron diode detectors to that obtained for the PinPoint.

As expected from the DLP constancy theorem of Section 5.2.1, the experimentally determined Diamond and PinPoint DLPs agree to within 0.5% (with 1 s.d. uncertainties of $< 0.3\%$). However, the DLP obtained using the PTW Ediode is 7% low relative to that obtained using the PinPoint (Figure 5.4(a), 1 s.d. uncertainty of 0.2%). Further investigation showed that the response of the PTW Ediode was non-linear with dose-rate, breaking a key assumption of the DLP/DAP constancy theorem. In particular, the Ediode under-responded at low dose-rates, erroneously reducing the area under the profile tails when calibrated according to measurements made at high dose rate in the centre of a $10\times10\,\mathrm{cm}^2$ field. A similar low dose-rate under-response was also observed by Lacroix *et al* [84] in 2011 for the same detector model, a PTW unshielded diode 60012.

To further test the experimental validity of the DLP theorem, a second IBA-manufactured electron diode (EFD^{3G}) was employed. For this detector the experimentally-determined DLP agreed with that of the PinPoint to within 0.5%, and the detector showed no signs of under-reading at low dose-rates thus fulfilling the linearity requirement of the DLP constancy theorem. Both the PTW diode 60012 and the IBA diode EFG-3G use p-type silicon. However, AAPM Report 87 [85] concludes that differences in dose-rate dependence emerge mainly due to a complex interplay between diode: substrate resistivity; defects and impurities; pre-irradiation requirements, and capture cross-sections[2].

Positional information on differences between calibrated dosimeter measurements is shown in Figure 5.4(b). The largest inter-detector variation in response occurs in the high dose-gradient regions.

Figure 5.4(c) explores the third assumption of the DLP/DAP theorem (Section 5.2.1) which requires the measured profile to extend sufficiently far beyond the edges of the small field that, at the profile limits, the detector response falls to zero. In practice, at the extremes of our measured profiles, each detector reading falls to less than 1.5% of its central axis value. The IBA Diode: PinPoint DLP ratio for the slit field agrees to within 0.9% (with a 1 s.d. uncertainty of 0.5%) for symmetrical profile limits of 20 mm, while for symmetrical profile limits of 50 mm, the ratio agrees to within 0.5% ($\pm$ 0.3% 1 s.d.). For these limits the Diamond:PinPoint DLP ratio agrees to within 1.11% ($\pm$0.2% 1 s.d.) and 0.3% ($\pm$0.1% 1 s.d.). Assumption (4) of the DLP/DAP theorem requires that the calibration field is sufficiently wide that the central axis detector response function falls to zero for the furthest pencil beams. Whilst this issue has not been explicitly explored in this study, it is of course closely related to assumption (3), and from the data presented here, the standard $10 \times 10\,\mathrm{cm}^2$ calibration field employed appears to be wide enough.

[2]The report suggests that there is no clear distinction between the dose-rate dependence of n-type and p-type diodes.

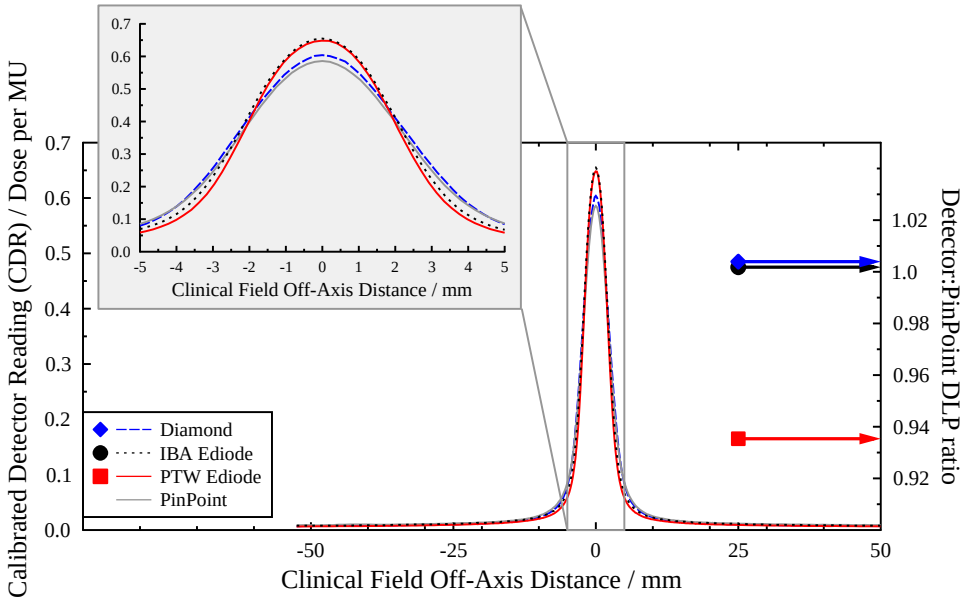

(a) Calibrated profiles obtained for four different detectors; the scale on the left-hand y-axis shows the Calibrated Detector Readings (CDRs), whilst that on the right hand side shows the ratio of detector DLP to PinPoint DLP where each DLP is taken as the area under the complete CDR curve.

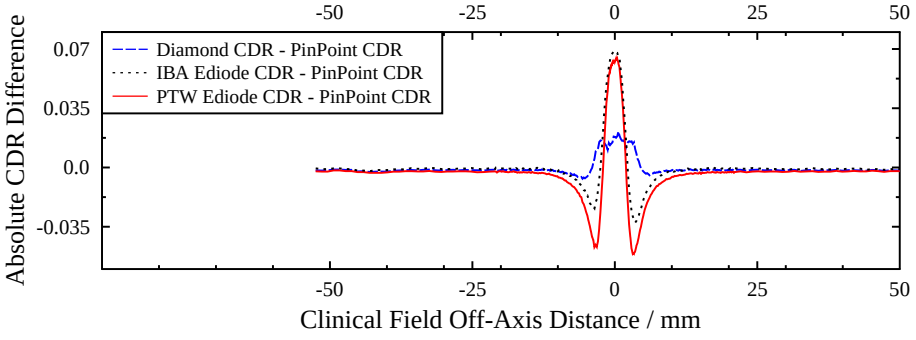

(b) Absolute differences between calibrated profiles measured by the PinPoint and other dosimeters.

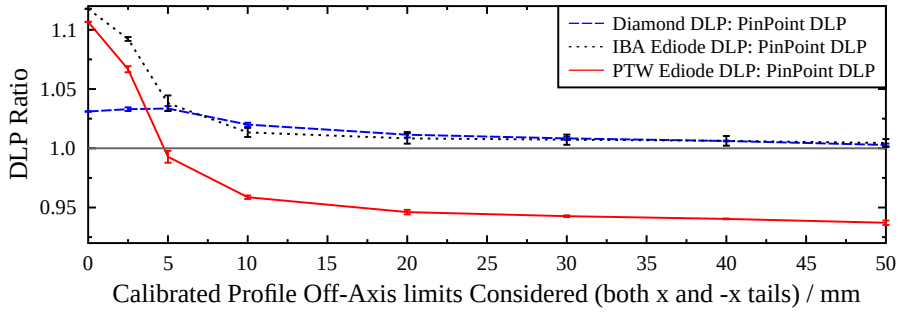

(c) Convergence of DLP ratio to unity with symmetrical off-axis profile limits considered. Error bars show 1 s.d. uncertainties.

FIGURE 5.4: Experimental DLP results obtained across the short (x-) axis of a 0.5 cm×40 cm linac slit field.

5.3.2 Monte Carlo calculated DLP

Simulated DLP results obtained for the four virtual PTW detectors, are shown in the left-hand column of Table 5.1, normalised to the results obtained for a reference detector composed of a $0.25\times0.25\times5\,mm^3$ water voxel alone. None of the DLP ratios lie further than 2.2 standard deviations (of the statistical uncertainty) from unity, including the PTW Ediode-to-water DLP ratio. Thus the Monte Carlo simulations validate the DLP theorem, implying that the violation of DLP constancy observed for the PTW Ediode is likely to be attributable to the non-linearity of detector signal with dose, as described for this dosimeter by Lacroix *et al* [84], an electronics consideration rather than an anomaly due to any radiological properties of the detector.

Detector	Detector:Water DLP ratio	% uncertainty (1 s.d.)
PTW PinPoint	0.9986	0.37
PTW Diamond	1.0022	0.31
PTW MicroLion	1.0080	0.37
PTW Ediode	1.0128	0.65

TABLE 5.1: Monte Carlo DLP results for $0.5\times40\,cm^2$ slit field.

5.3.3 Monte Carlo calculated DAP for square fields

Results of DAP simulations performed for a $0.25\times0.25\,cm^2$ field are shown in Figure 5.5. In particular the figure shows DAPs calculated for PinPoint and diamond detectors, divided by the DAP calculated for the reference water-based detector. The figure also shows how the DAP ratios change as the number of simulated detector positions is progressively increased from just a central location through to all locations shown in Figure 5.3. The figure shows how, for the single most central position, the difference in response between the PinPoint and the water voxel exceeds 20% and the difference in response between the Diamond detector and the water voxel response is ≈15%. However, as additional detector positions are considered, the DAPs for the two detectors tend towards agreement, ultimately both matching that obtained for the water voxels (the reference) to within the statistical uncertainties of the simulation. In fact, Figure 5.3 indicates that assumption (3) of the DLP/DAP theorem (Section 5.2.1) appears to be fulfilled for an off-axis scan distance of 7 mm (the end of the high resolution grid region in Figure 5.5).

For a $0.5\times0.5\,cm^2$ field, complete DAP simulations have been performed for the diamond, Ediode, MicroLion and PinPoint detectors and results are summarised in Table 5.2.

Excellent agreement with DAPs calculated for an ideal water dosimeter was obtained for all four dosimeters.

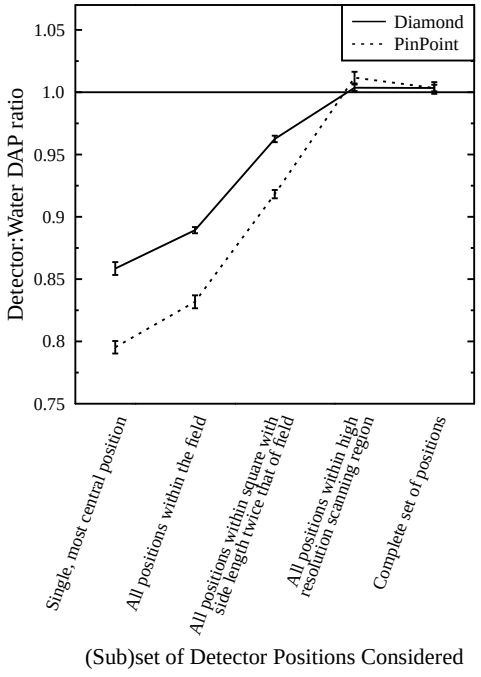

FIGURE 5.5: Monte Carlo Simulated DAP results (normalised to DAP calculated for an ideal small water voxel detector) calculated various subsets of detector positions within one quadrant of a $0.25\times0.25\,\mathrm{cm}^2$ field. Error bars show 1 s.d. statistical uncertainties.

	$0.5\times0.5\,\mathrm{cm}^2$ cm Field DAP	
Detector	Detector:Water DAP ratio	% uncertainty (1 s.d.)
PinPoint	0.9972	0.33
Diamond	0.9990	0.26
MicroLion	1.0063	0.32
Ediode	0.9961	0.61

TABLE 5.2: Monte Carlo calculated DAP results for $0.5\times0.5\,\mathrm{cm}^2$ field

5.3.4 Monte Carlo calculated DAP for an IMRT field

The fluence map of the simulated four segment (partial breast irradiation) IMRT field is shown in Figure 5.6, overlaid on the full grid of detector positions used in the Monte Carlo DAP simulation. Also shown are simulations of calibrated Diamond and PinPoint dose measurements, and calculations of doses absorbed by water voxels lying on the same positional grid, each voxel having dimensions $0.25 \times 0.25 \times 5\,\mathrm{mm}^3$. Additionally, Figure 5.6 includes a plot displaying differences between doses measured using the diamond and PinPoint detectors expressed as a percentage of the diamond calibrated dose value at point [0,0] within the field[3]. Identical positional contours are superimposed on the water voxel dose plot and on the dose difference plot to highlight the areas of the radiation field which elicit the greatest difference in dosimeter response in particular the high dose region in the centre of the field. The difference plot shows that the fluence modulation pattern leads to response differences of 5-6% (of the calibrated Diamond dose at the centre of the field) across large regions of the IMRT field. However, once the integral dose is considered the responses of the Diamond and the PinPoint detectors agree with that of the ideal water detector to within 0.4%, falling within the 2 s.d. statistical uncertainty level on the calculations (Table 5.3).

	IMRT Field DAP	
Detector	Detector:Water DAP ratio	% uncertainty (1 s.d.)
PinPoint	0.9990	0.35
Diamond	0.9967	0.26

TABLE 5.3: Monte Carlo DAP results for IMRT field

5.4 Conclusions

It has been suggested by Djouguela et al [79] and Sánchez-Doblado et al [86] that the area dose integral in a plane perpendicular to the beam axis, measured using an ionisation chamber whose area is larger than the field provides a useful dose metric for small fields. Here, it is demonstrated that the surface integral concept is also useful for conventional (small) dosimeters. Although inter-detector measurement variations of many percent are demonstrable at individual positions within small fields, the results of our study

[3]Point [0,0] lies just beyond the high dose-gradient part of the field, in a region that is relatively uniform. Considering five additional nearby points chosen at random ([0.3,-1.2], [0.3,0.3], [-0.75,0.45], [0,0.75] and [-0.9,0.75]) the mean value for the diamond dose agreed with that of the central point to within 0.38%, with a standard deviation of 0.36%. Thus the point-dose-difference analysis was found to be relatively robust to calibration point choice (within the high-dose region).

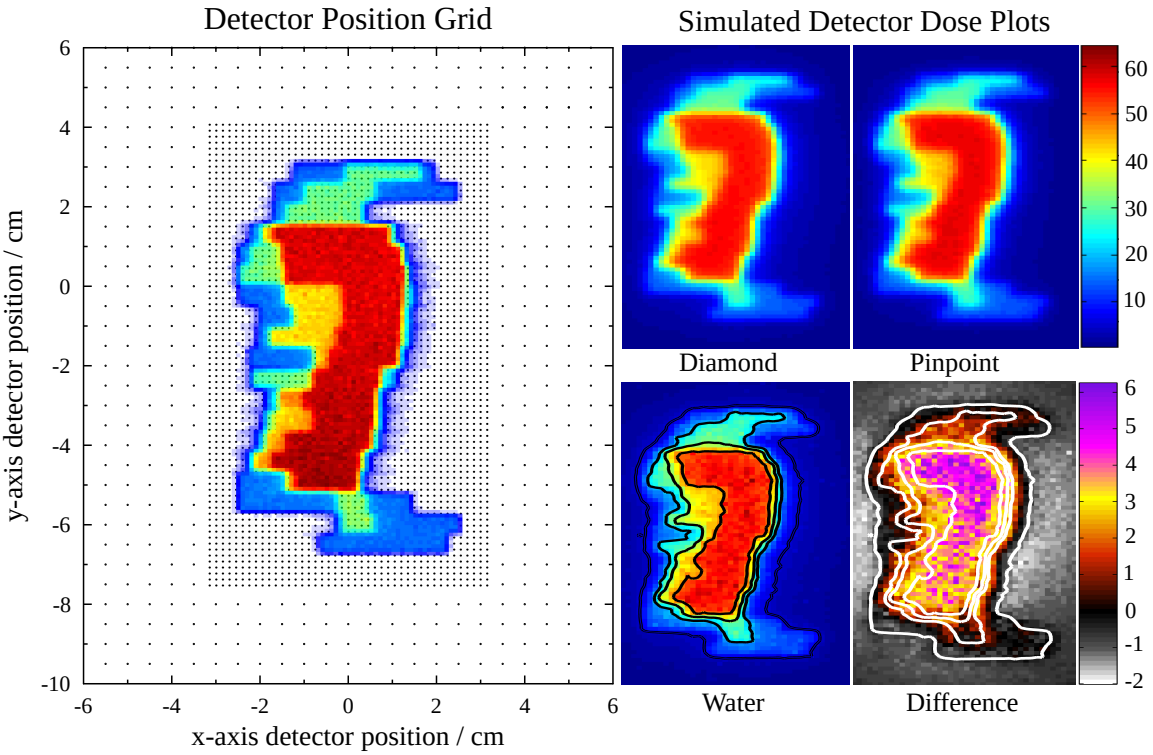

FIGURE 5.6: Monte Carlo DAP simulations for an IMRT field. Far left: complete set of detector positions used to calculate the DAP of the field, overlaid with the in-air fluence. Right: calibrated detector dose maps for the Diamond detector and PinPoint chamber, plus dose map for the small water voxel. A 64 element colour map is used, limited by the same minimum and maximum calibrated dose values for all dosimeters/water voxels. Far right, lower plot: (Diamond calibrated dose − Pinpoint calibrated dose) expressed as a percentage of the Diamond calibrated dose value at the centre of the field (point [0,0]).

indicate that the application of conventional (detector-specific) large-field calibration factors leads to accurate measurement of the dose area product (integral dose).

Under the Alfonso formalism, point-dose to water in a small ('*clin*') field is obtained using equation 7.1:

$$D^{f_{\text{clin}}}_{\text{w,Q}_{\text{clin}}} = M^{f_{\text{clin}}}_{\text{Q}_{\text{clin}}} \cdot \left[\frac{D^{f_{\text{msr}}}_{\text{w,Q}_{\text{msr}}}}{M^{f_{\text{msr}}}_{\text{Q}_{\text{msr}}}} \right] \cdot \left\{ \frac{D^{f_{\text{clin}}}_{\text{w,Q}_{\text{clin}}} / M^{f_{\text{clin}}}_{\text{Q}_{\text{clin}}}}{D^{f_{\text{msr}}}_{\text{w,Q}_{\text{msr}}} / M^{f_{\text{msr}}}_{\text{Q}_{\text{msr}}}} \right\} \quad (5.5)$$

where the term in braces is the small-field point-dose correction factor, $k^{f_{\text{clin}},f_{\text{msr}}}_{\text{Q}_{\text{clin}},\text{Q}_{\text{msr}}}$. Should a small, linearly-responding dosimeter be used to integrate dose over a high resolution grid of positions inside and outside the boundaries of a radiation field, such that integral-dose is considered rather than the point-dose, equation 7.1 can be vastly simplified to:

$$DAP^{f_{\text{clin}}}_{\text{w,Q}_{\text{clin}}} = MAP^{f_{\text{clin}}}_{\text{Q}_{\text{clin}}} \cdot \left[\frac{D^{f_{\text{msr}}}_{\text{w,Q}_{\text{msr}}}}{M^{f_{\text{msr}}}_{\text{Q}_{\text{msr}}}} \right] \quad (5.6)$$

where: $MAP^{f_{\text{clin}}}_{\text{Q}_{\text{clin}}}$ is an un-calibrated detector integral-dose reading; $\left[\frac{D^{f_{\text{msr}}}_{\text{w,Q}_{\text{msr}}}}{M^{f_{\text{msr}}}_{\text{Q}_{\text{msr}}}} \right]$ is the classical wide field (detector-specific) calibration factor, and no other correction factors need be applied.

Consequently it follows that if a single dosimeter is used for all treatment planning system (TPS) commissioning measurements (including off-axis profiles and output factors) the integral dose calculated by the TPS should be robust, regardless of the detector type - provided that the detector responds linearly with dose-rate and the response of the detector is relatively energy independent[4].

In summary, this chapter demonstrates empirically that DAPs can be measured accurately for small fields using detectors calibrated in wide fields, despite the fact that dose measurement at individual points requires corrections specific to the field size and detector design, position and orientation. With regards to the total uncertainty associated with the DAP metric:

- the DAP calibration will be subject to the same uncertainties as any conventional point dose measurement
- additional uncertainties will arise due to discrepancies between the ideal conditions utilised in deriving the theorem and the physical reality of the linac beam and detectors involved

A more rigorous analysis of the validity of theorem assumptions would clearly be needed to further investigate the latter form of uncertainty.

[4]Should the detector's response to changing beam spectrum (*e.g.* with depth) vary substantially then a depth-specific calibration factor might be needed; *i.e.* it might be necessary to calibrate the detector in a $10\times10\,\text{cm}^2$ field at various depths to correctly calculate the DAP at each one.

For those interested, a mathematical formulation of both continuous and discrete forms of DAP is included in appendix A. For the discrete version, a further logical and interesting extension of this work would be to consider:

1. the maximum inter-detector spacing, and
2. the mininum number of measurement positions (the minimum extent of measurement area)

required for DAP constancy to be upheld. For a given detector, if the minimum inter-detector spacing for DAP constancy is greater than that required to prevent interference between neighbouring instruments, then it should be a straightforward process to construct a DAP-compatible detector-array for 2D IMRT quality control. Using such an array, both accurate dosimetric information and spatial verification could be obtained via a single measurement.

Chapter 6

Modifying detector designs for small field dosimetry

6.1 Introduction

As of Spring 2013, the only internationally accepted formalism for accounting for dosimetric perturbations under small-field conditions is the point-dose correction-factor method of Alfonso *et al* (investigated in Chapter 4). Under the Alfonso protocol, a ratio of dosimeter readings obtained across small and large fields ($M^{f_{\text{clin}}}_{\text{Q}_{\text{clin}}}/M^{f_{\text{msr}}}_{\text{Q}_{\text{msr}}}$) is converted into a ratio of "point-like" water structure doses ($D_{\text{clin}}/D_{\text{msr}}$) using the correction factor $k^{f_{\text{clin}},f_{\text{msr}}}_{\text{Q}_{\text{clin}},\text{Q}_{\text{msr}}}$:

$$\frac{D_{\text{clin}}}{D_{\text{msr}}} = k^{f_{\text{clin}},f_{\text{msr}}}_{\text{Q}_{\text{clin}},\text{Q}_{\text{msr}}} \cdot \frac{M^{f_{\text{clin}}}_{\text{Q}_{\text{clin}}}}{M^{f_{\text{msr}}}_{\text{Q}_{\text{msr}}}} \tag{6.1}$$

As discussed in Chapter 4, for commonly used radiotherapy detectors, $k^{f_{\text{clin}},f_{\text{msr}}}_{\text{Q}_{\text{clin}},\text{Q}_{\text{msr}}}$ is strongly dependent upon detector off-axis position and detector azimuthal angle in addition to field size [15, 29–32].

Following on from the work of Scott *et al.* [16], results from Chapter 4 also demonstrate that, when considered in isolation, dosimeter sensitive media with mass-densities $>1\,\text{g/cm}^3$ over-respond relative to water, whereas sensitive media with densities $<1\,\text{g/cm}^3$ under-respond.

Further to [87], this chapter explores whether detector designs may be modified (based upon the principle of "mass-density compensation") to produce a dosimeter with a $k^{f_{\text{clin}},f_{\text{msr}}}_{\text{Q}_{\text{clin}},\text{Q}_{\text{msr}}}$ value of unity under a broad range of small-field conditions. For such a

dosimeter the ratio of detector readings in small and large fields would equal the ratio of water readings in small and large fields: ideal performance would be achieved.

6.2 General Monte Carlo Methods

This work utilised phase space files from the 6 MV BEAMnrc linac model (described in Chapter 3) as radiation sources within the egs_chamber and flurznrc Monte Calo codes. A large virtual water phantom was simulated, located at an SSD of 100 cm. Unless otherwise stated, detector models were positioned at a depth of 5 cm. A machine-specific-reference field size of 3 cm was utilised (sufficiently large to be free from small field effects, but sufficiently small to enable relatively fast simulation times). Initial simulations were typically run using a square field of side-length 0.5 cm as the small ('clinical') field. For $k^{f_{\text{clin}},f_{\text{msr}}}_{\text{Q}_{\text{clin}},\text{Q}_{\text{msr}}}$ values calculated in this chapter, the "point-like" water structure considered was a $0.25\times0.25\times0.25\,\text{mm}^3$ water voxel[1]. A global electron cut-off (ECUT) of 0.512 MeV was employed.

For clarity, the additional methods used in this chapter are introduced alongside the relevant sections of the results and discussion. For all plotted data, 1 s.d. uncertainties are included as error bars.

6.3 Results and discussion

6.3.1 Modifying hypothetical spherical cavities

6.3.1.1 Cavity mass density versus cavity radius

Initially, hypothetical detectors of the simplest form were modelled: spherical cavities of radius 0.1 cm (comparable in size to many of the small-field detectors considered in this thesis, see Chapter 2). These were used to explore the relationship between the mass-density of the cavity and $k^{f_{\text{clin}},f_{\text{msr}}}_{\text{Q}_{\text{clin}},\text{Q}_{\text{msr}}}$. In order to eliminate effects due to cavity atomic composition, water of modified mass-density was considered[2]. $k^{f_{0.5},f_3}_{\text{Q}_{0.5},\text{Q}_3}$ was calculated for nine water-filled cavities identical in geometry, but whose mass-densities varied from $0.001\,\text{g/cm}^3$ to $20\,\text{g/cm}^3$. The results are shown in Figure 6.1(a). For a water-filled cavity, increasing the cavity density from 0.001 to $20\,\text{g/cm}^3$ reduces the on-axis $k^{f_{0.5},f_3}_{\text{Q}_{0.5},\text{Q}_3}$

[1] For water voxels of this size, volume averaging effects were found to be insignificant for fields with side lengths of 0.5 cm or greater - that is $k^{f_{\text{clin}},f_{\text{msr}}}_{\text{Q}_{\text{clin}},\text{Q}_{\text{msr}}}$ remained constant for a $0.5\times0.5\,\text{cm}^2$ clinical field when test simulations using smaller point-like structures were carried out

[2] The mass radiological properties of unit-density liquid water were maintained *as per* the method of Scott *et al. i.e.* the polarisation-effect-correction was not recalculated with changing mass-density.

by ∼30%. At least 15% of this reduction occurs over the range of mass-densities found in existing detectors (between the mass-densities of air and diamond, 0.0013 g/cm^3 - 3.52 g/cm^3).

Next, the impact of cavity radius upon $k_{Q_{clin},Q_{msr}}^{f_{clin},f_{msr}}$ was explored (the effect of volume averaging). Here $k_{Q_{0.5},Q_3}^{f_{0.5},f_3}$ was calculated for six spheres filled with unit-density liquid water, their radii ranging from 0.05 cm to 0.3 cm. The results are plotted in Figure 6.1(b). Increasing the radius from 0.05 cm to 0.3 cm results in a 30% increase in $k_{Q_{0.5},Q_3}^{f_{0.5},f_3}$.

Together Figures 6.1(a) and (b) indicate that whilst increasing the mass-density of a cavity lowers $k_{Q_{clin},Q_{msr}}^{f_{clin},f_{msr}}$, increasing the radius of that cavity will increase $k_{Q_{clin},Q_{msr}}^{f_{clin},f_{msr}}$: two competing effects are at play.

Remembering that:

$$k_{Q_{clin},Q_{msr}}^{f_{clin},f_{msr}} = \left[\frac{D_{w,Q_{clin}}^{f_{clin}}/M_{Q_{clin}}^{f_{clin}}}{D_{w,Q_{msr}}^{f_{msr}}/M_{Q_{msr}}^{f_{msr}}}\right] \tag{6.2}$$

it is important to note that trends in $k_{Q_{clin},Q_{msr}}^{f_{clin},f_{msr}}$ are almost entirely attributable to the (small-field) numerator of equation 6.2 (as shown in Figure 6.1). In the set-up used for Figure 6.1, $D_{w,Q_{clin}}^{f_{clin}}$ (the dose to a point-like structure of water) is constant, so the critical term is $M_{Q_{clin}}^{f_{clin}}$ which is influenced by both cavity size (volume averaging) and mass-density.

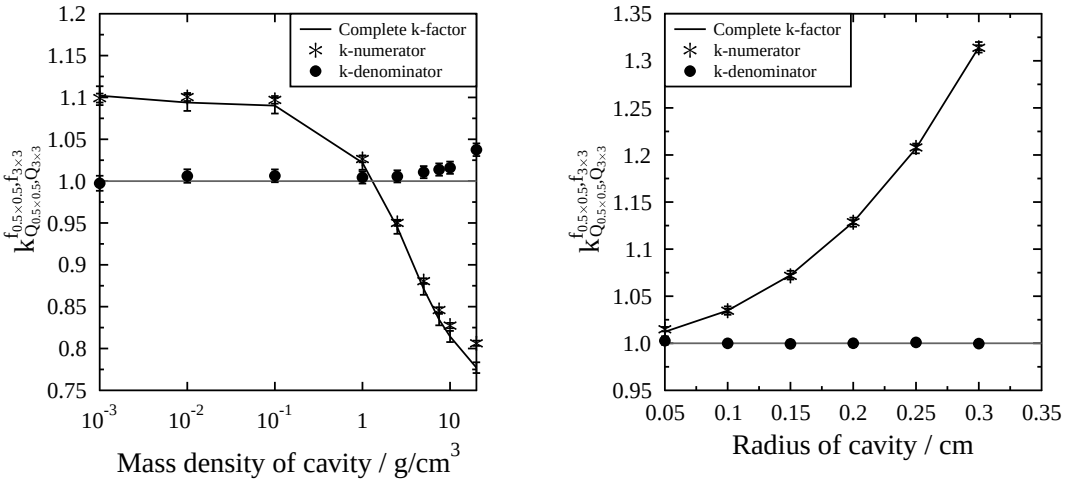

(a) Dependence of $k_{Q_{0.5},Q_3}^{f_{0.5},f_3}$ on cavity mass-density (for modified water of various densities and a fixed cavity radius of 0.1 cm)

(b) Dependence of $k_{Q_{0.5},Q_3}^{f_{0.5},f_3}$ on cavity radius (for cavities filled with unit-density water)

FIGURE 6.1: Impact of mass-density and radius on $k_{Q_{clin},Q_{msr}}^{f_{clin},f_{msr}}$ for hypothetical spherical cavities.

6.3.1.2 Mass-density compensation

In order to explore the possibility of detector design-modification based upon mass-density compensation, simulations were performed for spherical cavities (of radius 0.1 cm) made from diamond and air. These materials were chosen as they are the sensitive media of two real detectors. The low density air cavity was modified by the addition of a relatively high density graphite shell (graphite, a common detector electrode material), while the high density diamond cavity was modified using a low density air shell.

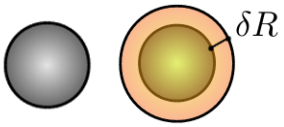

FIGURE 6.2: Initial tests of the principle of mass-density compensation: (a) a spherical sensitive volume (b) the same sensitive volume modified with a spherical shell (of thickness δR) made from a material of contrasting mass density.

Medium	Mass-density (g/cm^3)
Air	0.0013
Graphite	1.85
Diamond	3.52

TABLE 6.1: Mass-densities of media involved

Recall from Chapter 4, that $[k(D_{\text{vol}})]^{f_{\text{clin}},f_{\text{msr}}}_{\text{Q}_{\text{clin}},\text{Q}_{\text{msr}}}$ is defined as:

$$[k(D_{\text{vol}})]^{f_{\text{clin}},f_{\text{msr}}}_{\text{Q}_{\text{clin}},\text{Q}_{\text{msr}}} = \left[\frac{(D_{\text{vol}})^{f_{\text{clin}}}_{\text{w,Q}_{\text{clin}}}/M^{f_{\text{clin}}}_{\text{Q}_{\text{clin}}}}{(D_{\text{vol}})^{f_{\text{msr}}}_{\text{w,Q}_{\text{msr}}}/M^{f_{\text{msr}}}_{\text{Q}_{\text{msr}}}}\right] \tag{6.3}$$

and considers the dose D_{vol} absorbed by a volume of water having the same dimensions as the dosimeter sensitive region whereas the original $k^{f_{\text{clin}},f_{\text{msr}}}_{\text{Q}_{\text{clin}},\text{Q}_{\text{msr}}}$ considers the dose D absorbed by a point-like water structure. Consequently, $[k(D_{\text{vol}})]^{f_{\text{clin}},f_{\text{msr}}}_{\text{Q}_{\text{clin}},\text{Q}_{\text{msr}}}$ enforces consistent volume averaging for the water structure and detector sensitive region.

For each hypothetical detector, a range of shell thicknesses (δR values) were tested in order to find:

1. the value of δR which gave $k^{f_{0.5},f_3}_{\text{Q}_{0.5},\text{Q}_3}$=1
2. the value of δR which gave $[k(D_{\text{vol}})]^{f_{0.5},f_3}_{\text{Q}_{0.5},\text{Q}_3}$=1

for the standard set-up of a cavity positioned on-axis at a depth of 5 cm (within a 0.5×0.5 cm^2 field).

Figure 6.3 shows the variation in $k^{f_{clin},f_{msr}}_{Q_{clin},Q_{msr}}$ and also $[k(D_{vol})]^{f_{clin},f_{msr}}_{Q_{clin},Q_{msr}}$ with thickness δR of additional density-compensation shell. For both core media, the trends in behaviour and the optimised δR values (Table 6.2) are similar for $[k(D_{vol})]^{f_{clin},f_{msr}}_{Q_{clin},Q_{msr}}$ and $k^{f_{clin},f_{msr}}_{Q_{clin},Q_{msr}}$. In order to modify a detector of density <1 (so that its small field correction factors approach unity), a thicker shell is required when considering $k^{f_{clin},f_{msr}}_{Q_{clin},Q_{msr}}$ than when considering $[k(D_{vol})]^{f_{clin},f_{msr}}_{Q_{clin},Q_{msr}}$. This is because for densities <1, $k^{f_{clin},f_{msr}}_{Q_{clin},Q_{msr}}$ is pushed upwards by both mass-density and volume averaging effects. For modification of media with greater than unit density, a thicker shell is required in the case of $[k(D_{vol})]^{f_{clin},f_{msr}}_{Q_{clin},Q_{msr}}$. This is because for densities >1, $[k(D_{vol})]^{f_{clin},f_{msr}}_{Q_{clin},Q_{msr}}$ is pushed down by the density, but this effect is counter-balanced somewhat by volume averaging (less mass-density compensation is required for $[k(D_{vol})]^{f_{clin},f_{msr}}_{Q_{clin},Q_{msr}}$). The thickness of the proposed shells ranges from 70-130% of the radius of the sensitive cavity.

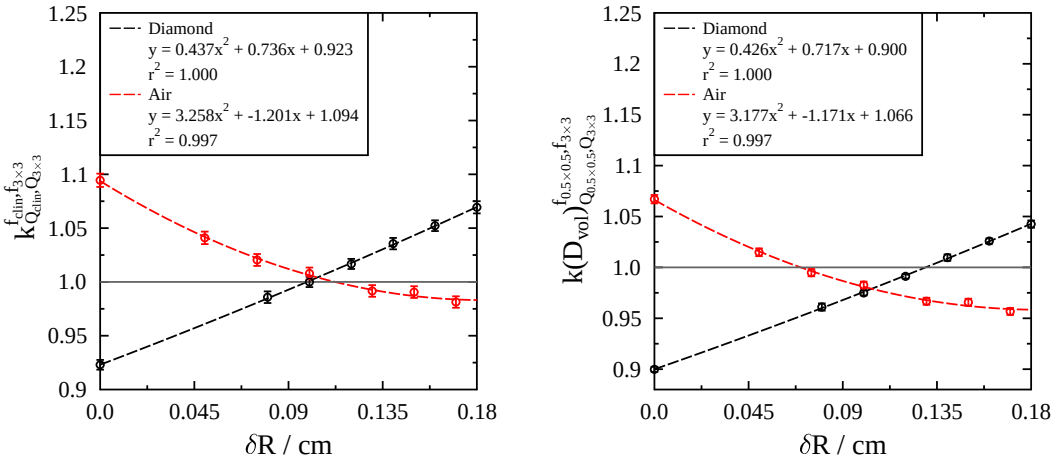

(a) $k^{f_{clin},f_{msr}}_{Q_{clin},Q_{msr}}$ (b) $[k(D_{vol})]^{f_{clin},f_{msr}}_{Q_{clin},Q_{msr}}$

FIGURE 6.3: Modifying hypothetical spherical detectors of 0.1 cm radius: exploring the thickness of shell (δR) required to attain unity in (a) $[k(D_{vol})]^{f_{clin},f_{msr}}_{Q_{clin},Q_{msr}}$ and (b) $k^{f_{clin},f_{msr}}_{Q_{clin},Q_{msr}}$. Quadratic fits (obtained using linear regression) are also shown.

	δR for $k^{f_{clin},f_{msr}}_{Q_{clin},Q_{msr}}$ (cm)	δR for $[k(D_{vol})]^{f_{clin},f_{msr}}_{Q_{clin},Q_{msr}}$ (cm)
Air modified using graphite	0.1128	0.0694
Diamond modified using air	0.0988	0.1295

TABLE 6.2: 0.1 cm radius sphere modifications based on polynomials fitted to 0.5 cm field data

In order to consider their robustness, the modifications of Table 6.2 were applied and tested for four different clinical field sizes and three different detector depths, with results shown in Figures 6.4 and Figures 6.5.

From Figure 6.4 we see that, in the case of the spherical air-filled cavity, the modification that was optimised for a 0.5 cm field also reduces the $k^{f_{\text{clin}},f_{\text{msr}}}_{Q_{\text{clin}},Q_{\text{msr}}}$ correction-factor associated with both smaller and larger fields. However, for the 0.25 cm field, $k^{f_{\text{clin}},f_{\text{msr}}}_{Q_{\text{clin}},Q_{\text{msr}}}$ is ∼5% too high compared to the ideal. A thicker graphite shell would have been proposed had the optimisation been performed for this field size. Nonetheless, for all field sizes, the addition of the graphite shell reduces the $k^{f_{\text{clin}},f_{\text{msr}}}_{Q_{\text{clin}},Q_{\text{msr}}}$ of the air cavity to approximately that of a water-filled cavity of the same size.

If we consider the basic diamond sphere, here our modification proves very successful. From Figure 6.4(a) across all field sizes, the deviation of $k^{f_{\text{clin}},f_{\text{msr}}}_{Q_{\text{clin}},Q_{\text{msr}}}$ from unity is <0.7% (around the level of the statistical uncertainties of the simulations).

Two aspects of the data presented in Figure 6.4 are particularly interesting:

1. The $k^{f_{\text{clin}},f_{\text{msr}}}_{Q_{\text{clin}},Q_{\text{msr}}}$ modifications prove more robust to changes in field size in the case of a diamond sphere modified using an air-shell, than in the case of an air sphere modified using a graphite-shell
2. For the diamond sphere, it appears to be easier to attain $k^{f_{\text{clin}},f_{\text{msr}}}_{Q_{\text{clin}},Q_{\text{msr}}}$=1 than $[k(D_{\text{vol}})]^{f_{\text{clin}},f_{\text{msr}}}_{Q_{\text{clin}},Q_{\text{msr}}}$=1 across a range of field sizes.

The first of these behaviours might be attributed to the fact that the electron fluence in the air-shell will enter the diamond cavity in a relatively unattenuated state, whereas within the graphite cavity, many more interactions will occur, reducing the impact of the shell upon the cavity fluence. Additionally, the $k^{f_{\text{clin}},f_{\text{msr}}}_{Q_{\text{clin}},Q_{\text{msr}}}$ values of the original diamond sphere are smaller than those of the original air sphere: the required correction is less extreme in the diamond case. Regarding the second effect, the core diamond sphere plus the $[k(D_{\text{vol}})]^{f_{\text{clin}},f_{\text{msr}}}_{Q_{\text{clin}},Q_{\text{msr}}}$ modified shell has a total radius of 0.2296 cm: the modified detector extends significantly beyond the boundaries of the $0.25\times0.25\,\text{cm}^2$ field. This is problematic in the case of $[k(D_{\text{vol}})]^{f_{\text{clin}},f_{\text{msr}}}_{Q_{\text{clin}},Q_{\text{msr}}}$: not enough of the compensatory air-shell (δR=0.1295 cm) lies within the boundaries of the field[3]. In the case of $k^{f_{\text{clin}},f_{\text{msr}}}_{Q_{\text{clin}},Q_{\text{msr}}}$, the required shell is much thinner (δR=0.0988 cm): the modification performs much better for the smallest field size.

[3]It may be possible to address this problem by changing the modification design: shifting some of the compensatory material from the sides of the spherical cavity to the region upstream.

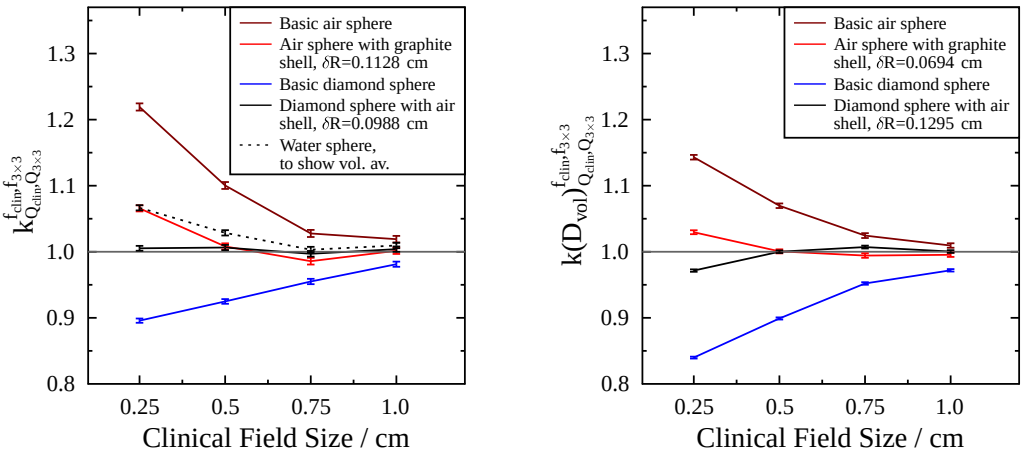

(a) $k^{f_{\text{clin}},f_{\text{msr}}}_{\text{Q}_{\text{clin}},\text{Q}_{\text{msr}}}$ (b) $[k(D_{\text{vol}})]^{f_{\text{clin}},f_{\text{msr}}}_{\text{Q}_{\text{clin}},\text{Q}_{\text{msr}}}$

FIGURE 6.4: Robustness of modifications to 0.1 cm radius spheres (δR values detailed in Table 6.2) to changing clinical field size

In addition to changing field size, Figure 6.5 considers the robustness of cavity modification to changing cavity depth[4]. Despite their location within the build-up region of the PDD, the cavities positioned at a depth of 1 cm exhibit very similar $k^{f_{\text{clin}},f_{\text{msr}}}_{\text{Q}_{\text{clin}},\text{Q}_{\text{msr}}}$ values to those positioned at the reference depth of 5 cm. As the depth of the cavity is increased to 25 cm, $k^{f_{\text{clin}},f_{\text{msr}}}_{\text{Q}_{\text{clin}},\text{Q}_{\text{msr}}}$ does vary significantly, however in all cases its value moves closer to the ideal. At first glance, this behaviour might be assumed to be due to beam divergence. However, if we consider the data for the basic air sphere, we would expect the nominal (isocentric) field size to increase by a factor of 1.2 between depths of 5 and 25 cm. But if we interpolate to larger field sizes on the depth=5 cm line (say from an x-axis value of 0.25 to 0.3) we see that the reduction in $k^{f_{\text{clin}},f_{\text{msr}}}_{\text{Q}_{\text{clin}},\text{Q}_{\text{msr}}}$ due to beam divergence alone appears insufficient to account for the low values of the data obtained at a depth of 25 cm. Thus, it is more likely that the discrepancy can be attributed to increased photon scatter at deeper depths, which blurs the beam profile and this also essentially serves to widen the effective field size.

Figure 6.6 demonstrates that, out to a distance of 0.3 cm (beyond the edge of the 0.5×0.5 cm field which extends to 0.2625 cm) the modifications to the spherical cavities also prove robust to changing off-axis position[5].

[4]For data simulated using the 3 cm machine-specific-reference field, the reference depth of 5 cm was maintained.

[5]Similarly, for data simulated using the 3 cm machine-specific-reference field, the reference (on-axis) detector position was maintained.

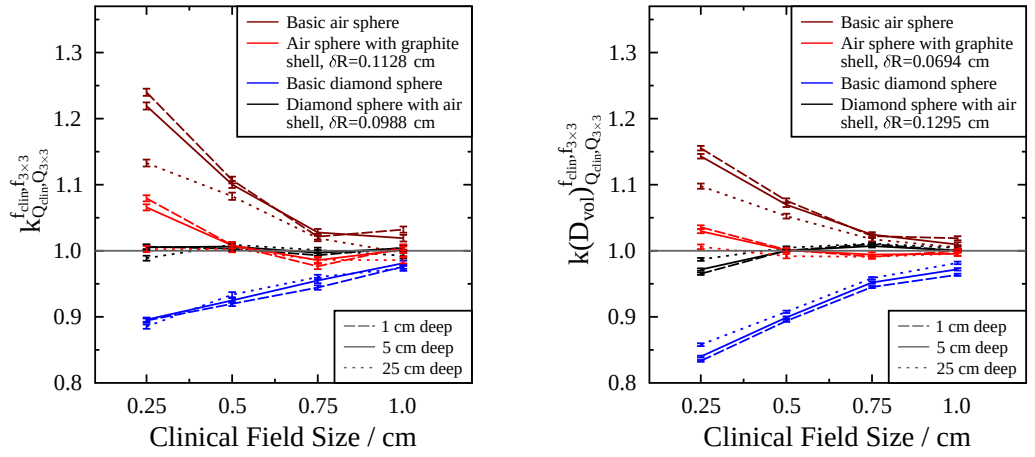

(a) $k^{f_{\text{clin}},f_{\text{msr}}}_{Q_{\text{clin}},Q_{\text{msr}}}$ (b) $[k(D_{\text{vol}})]^{f_{\text{clin}},f_{\text{msr}}}_{Q_{\text{clin}},Q_{\text{msr}}}$

FIGURE 6.5: Robustness of modifications to 0.1 cm radius spheres (δR values detailed in Table 6.2) to changing detector depth

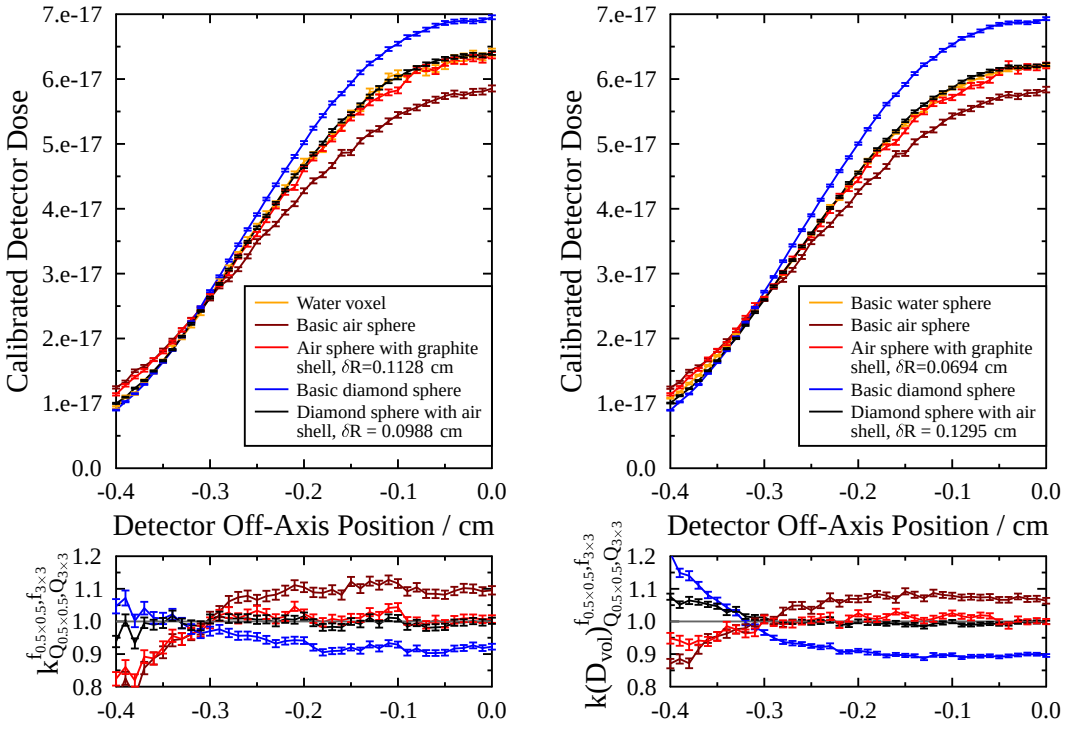

(a) $k^{f_{\text{clin}},f_{\text{msr}}}_{Q_{\text{clin}},Q_{\text{msr}}}$ (b) $[k(D_{\text{vol}})]^{f_{\text{clin}},f_{\text{msr}}}_{Q_{\text{clin}},Q_{\text{msr}}}$

FIGURE 6.6: Robustness of 0.1 cm radius sphere modifications (δR values detailed in Table 6.2) to off-axis position within a square clinical field of side length 0.5 cm.

For the optimised modifications, shells of varying half-angle (as shown in Figure 6.7) were also tested, to determine the relative impact of density-compensation-media up-stream/down-stream from the cavity itself.

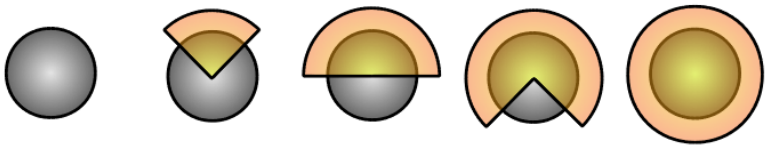

(a) $\theta = 0°$ (b) $\theta = 45°$ (c) $\theta = 90°$ (d) $\theta = 135°$ (e) $\theta = 180°$

FIGURE 6.7: Considering modifications using spherical shells of different half-angle (θ).

The largest gains in $k^{f_{\text{clin}},f_{\text{msr}}}_{\text{Q}_{\text{clin}},\text{Q}_{\text{msr}}}$ optimisation are obtained by adding media in the hemi-sphere directly above the cavity, little being lost by removing material below the cavity. This is as expected because the electron distribution is strongly forward-peaked.

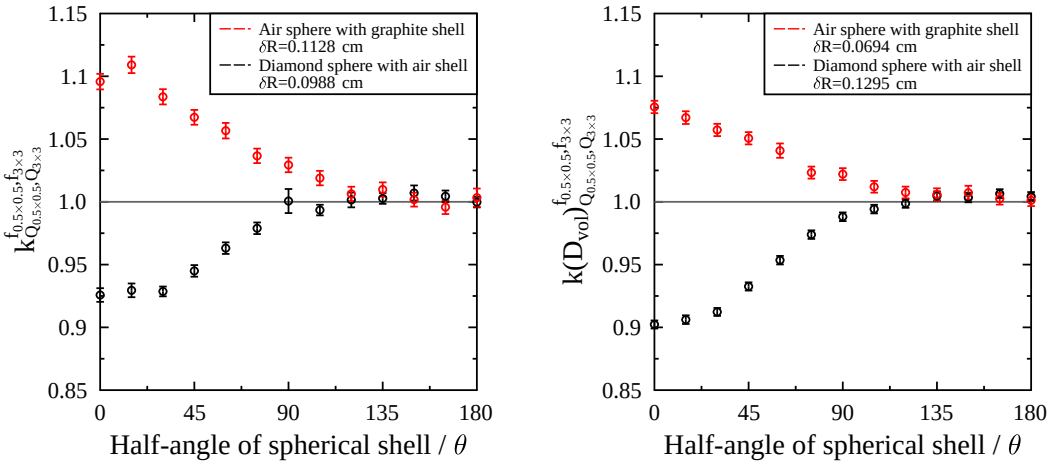

(a) (b)

FIGURE 6.8: Impact of half-angle of spherical shell on $k^{f_{\text{clin}},f_{\text{msr}}}_{\text{Q}_{\text{clin}},\text{Q}_{\text{msr}}}$ and $[k(D_{\text{vol}})]^{f_{\text{clin}},f_{\text{msr}}}_{\text{Q}_{\text{clin}},\text{Q}_{\text{msr}}}$ for 0.1 cm core-radius spheres

6.3.2 Simulations of modifications for real detectors

As the simulations for spherical geometries have shown, it is possible to manipulate both $k^{f_{\text{clin}},f_{\text{msr}}}_{\text{Q}_{\text{clin}},\text{Q}_{\text{msr}}}$ and $[k(D_{\text{vol}})]^{f_{\text{clin}},f_{\text{msr}}}_{\text{Q}_{\text{clin}},\text{Q}_{\text{msr}}}$ using mass-density compensation.

Manipulation of $[k(D_{\text{vol}})]^{f_{\text{clin}},f_{\text{msr}}}_{\text{Q}_{\text{clin}},\text{Q}_{\text{msr}}}$ is straight-forward: sensitive media with mass-density < 1 always require additional components with mass-density > 1; sensitive media with mass-density > 1 always require additional components with mass-density < 1.

Manipulation of $k_{Q_{clin},Q_{msr}}^{f_{clin},f_{msr}}$ is more complex. Results so far have demonstrated that small-field measurements, $M_{Q_{clin}}^{f_{clin}}$, are influenced by:

1. the mass density of the sensitive medium
2. the shape and size of the sensitive volume (*i.e.* its susceptibility to volume averaging)

For detectors filled with air (or other low-density sensitive media) both low-density-effects and volume averaging reduce $M_{Q_{clin}}^{f_{clin}}$ values. So if density compensation is applied with the aim of achieving unity in $k_{Q_{clin},Q_{msr}}^{f_{clin},f_{msr}}$, components with > 1 mass-density will be required.

But for detectors whose sensitive media have mass-densities > 1, the two effects compete: density acts to increase $M_{Q_{clin}}^{f_{clin}}$, whereas volume averaging acts to decrease it.

6.3.2.1 PTW Diamond detector

The Diamond PTW 60003 may be modelled as consisting of a cuboidal block of diamond embedded inside a cylindrical polystyrene case[6]. In the case of our particular detector, the cuboidal diamond block had a height of 0.026 cm and a square front-face with side-length 0.277 cm (according to the individual detector certificate from PTW).

In the quest for unity in $[k(D_{vol})]_{Q_{clin},Q_{msr}}^{f_{clin},f_{msr}}$ and $k_{Q_{clin},Q_{msr}}^{f_{clin},f_{msr}}$, two different modification designs were considered, as shown in Figure 6.9.

(a) (b) (c)

FIGURE 6.9: Diagrams to show the two different designs of modification simulated for the PTW Diamond detector. (a) The original detector. (b) Placing a lid of height δL on top of the sensitive cavity (b) Surrounding the cavity with a case of uniform height- and side- extension δC.

For the original PTW detector, the competing effects of volume averaging (lowering $k_{Q_{clin},Q_{msr}}^{f_{clin},f_{msr}}$) and the diamond's relatively high mass density (raising $k_{Q_{clin},Q_{msr}}^{f_{clin},f_{msr}}$) are rather complex. Their impact upon the modification strategy (for both lid and case modifications) is summarised in table 6.3.

	$k^{f_{\text{clin}},f_{\text{msr}}}_{Q_{\text{clin}},Q_{\text{msr}}}$ modifications	$[k(D_{\text{vol}})]^{f_{\text{clin}},f_{\text{msr}}}_{Q_{\text{clin}},Q_{\text{msr}}}$ modifications
Vertically oriented detector	Volume averaging dominates over high density effect: additional dense material is required, detector is modified using aluminium (ρ=2.70 g/cm^3).	Detector is modified using air (ρ=0.0013 g/cm^3) to counteract increased density of sensitive volume.
Horizontally oriented detector	Volume averaging is counteracted by increased density: $k^{f_{\text{clin}},f_{\text{msr}}}_{Q_{\text{clin}},Q_{\text{msr}}} \sim 1$ in a 0.5 cm field, such that no modification is necessary for this field size.	Detector is modified using air (ρ=0.0013 g/cm^3) to counteract increased density of sensitive volume.

TABLE 6.3: Modification strategies for various PTW Diamond detector configurations

The dimensions of the modifications were optimised to attain $k^{f_{0.5},f_3}_{Q_{0.5},Q_3}$=1 or $[k(D_{\text{vol}})]^{f_{0.5},f_3}_{Q_{0.5},Q_3} = 1$ for a detector, positioned on axis at a depth of 5 cm deep. The values of δL and δC ranged from 77% to 230% of the height of the diamond cavity (0.026 cm). As for the spherical cavities, the optimised modifications were also tested at other field sizes.

First let us consider the vertically orientated set-up (figure 6.10). In the case of this real detector, it appears that a single modification can attain $k^{f_{\text{clin}},f_{\text{msr}}}_{Q_{\text{clin}},Q_{\text{msr}}}$=1 to within 5% for a full range of field sizes down to 0.5×0.5 cm^2. However, for the smallest field size, the modification leads to a $k^{f_{0.25},f_3}_{Q_{0.25},Q_3}$ value that lies within 8% of unity. This relatively high discrepancy can be attributed to the fact that the side-length of the sensitive volume (0.277 cm) exceeds the side length of the field (0.25 cm as defined at the isocentre, increasing to 0.2625 cm at a depth of 5 cm due to beam divergence). Consequently, the volume averaging behaviour differs substantially between the smallest field size and all of the others. Considerably more success is achieved in the optimisation of $[k(D_{\text{vol}})]^{f_{\text{clin}},f_{\text{msr}}}_{Q_{\text{clin}},Q_{\text{msr}}}$ where the effects of volume averaging are no longer relevant.

It is interesting to note that, in the case of $k^{f_{\text{clin}},f_{\text{msr}}}_{Q_{\text{clin}},Q_{\text{msr}}}$, the modification where the sensitive cavity is topped with a compensatory lid appears to be more robust to changing field size than does the modification where the sensitive cavity is enclosed within a compensatory case (see Figure 6.9). This is consistent with the data shown in Figure 6.4(b), where (for the hypothetical spherical detector consisting of a diamond sphere surrounded by

[6]Small electrical contacts of course lie below the sensitive volume, but PTW were unwilling to provide us with any detailed information on this element of the detector design. Nonetheless, an excellent fit to experimental data was obtained for our simple virtual model, as presented in Chapter 3

an air shell) the optimisation of $[k(D_{\text{vol}})]^{f_{\text{clin}},f_{\text{msr}}}_{Q_{\text{clin}},Q_{\text{msr}}}$ breaks down when the extent of the compensatory case exceeds the field size. Thus the data suggests that modifications based upon compensatory components positioned *upstream* from the detector sensitive cavity are most robust to changing field size.

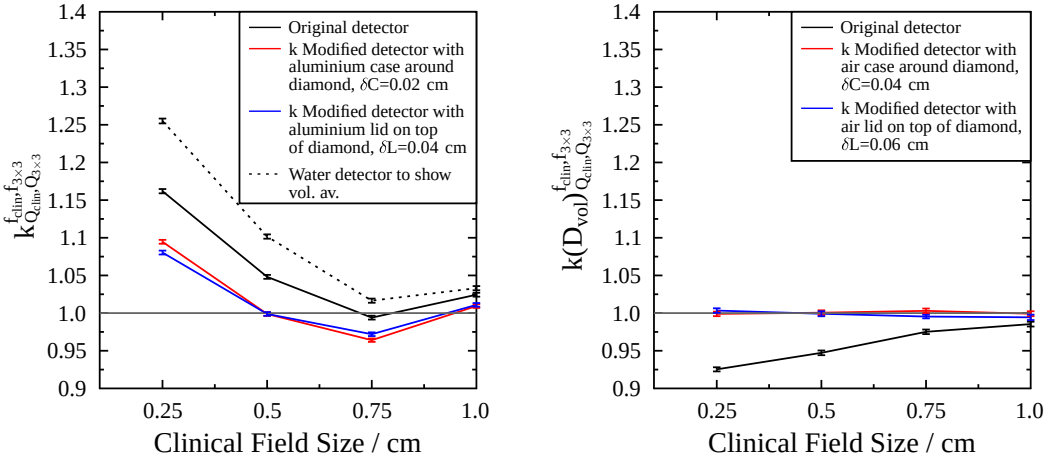

(a) $k^{f_{\text{clin}},f_{\text{msr}}}_{Q_{\text{clin}},Q_{\text{msr}}}$ (b) $[k(D_{\text{vol}})]^{f_{\text{clin}},f_{\text{msr}}}_{Q_{\text{clin}},Q_{\text{msr}}}$

FIGURE 6.10: Vertically orientated diamond detector: considering the robustness of the modifications with field size

In the case of the horizontally orientated detector, the relatively high mass-density of the sensitive region actually does a near perfect job of compensating for the volume averaging evident in a $0.5\times0.5\,\text{cm}^2$ field. However, for a $0.25\times0.25\,\text{cm}^2$ field, the compensation is less ideal ($k^{f_{0.25},f_3}_{Q_{0.25},Q_3}$ lies at $\sim$0.95). When the detector is oriented horizontally, the cuboidal sensitive volume (of width 0.026 cm and length 0.277 cm) again extends beyond the edges of the 0.25×0.25 cm field: extreme volume averaging occurs.

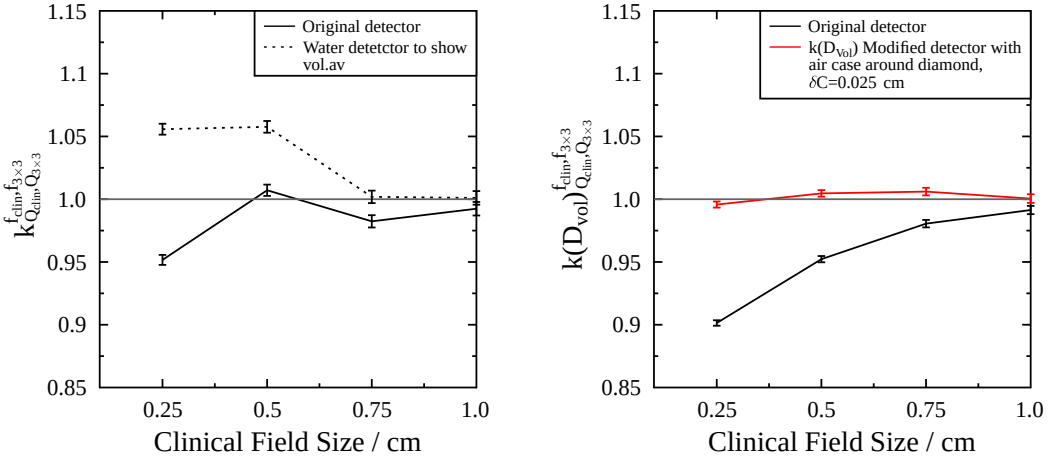

(a) $k^{f_{\text{clin}},f_{\text{msr}}}_{Q_{\text{clin}},Q_{\text{msr}}}$. Due to the near unit value of $k^{f_{\text{clin}},f_{\text{msr}}}_{Q_{\text{clin}},Q_{\text{msr}}}$ for a square clinical field size with side-length 0.5 cm, in this case the detector was not modified.

(b) $[k(D_{\text{vol}})]^{f_{\text{clin}},f_{\text{msr}}}_{Q_{\text{clin}},Q_{\text{msr}}}$

FIGURE 6.11: Horizontally orientated PTW diamond detector, considering the robustness of the proposed modifications with field size.

Considering how the modifications affect electron fluence

In order to tentatively explore the mechanism behind mass-density based compensation, simulations of electron fluence were performed. For this purpose, flurznrc (an EGSnrc code which enables fluence scoring in cylindrical geometries) was used. The cuboidal sensitive volume of the real diamond detector (thickness = 0.026 cm and side-length = 0.277 cm) was remodelled as a cylinder with the same thickness and cross-sectional area (radius 0.157 cm). The sensitive region was encased within a cylinder of polystyrene (as in the case of the real detector).

Above the diamond cavity, a cylindrical lid of height 0.05 cm was also built into the model, as shown in Figure 6.12. In case (a) this lid was constructed from polystyrene[7], in case (b) it was constructed from air, and case (c) considered a lid made from aluminium.

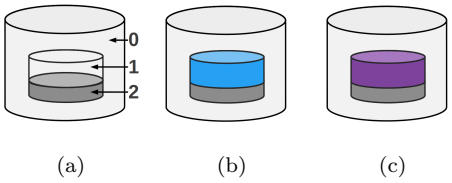

FIGURE 6.12: Fluence scoring. (i) Diagram to show scoring regions, (a) Original detector scenario: regions 0 and 1 are polystyrene, region 2 is diamond, (b) Air lid: region 0 is polystyrene, region 1 is air, region 2 is diamond, (c) Aluminium lid: region 0 is polystyrene, region 1 is aluminium, region 2 is diamond.

All simulations were performed with the centre of the diamond cavity positioned at a depth of 5 cm in a large model water tank at an SSD of 100 cm. For two different field sizes ($0.5\times0.5\,cm^2$ and $3\times3\,cm^2$), the total electron fluence averaged over the volume was scored in both the lid above the cavity and in the cavity itself. The results are plotted in Figure 6.13.

It is clear that, under small field conditions (Figure 6.13 (a) and (b)), differences in the electron fluence in the lid propagate through to differences in the electron fluence in the cavity. Whilst the detector modifications lead to pronounced differences in cavity fluence in the case of the $0.5\times0.5\,cm^2$ field, for the $3\times3\,cm^2$ field - where lateral scattering of electrons into the cavity is much more important - the impact of the modifications is relatively minor.

[7]Such that a near replica of the actual detector was modelled

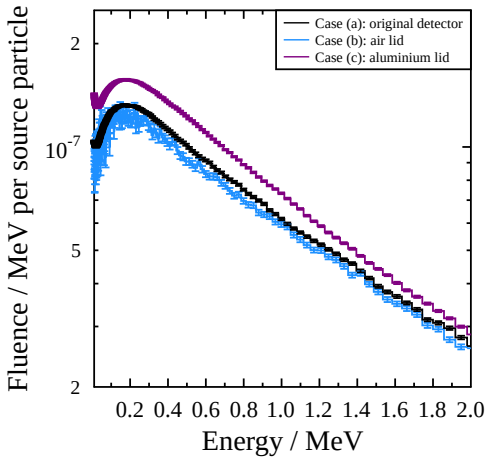

(a) $0.5 \times 0.5\,\mathrm{cm}^2$ field fluence scoring in region 1 (the lid)

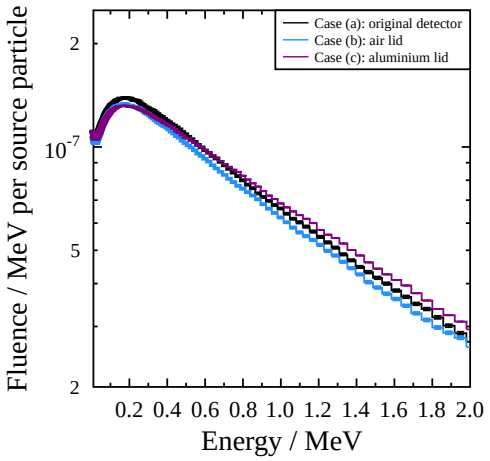

(b) $0.5 \times 0.5\,\mathrm{cm}^2$ field fluence scoring in region 2 (the cavity itself)

FIGURE 6.13: Scoring the total electron fluence averaged over the volume of (i) the lid above the diamond cavity (left hand plots) and (ii) the cavity itself (right hand plots). In all cases, the centre of the cavity was positioned at a depth of 5 cm. The model detectors were irradiated inside a large model water tank, located at an SSD of 100 cm and irradiated by either a $0.5 \times 0.5\,\mathrm{cm}^2$ field (plots above) or a $3 \times 3\,\mathrm{cm}^2$ (plots below).

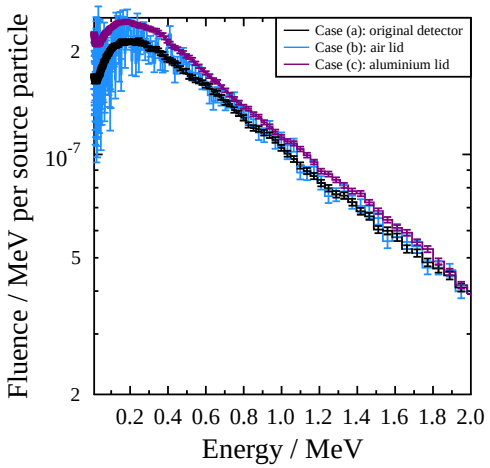

(c) $3 \times 3\,\mathrm{cm}^2$ field fluence scoring in region 1 (the lid)

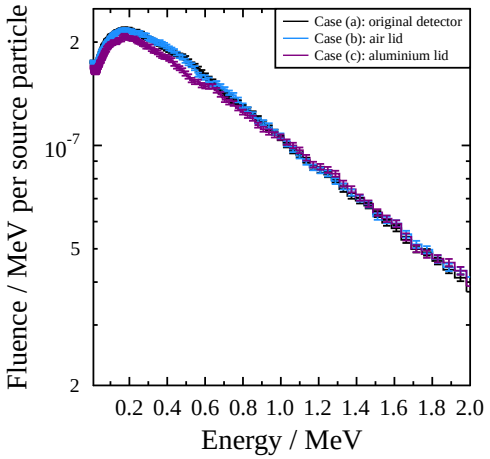

(d) $3 \times 3\,\mathrm{cm}^2$ field fluence scoring in region 2 (the cavity itself)

6.3.2.2 PTW PinPoint Ionisation Chamber

The second real detector that was modelled was the PinPoint PTW 31006. This ionisation chamber consists of a cylinder of steel (the inner electrode), in an air cavity surrounded a hemispherically-tipped-cylinder of graphite (the outer electrode), all coated in PMMA. Due to its low-density air-filled sensitive volume, the PinPoint detector requires a high-density compensatory component in order to achieve a value of one for $[k(D_{\text{vol}})]^{f_{\text{clin}},f_{\text{msr}}}_{\text{Q}_{\text{clin}},\text{Q}_{\text{msr}}}$ and $k^{f_{\text{clin}},f_{\text{msr}}}_{\text{Q}_{\text{clin}},\text{Q}_{\text{msr}}}$. In the modifications considered here, the medium of the outer electrode was transformed from graphite (ρ=1.85 g/cm^3) to aluminium (ρ=2.70 g/cm^3)[8]. In the original detector, the graphite outer-electrode had a thickness of 0.015 cm. Here, in the modified versions, the total thickness of the alternative aluminium electrode is quoted as δE. The value of δE was optimised to attain either $[k(D_{\text{vol}})]^{f_{0.5},f_3}_{\text{Q}_{0.5},\text{Q}_3}$=1 or $k^{f_{0.5},f_3}_{\text{Q}_{0.5},\text{Q}_3}$=1, with the detector positioned on-axis at a depth of 5 cm. In the proposed modifications, in addition to the material transformation, the thickness of the outer electrode is increased by a factor of up to 4.33 (in the case of $k^{f_{\text{clin}},f_{\text{msr}}}_{\text{Q}_{\text{clin}},\text{Q}_{\text{msr}}}$). Of course, this factor could have been reduced had a material of greater density been used. Scale diagrams of the proposed modifications are included in Figure 6.14.

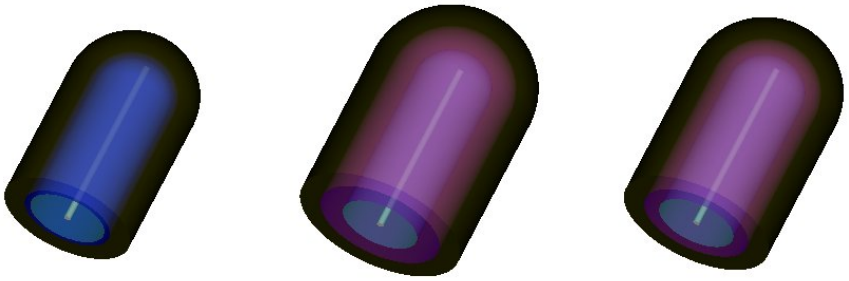

(a) (b) (c)

FIGURE 6.14: Scale diagrams to show the application of density-compensated design-modifications to the PinPoint ionisation chamber. In all cases, a uniform coating (of equal thickness) of PMMA is shown in black on the outside of the detector. Figure (a) shows the original PinPoint with its graphite outer-electrode (of thickness 0.015 cm) in blue. Figure (b) shows the $k^{f_{0.5},f_3}_{\text{Q}_{0.5},\text{Q}_3}$ density-compensated PinPoint with aluminium outer-electrode shown in purple: here the total electrode thickness δE=0.065 cm. Figure (c) shows the $[k(D_{\text{vol}})]^{f_{0.5},f_3}_{\text{Q}_{0.5},\text{Q}_3}$ density-compensated PinPoint, where δE=0.04 cm.

Figure 6.15 demonstrates that, for a 0.5×0.5 cm^2 field, the modifications detailed in Figure 6.14 prove relatively robust to changes in detector off-axis position. As shown in the lower axis of Figure 6.15(b), the correction factor for the detector modified according to $[k(D_{\text{vol}})]^{f_{0.5},f_3}_{\text{Q}_{0.5},\text{Q}_3}$ maintains its unit value well into the penumbral region of the field. Unfortunately the statistical uncertainties cloud the off-axis behaviour of $k^{f_{0.5},f_3}_{\text{Q}_{0.5},\text{Q}_3}$, but excellent performance is clearly achieved within the field itself.

[8] In this work, adaptation of the inner electrode was not considered in order to preserve the volume of the sensitive region.

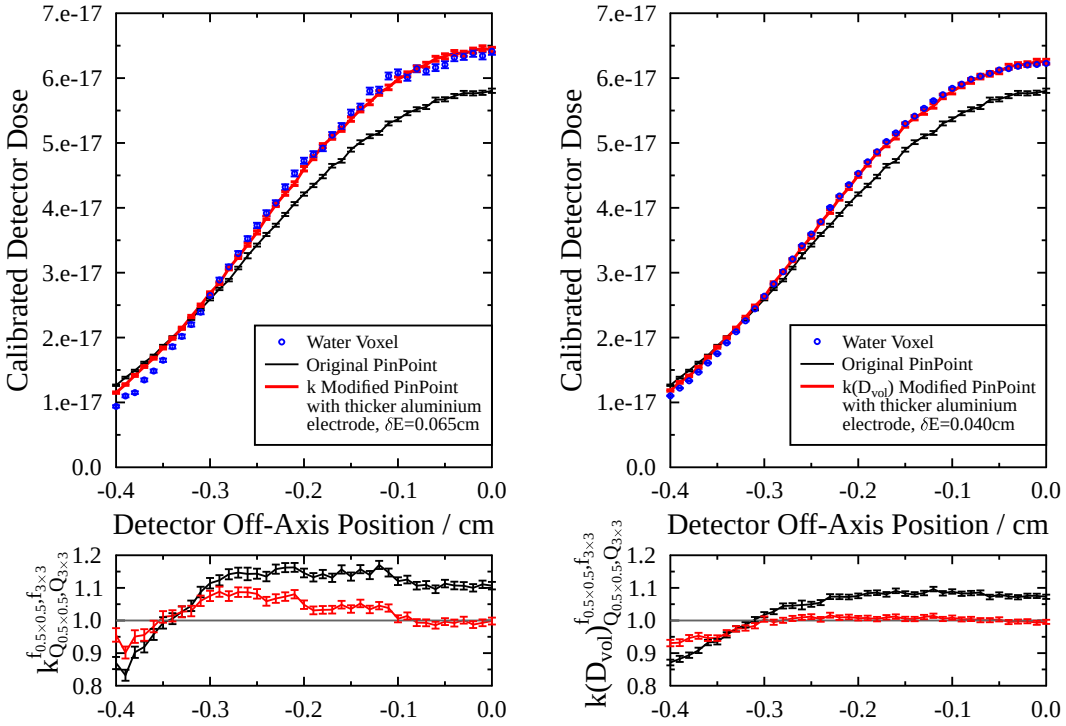

(a) $k^{f_{\text{clin}},f_{\text{msr}}}_{\text{Q}_{0.5},\text{Q}_3}$ (b) $[k(D_{\text{vol}})]^{f_{\text{clin}},f_{\text{msr}}}_{\text{Q}_{0.5},\text{Q}_3}$

FIGURE 6.15: Robustness of PinPoint modifications to off-axis position within a square clinical field of side length 0.5 cm.

The robustness of the proposed PinPoint modifications to changing field size is considered in Figure 6.16. For the original PinPoint detector, at all field sizes, the magnitude of the correction factors is large (*e.g.* $k^{f_{0.25},f_3}_{\text{Q}_{0.25},\text{Q}_3}$=1.28 and $[k(D_{\text{vol}})]^{f_{0.5},f_3}_{\text{Q}_{0.5},\text{Q}_3}$=1.18). Whilst the performance of the modified detectors is somewhat less than ideal, the resulting correction factors are consistent with unity to within 8%.

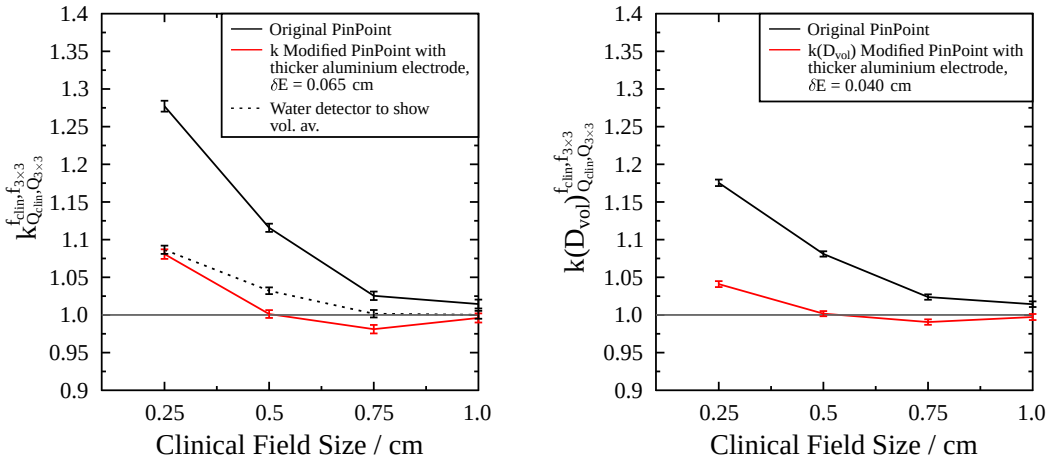

(a) $k^{f_{\text{clin}},f_{\text{msr}}}_{\text{Q}_{\text{clin}},\text{Q}_{\text{msr}}}$ (b) $[k(D_{\text{vol}})]^{f_{\text{clin}},f_{\text{msr}}}_{\text{Q}_{\text{clin}},\text{Q}_{\text{msr}}}$

FIGURE 6.16: Considering the robustness of PinPoint $k^{f_{\text{clin}},f_{\text{msr}}}_{\text{Q}_{\text{clin}},\text{Q}_{\text{msr}}}$ and $[k(D_{\text{vol}})]^{f_{\text{clin}},f_{\text{msr}}}_{\text{Q}_{\text{clin}},\text{Q}_{\text{msr}}}$ modifications to changing field size.

6.4 Conclusion

Detectors often consist of several components whose mass densities differ substantially from water. It is well known that inserts of non-water-like mass-density have the capacity to perturb radiotherapy dose distributions both in dosimeters and in patient treatment plans. However, mass-density compensation has not yet been utilised to improve dosimeter water-equivalence / performance in non-equilibrium conditions.

Simulations show that by covering or encasing the sensitive region of the PTW diamond detector 60003 with an appropriate layer of air, the instrument can be made to behave as though it was made entirely from water. For a single detector orientation (horizontal or vertical), one modification can lead to water-equivalent performance under a wide variety of non-equilibrium conditions (different field sizes, off-axis positions and detector depths).

Ionisation chambers such as the PinPoint PTW 31006 require considerable quantities of high-density material to compensate for the excessively low density of air. However, provided that the compensatory material can be positioned appropriately (within the field boundaries), it is again possible to make the detector behave as though it were constructed from water alone.

The findings presented here explain a number of previous observations in retrospect. For instance, Martens *et al* [88] placed a metalic plate above a liquid-filled ion-chamber array and observed penumbral sharpening (for intensity modulated fields): the performance of their array was improved via mass-density compensation. And the promising results of the IMRT calorimetry probe developed by Renaud *et al* [89] are likely to be attributable to the cylindrical nesting of relatively high-density graphite ($1.72\,\mathrm{g/cm^3}$) components with relatively low-density Pyrogel® ($0.17\,\mathrm{g/cm^3}$). The results of this study also add to the evidence that plastic scintillation detectors - with near unit density - may become a non-equilibrium dosimeter of choice [90–92].

In summary, for existing solid-state dosimeters / air-filled ionisation chambers within 6 MV photon fields, simulations show that near perfect water-equivalence can be achieved using a single modification, which for a given detector orientation, will perform well over a wide range of irradiation conditions (field sizes, depths and off-axis positions). If such an entirely water equivalent detector were to be manufactured, the dose distributions it measured would be perturbed only due to volume averaging which is well understood and could be corrected-for on a local basis.

Furthermore, this work shows that for detector cavities of certain shapes and small sizes, mass-density-compensation may be used to manipulate dosimeter response in order to

obtain near-unit small-field correction factors. In this manner, dosimeters can be made to behave like point-like water structures. Thus, provided that adequate sensitivity can be achieved for a small-sensitive volume, it may be possible to use Monte Carlo-driven design to produce a solid-state dosimeter / air-filled ionisation chamber with a near-perfect small-field response.

Chapter 7

Conclusion

Chapter 1 of this thesis highlighted that small field dosimetric data should ideally be obtained using (i) a dosimeter with very high spatial resolution and (ii) a robust, internationally accepted Code of Practice to account for the dosimeter's remaining perturbative effects and to link its output back to that of a primary standard at a National Standards Laboratory.

Neither of these ideals are currently available. In Autumn 2008 the working group on reference dosimetry of the IAEA and AAPM (Alfonso *et al.*) published "A new formalism for reference dosimetry of small and nonstandard fields". Their paper presents a framework (based upon point-dose correction factors) that enables reference dosimetry to be applied to single detector position measurements within small fields. However as shown in Chapter 4 of this thesis and numerous published studies [15, 29–32], point-dose correction factors ($k_{Q_{clin},Q_{msr}}^{f_{clin},f_{msr}}$) depend strongly on detector design, field size, detector position and detector azimuthal angle. Accurate $k_{Q_{clin},Q_{msr}}^{f_{clin},f_{msr}}$ values are not easy to obtain, their determination typically requiring time-intensive Monte Carlo simulations calculated using a validated beam model. Consequently, although the approach of Alfonso et al [25] is conceptually useful, obtaining the correction factors it requires with sufficient accuracy proves practically difficult.

It has been suggested by Djouguela et al [79] and Sánchez-Doblado et al [86] that the area dose integral in a plane perpendicular to the beam axis, measured using an ionisation chamber whose area is larger than the field, provides a useful dose metric for small fields. Chapter 5 of this thesis demonstrates that the surface integral concept may also prove useful for conventional (small) dosimeters. Although inter-detector measurement variations of many percent are demonstrable at individual positions within small fields, the results of Chapter 5 indicate that the application of conventional (detector-specific)

large-field calibration factors leads to accurate measurement of the dose area product (integral dose).

Following the Alfonso formalism, point-dose to water in a small field ('*clin*') is obtained using equation 7.1:

$$D^{f_{\text{clin}}}_{\text{w,Q}_{\text{clin}}} = M^{f_{\text{clin}}}_{\text{Q}_{\text{clin}}} \cdot \left\{ \frac{D^{f_{\text{clin}}}_{\text{w,Q}_{\text{clin}}} / M^{f_{\text{clin}}}_{\text{Q}_{\text{clin}}}}{D^{f_{\text{msr}}}_{\text{w,Q}_{\text{msr}}} / M^{f_{\text{msr}}}_{\text{Q}_{\text{msr}}}} \right\} \cdot \left[\frac{D^{f_{\text{msr}}}_{\text{w,Q}_{\text{msr}}}}{M^{f_{\text{msr}}}_{\text{Q}_{\text{msr}}}} \right] \tag{7.1}$$

$$= M^{f_{\text{clin}}}_{\text{Q}_{\text{clin}}} \cdot \left\{ \frac{D^{f_{\text{clin}}}_{\text{w,Q}_{\text{clin}}} / M^{f_{\text{clin}}}_{\text{Q}_{\text{clin}}}}{D^{f_{\text{msr}}}_{\text{w,Q}_{\text{msr}}} / M^{f_{\text{msr}}}_{\text{Q}_{\text{msr}}}} \right\} \cdot C \tag{7.2}$$

where the term in braces is the small-field point-dose correction factor, $k^{f_{\text{clin}},f_{\text{msr}}}_{\text{Q}_{\text{clin}},\text{Q}_{\text{msr}}}$ and the term in square brackets is the classical reference field calibration factor, C. Should a small, linearly-responding dosimeter be used to integrate dose over a high resolution grid of positions inside and outside the boundaries of a radiation field, such that integral-dose is considered rather than the point-dose, equation 7.1 can be vastly simplified to:

$$DAP^{f_{\text{clin}}}_{\text{w,Q}_{\text{clin}}} = MAP^{f_{\text{clin}}}_{\text{Q}_{\text{clin}}} \cdot C \tag{7.3}$$

where: $MAP^{f_{\text{clin}}}_{\text{Q}_{\text{clin}}}$ is an un-calibrated detector integral-dose reading and no correction factors need be applied other than the conventional calibration factor, C.

Consequently it follows that if a single dosimeter is used for all treatment planning system (TPS) commissioning measurements (including off-axis profiles and output factors) the integral dose calculated by the TPS should be robust, regardless of the detector type - provided that the detector responds linearly with dose-rate and the response of the detector is relatively energy independent[1]. However errors could potentially occur if the TPS integral dose were to become distorted by the application of various point-dose correction factors, each associated with its own uncertainty.

In summary, Chapter 5 demonstrated that DAPs can be measured accurately for small fields using detectors calibrated in wide fields, despite the fact that dose measurement at individual points requires corrections specific to the field size and detector design, position and orientation.

[1]Should the detector's response to changing beam spectrum (*e.g.* with depth) vary substantially then a depth-specific calibration factor might be needed; *i.e.* it might be necessary to calibrate the detector in a $10\times10\,\text{cm}^2$ field at various depths to correctly calculate the DAP at each one.

As an alternative strategy, Chapter 6 investigated whether it might be possible to reduce the scale of those corrections, or eliminate them altogether, by modifying detector designs. Further to the work of Scott et al [16], this study shows that, under small field conditions, mass density is the principal determinant of detector water-equivalence. Detectors whose sensitive volumes have relatively low density (*e.g.* the MicroLion and the PinPoint) can potentially be improved by adding high density media into the detector design. And conversely, the water-equivalence of solid-state detectors such as the Ediode and Diamond can be improved by adding low density filler media into the detector design. The results presented in Chapter 6 show that, for any detector whose cavity is sufficiently small, "mass-density compensation" may be used to manipulate the response of that detector in order to obtain near-unit $k_{Q_{clin},Q_{msr}}^{f_{clin},f_{msr}}$ values for a variety of small field scenarios. Thus, provided that adequate sensitivity can be achieved using small-sensitive volumes, it may be possible to use Monte Carlo-driven design to produce real dosimeters with a near-perfect small-field response.

This research could be taken forward via (i) further investigation into the validity of the assumptions of the DAP theorem and also the theorems applicability to detector arrays; and (ii) prototyping and experimental testing of real detectors with designs optimised (for non-equilibrium dosimetry) according to the principle of mass-density-compensation.

Appendix A

Mathematical formulations of DAP

A.1 Basic formulation

The total particle fluence I may be described by an infinite number of unattenuated pencil beams along the x and the y axes: where $I(x, y)$ is the fluence of a single pencil beam at position $\vec{x} = \{x, y\}$.

For a detector positioned at $\vec{r} = \{r_{\mathrm{x}}, r_{\mathrm{y}}\}$, $f(x - r_{\mathrm{x}}, y - r_{\mathrm{y}})$ gives the fraction of the fluence of the single pencil beam at $\vec{x}$ which is registered by the detector. $(\vec{x} - \vec{r}) = \vec{q}$ is the separation between the detector and the pencil beam.

For a single detector position, $\vec{r}$ and a single pencil beam position, $\vec{x}$, consider the static meter-reading which will be obtained, $M(\vec{x}, \vec{r})$:

$$M(\vec{x}, \vec{r}) = I(x, y) f(x - r_{\mathrm{x}}, y - r_{\mathrm{y}}) \tag{A.1}$$

This is the meter-reading obtained for a detector at position r due to a pencil beam at position $\{x, y\}$. The detector dwell time and linac dose-rate are assumed to be constant.

For a single detector position, integrate over all of the pencil beams:

$$M(\vec{r}) = \int_{-\infty}^{+\infty} \int_{-\infty}^{+\infty} I(x, y) f(x - r_{\mathrm{x}}, y - r_{\mathrm{y}}) \, \mathrm{d}x \mathrm{d}y \tag{A.2}$$

Let us now consider the case of a very wide calibration field, with our static detector positioned at the origin ($\vec{r} = 0$), from equation A.2 we have:

$$M_{\text{wide}}(0) = \int_{-\infty}^{+\infty} \int_{-\infty}^{+\infty} I(x,y) f(x,y)\, \mathrm{d}x\mathrm{d}y \tag{A.3}$$

However, in the case where the x and y profiles are sufficiently wide relative to the detector response function f, $I(x,y)$ becomes a constant, which we will call I_{wide}. Then:

$$\frac{M_{\text{wide}}(0)}{I_{\text{wide}}} = \int_{-\infty}^{+\infty} \int_{-\infty}^{+\infty} f(x,y)\, \mathrm{d}x\mathrm{d}y \tag{A.4}$$

In the case of a very wide calibration field, it is possible to convert between a detector meter-reading M and a water dose D by applying the detector-specific calibration factor C_{wide}:

$$C_{\text{wide}} = \frac{D_{\text{wide}}(0)}{M_{\text{wide}}(0)} \tag{A.5}$$

so that equation A.4 may be written in terms of dose to water, D:

$$\frac{D_{\text{wide}}(0)}{C_{\text{wide}} \times I_{\text{wide}}} = \int_{-\infty}^{+\infty} \int_{-\infty}^{+\infty} f(x,y)\, \mathrm{d}x\mathrm{d}y \tag{A.6}$$

In order to obtain the Meter-reading Area Product (MAP), integrate the meter-reading of equation A.2 over all detector positions:

$$MAP = \int_{\mathrm{a}}^{b} \mathrm{d}r_{\mathrm{x}} \int_{\alpha}^{\beta} \mathrm{d}r_{\mathrm{y}} \int_{-\infty}^{+\infty} \mathrm{d}x \int_{-\infty}^{+\infty} \mathrm{d}y\ I(x,y) f(x - r_{\mathrm{x}}, y - r_{\mathrm{y}}) \tag{A.7}$$

change variables, $(x - r_{\mathrm{x}}) = -p$, $(y - r_{\mathrm{y}}) = -q$ and use $f(p,q) = f(-p,-q)$,

$$MAP = \int_{-\infty}^{+\infty} \mathrm{d}x \int_{-\infty}^{+\infty} \mathrm{d}y \int_{\mathrm{a-x}}^{b-x} \mathrm{d}p \int_{\alpha-\mathrm{y}}^{\beta-y} \mathrm{d}q\ I(x,y) f(p,q) \tag{A.8}$$

If the detector limits a, b, α and β are positioned sufficiently beyond the field edges, then we can make the substitutions: $a - x = -\infty$, $b - x = \infty$, $\alpha - y = -\infty$ and $\beta - y = \infty$:

$$MAP = \int_{-\infty}^{+\infty} \mathrm{d}x \int_{-\infty}^{+\infty} \mathrm{d}y \int_{-\infty}^{+\infty} \mathrm{d}p \int_{-\infty}^{+\infty} \mathrm{d}q\ I(x,y) f(p,q) \tag{A.9}$$

Substituting equation A.6 into equation A.9 gives:

$$MAP \times C_{\text{wide}} = \frac{D_{\text{wide}}(0)}{I_{\text{wide}}} \int_{-\infty}^{+\infty} \mathrm{d}x \int_{-\infty}^{+\infty} \mathrm{d}y\ I(x,y) \tag{A.10}$$

It is clear that the right-hand side of equation A.10 is independent of the detector used, consisting of nothing more than a series of constants for a particular radiation field:

- both the double integral of the pencil beams and I_{wide} are related to the fluence of the radiation field
- D_{wide} is the **calibrated** wide-field dose delivered to water for the fixed detector dwell-time considered throughout this formulation.

Because of the dimensions of $MAP \times C_{\text{wide}}$ are those of a dose times an area [Gy m^2], we term it the dose area product or DAP:

$$DAP = \frac{D_{\text{wide}}(0)}{I_{\text{wide}}} \int_{-\infty}^{+\infty} \mathrm{d}x \int_{-\infty}^{+\infty} \mathrm{d}y \; I(x,y) \tag{A.11}$$

A.1.0.3 Assumptions made in deriving the formulation

1. The detector responds linearly with dose
2. The linac dose-rate and detector dwell-time remain constant and infinite detector positions are considered to obtain the integrated meter-readings
3. All pencil beams making up the field are exactly the same
4. Profiles of measured fields extend sufficiently beyond the field edge that, at the profile limits, the detector response falls to zero
5. The calibration field is sufficiently wide that the central axis detector response function falls to zero for the furthest pencil beams

A.2 Discretised mathematical formulation of DAP

In reality, it is impossible to integrate readings from an infinite series of detector positions over an infinitely large two-dimensional area. Practically, a discretised form of DAP must be considered.

For uniform inter-detector-position spacing, this is straight-forward. Considering equation A.7, for a field with two-fold reflective symmetry, we can obtain the total discretised DAP by examining a single quadrant:

$$DAP = 4\,\delta^2 \sum_{\mathrm{n}=0}^{n_{\max}} \sum_{\mathrm{k}=0}^{k_{\max}} \int_{-\infty}^{+\infty} dx \int_{-\infty}^{+\infty} dy I(x,y) f(x - n\delta, y - k\delta) \tag{A.12}$$

Here δ is the inter-detector-position spacing (which is constant) and $n_{\max}$ and $k_{\max}$ are integer values linked to the extreme values of the detector-positions, E, by:

$$n_{\max} = \frac{E_{\mathrm{x}}}{\delta} \tag{A.13}$$

$$k_{\max} = \frac{E_{\mathrm{y}}}{\delta} \tag{A.14}$$

The size of δ and $n_{\max}/k_{\max}$ then determine the validity of the approximation of the discrete DAP to the integral DAP presented in Section A.1.

An interesting extension of this study would be to determine the values of δ and $n_{\max}/k_{\max}$ at which DAP constancy breaks down. If the required δ is greater than the minimum inter-detector spacing to prevent interference between detectors, then there should be no problem in using arrays.

Bibliography

[1] M. Aspradakis, J.P. Byrne, H. Palmans, J. Conway, K. Rosser, J. Warrington, and S. Duane. *Report Number 103: Small Field MV Photon Dosimetry.* IPEM, 2010.

[2] S. Derreumaux, C. Etard, C. Huet, F. Trompier, I. Clairand, J.-F. Bottollier-Depois, B. Aubert, and P. Gourmelon. Lessons from recent accidents in radiation therapy in France. *Radiation Protection Dosimetry*, 131(1):130–5, 2008.

[3] R. Mohan, C. Chui, and L. Lidofsky. Energy and angular distributions of photons from medical linear accelerators. *Medical Physics*, 12(5):592–597, 1985.

[4] P. Mayles, A. Nahum, and J. Rosenwald. *Handbook of radiotherapy physics: theory and practice.* Taylor and Francis, 2007.

[5] H. Attix. *Introduction to Radiological Physics and Radiation Dosimetry.* Wiley-VCH, 2004.

[6] F. De Laney and H. Kooy. *Atoms, Radiation, and Radiation Protection.* James E. Turner, 2008.

[7] R. Loevinger. A formalism for calculation of absorbed dose to a medium from photon and electron beams. *Medical Physics*, 8(1):1–12, 1981.

[8] ICRU. *Stopping powers for electrons and positrons.* ICRU Report No. 37, 1984.

[9] ICRU. *Prescribing, Recording and Reporting Photon Beam Therapy.* ICRU Report No. 50, 1993.

[10] ICRU. *Determination of Absorbed Dose in a Patient Irradiated by Beams of X or Gamma Rays in Radiotherapy Procedures.* ICRU Report No. 24, 1993.

[11] A. Brahme. Dosimetric Precision Requirements in Radiation Therapy. *Acta Oncologica*, 23:379–391, 1984.

[12] P. Andreo, D.T. Burns, K. Hohlfeld, M.S. Huq, T. Kanai, F. Laitano, V.G. Smyth, and S. Vynckier. Absorbed dose determination in external beam radiotherapy. IAEA Technical Reports Series No. 398, 2000.

[13] H. Bouchard, J. Seuntjens, J. Carrier, and I. Kawrakow. Ionization chamber gradient effects in nonstandard beam configurations. *Medical Physics*, 36:4654–4663, 2009.

[14] F. Crop, N. Reynaert, G. Pittomvils, L. Paelinck, C. De Wagter, L. Vakaet, and H. Thierens. The influence of small field sizes, penumbra, spot size and measurement depth on perturbation factors for microionization chambers. *Physics in Medicine and Biology*, 54:2951–69, 2009.

[15] P. Francescon, S. Cora, and N. Satariano. Calculation of $k_{Q_{clin},Q_{msr}}^{f_{clin},f_{msr}}$ for several small detectors and for two linear accelerators using Monte Carlo simulations. *Medical Physics*, 38:6513–6527, 2011.

[16] A.J.D. Scott, S. Kumar, A.E. Nahum, and J.D. Fenwick. Characterizing the influence of detector density on dosimeter response in non-equilibrium small photon fields. *Physics in Medicine and Biology*, 57:4461–4476, 2012.

[17] L.V. Spencer and F.H. Attix. A theory of cavity ionization. *Radiation Research*, 3(3):239–254, 1955.

[18] A.E. Nahum. Water/air mass stopping power ratios for megavoltage photon and electron beams. *Physics in Medicine and Biology*, 23(1):24–38, January 1978.

[19] S.C. Lillicrap, B. Owen, J.R. Williams, and P.C Williams. Code of practice for high-energy photon therapy dosimetry based on the NPL absorbed dose calibration service. *Physics in Medicine and Biology*, 35(10):1355, 1990.

[20] G.X. Ding and F. Ding. Beam characteristics and stopping-power ratios of small radiosurgery photon beams. *Physics in Medicine and Biology*, 57(17):5509, 2012.

[21] A.J.D. Scott, A.E. Nahum, and J.D. Fenwick. Using a Monte Carlo model to predict dosimetric properties of small radiotherapy photon fields. *Medical Physics*, 35(10):4671–4684, 2008.

[22] F. Sanchez-Doblado, P. Andreo, R. Capote, A. Leal, M. Perucha, R. Arráns, L. Nú nez, E. Mainegra, J.I. Lagares, and E. Carrasco. Ionization chamber dosimetry of small photon fields: a Monte Carlo study on stopping-power ratios for radiosurgery and IMRT beams. *Physics in Medicine and Biology*, 48(14):2081, 2003.

[23] H. Palmans *et al.* BEST IN PHYSICS (THERAPY) - An international Code of Practice for the dosimetry of small static photon fields http://www.aapm.org/meetings/2012am/PRAbs.asp?mid=68&aid=18263. *Abstract for oral presentation at 54th AAPM Annual Meeting, session code: TH-E-BRB-5*, 2012.

[24] H. Palmans *et al.* Progress report of an international (IAEA/AAPM) working group on small and composite field dosimetry http://www-pub.iaea.org/MTCD/Publications/PDF/Newsletters/SSDL-NL-59.pdf. *SSDL Newsletter, No. 59*, 2011.

[25] R. Alfonso, P. Andreo, R. Capote, M. Saiful Huq, W. Kilby, P. Kjall, T.R. Mackie, H. Palmans, K. Rosser, J. Seuntjens, W. Ullrich, and S. Vatnitsky. A new formalism for reference dosimetry of small and nonstandard fields. *Medical Physics*, 35:5179–5186, 2008.

[26] K. Eklund and A. Ahnesj. Modeling silicon diode dose response factors for small photon fields. *Physics in Medicine and Biology*, 55(24):7411, 2010.

[27] D. Czarnecki and K. Zink. Monte Carlo calculated correction factors for diodes and ion chambers in small photon fields. *Physics in Medicine and Biology*, 58(8):2431, 2013.

[28] A. Gago-Arias, E. Antolin, F. Fayos-Ferrer, R. Simon, D.M. González-castaño, H. Palmans, P. Sharpe, F. Gomez, and J. Pardo-Montero. Correction factors for ionization chamber dosimetry in Cyberknife: Machine-specific, plan-class, and clinical fields. *Medical Physics*, 40(1):011721, 2013.

[29] E. Sterpin, T. R. Mackie, and S. Vynckier. Monte Carlo computed machine-specific correction factors for reference dosimetry of TomoTherapy static beam for several ion chambers. *Medical Physics*, 39:4066–4072, 2012.

[30] E. Pantelis, A. Moutsatsos, K. Zourari, L. Petrokokkinos, L. Sakelliou, W. Kilby, C. Antypas, P. Papagiannis, P. Karaiskos, E. Georgiou, and I. Seimenis. On the output factor measurements of the cyberknife iris collimator small fields: Experimental determination of the $k^{f_{\text{clin}},f_{\text{msr}}}_{\text{Q}_{\text{clin}},\text{Q}_{\text{msr}}}$ correction factors for microchamber and diode detectors. *Medical Physics*, 39:4875–4885, 2012.

[31] G. Cranmer-Sargison, S. Weston, J.A. Evans, N.P. Sidhu, and D.I. Thwaites. Monte Carlo modelling of diode detectors for small field MV photon dosimetry: detector model simplification and the sensitivity of correction factors to source parameterization. *Physics in Medicine and Biology*, 57:5141–5153, 2012.

[32] P. Francescon, W. Kilby, N. Satariano, and S. Cora. Monte Carlo simulated correction factors for machine specific reference field dose calibration and output factor measurement using fixed and iris collimators on the CyberKnife system. *Physics in Medicine and Biology*, 57:3741–3758, 2012.

[33] J.J. Duderstadt and W. M. Martin. *Transport Theory*. Wiley, New York, 1979.

[34] G. A. Failla and T. Wareing Y. Archambault S. Thompson. Acuros ® XB advanced dose calculation for the eclipse™ treatment planning system. Technical report, 2012.

[35] K.A. Gifford, J.L. Horton Jr, T.A. Wareing, G. Failla, and F. Mourtada. Comparison of a finite-element multigroup discrete-ordinates code with Monte Carlo for radiotherapy calculations. *Physics in Medicine and Biology*, 51(9):2253, 2006.

[36] S. Lloyd and W. Ansbacher. Evaluation of an analytic linear Boltzmann transport equation solver for high-density inhomogeneities. *Medical Physics*, 40(1):011707, 2013.

[37] M.W.K. Kan, L.H.T. Leung, R.W.K. So, and P.K.N. Yu. Experimental verification of the acuros XB and AAA dose calculation adjacent to heterogeneous media for IMRT and RapidArc of nasopharygeal carcinoma. *Medical Physics*, 40(3):031714, 2013.

[38] T. Han, F. Mourtada, K. Kisling, J. Mikell, D. Followill, and R. Howell. Experimental validation of deterministic acuros XB algorithm for imrt and vmat dose calculations with the radiological physics center's head and neck phantom. *Medical Physics*, 39(4):2193–2202, 2012.

[39] T. Han, J.K. Mikell, M. Salehpour, and F. Mourtada. Dosimetric comparison of acuros XB deterministic radiation transport method with Monte Carlo and model-based convolution methods in heterogeneous media. *Medical Physics*, 38(5):2651–2664, 2011.

[40] A. Fogliata, G. Nicolini, A. Clivio, E. Vanetti, and L. Cozzi. Dosimetric evaluation of acuros XB advanced dose calculation algorithm in heterogeneous media. *Radiation Oncology*, 6(1):82, 2011.

[41] D.W.O. Rogers. Fifty years of Monte Carlo simulations for medical physics. *Physics in Medicine and Biology*, 51(13):R287, 2006.

[42] F.B. Brown. *MCNP - A general Monte Carlo particle transport code.* Number Version 5. Report LA-UR-03. Los Alamos National Laboratory, 2003.

[43] J. Allison, K. Amako, J. Apostolakis, H. Araujo, P.A. Dubois, and M. *et al.* Asai. Geant4 developments and applications. *Nuclear Science, IEEE Transactions on*, 53(1):270–278, 2006.

[44] S. Jan, D. Benoit, E Becheva, T. Carlier, F. Cassol, P. Descourt, T. Frisson, L. Grevillot, L. Guigues, L. Maigne, C. Morel, Y. Perrot, N. Rehfeld, D. Sarrut, D.R. Schaart, S. Stute, U. Pietrzyk, D. Visvikis, N. Zahra, and I. Buvat. GATE V6: a

major enhancement of the GATE simulation platform enabling modelling of ct and radiotherapy. *Physics in Medicine and Biology*, 56(4):881, 2011.

[45] G. Battistoni, F. Cerutti, A. Fasso, A. Ferrari, S. Muraro, J. Ranft, S. Roesler, and P.R. Sala. The FLUKA code: description and benchmarking. *AIP Conference Proceedings*, 896(1):31–49, 2007.

[46] J. Bar, J. Sempau, J.M. Fernndez-Varea, and F. Salvat. PENELOPE: An algorithm for Monte Carlo simulation of the penetration and energy loss of electrons and positrons in matter. *Nuclear Instruments and Methods in Physics Research Section B: Beam Interactions with Materials and Atoms*, 100(1):31 – 46, 1995.

[47] I. Kawrakow and D.W.O. Rogers. The EGSnrc code system: Monte Carlo simulation of electron and photon transport. Technical Report PIRS-701, 2003.

[48] D.W.O. Rogers. Monte Carlo techniques in radiotherapy. *Physics in Canada*, 58(2):63–70, 2002.

[49] B.R.B. Walters, B. Walters, and I. Kawrakow. BEAMnrc users manual. Technical Report PIRS 509 rev L, 2011.

[50] D.W.O. Rogers, I. Kawrakow, J.P. Seuntjens, B.R.B. Walters, and E. Mainegra-Hing. NRC user codes for EGSnrc. Technical Report PIRS 702 rev C, 2013.

[51] B.R.B. Walters, I. Kawrakow, and D.W.O. Rogers. DOSXYZnrc users manual. Technical Report PIRS 794 rev B, 2005.

[52] J. Wulff, K. Zink, and I. Kawrakow. Efficiency improvements for ion chamber calculations in high energy photon beams. *Medical Physics*, 35:1328–1336, 2008.

[53] J. Seco and F. Verhaegen. *Monte Carlo Techniques in Radiation Therapy*. Imaging in Medical Diagnosis and Therapy. Taylor & Francis Group, 2013.

[54] M. J. Berger. Monte Carlo calculation of the penetration and diffusion of fast charged particles. *Methods Computational Physics*, (1):135–215, 1963.

[55] I. Kawrakow. Accurate condensed history Monte Carlo simulation of electron transport. i. [small-caps egs]nrc, the new [small-caps egs4] version. *Medical Physics*, 27(3):485–498, 2000.

[56] J. Seuntjens and D.W.O Rogers. *Chapter 5 Monte Carlo Applications in Measurement Dosimetry in 'Clinical Dosimetry Measurements in Radiotherapy'*. Medical Physics Publishing (Madison WI), 2009.

[57] F.B. Brown. *Fundamentals of Monte Carlo Particle Transport: Lecture notes for Monte Carlo Course*. Los Alamos National Laboratory.

[58] F. Verhaegen and J. Seuntjens. Monte Carlo modelling of external radiotherapy photon beams. *Physics in Medicine and Biology*, 48(21):R107, 2003.

[59] N. Reynaert, S.C. van der Marck, D.R. Schaart, W. Van der Zee, C. Van Vliet-Vroegindeweij, M. Tomsej, J. Jansen, B. Heijmen, M. Coghe, and C. De Wagter. Monte Carlo treatment planning for photon and electron beams. *Radiation Physics and Chemistry*, 76(4):643 – 686, 2007.

[60] J.M. Larraga-Gutierrez, D. Garcia-Hernandez, O.A. Garcia-Garduno, O.O. Galvan de la Cruz, P. Ballesteros-Zebadua, and K.P. Esparza-Moreno. Evaluation of the gafchromic® EBT2 film for the dosimetry of radiosurgical beams. *Medical Physics*, 39(10):6111–6117, 2012.

[61] I. Kawrakow, E. Mainegra-Hing, and D.W.O. Rogers. EGSnrcMP: the multi-platform environment for EGSnrc. Technical Report PIRS-877, 2006.

[62] International Commission on Radiation Units & Measurements. *ICRU report 37: Stopping powers for electrons and positrons*. 1984.

[63] PTW. Small field dosimetry application guide. Technical report, 2012.

[64] I.J. Chetty, B. Curran, J.E. Cygler, J.J. DeMarco, G. Ezzell, B.A. Faddegon, I. Kawrakow, P.J. Keall, H. Liu, C. Ma, D.W.O. Rogers, J. Seuntjens, D. Sheikh-Bagheri, and J.V. Siebers. Report of the AAPM Task Group No. 105: Issues associated with clinical implementation of Monte Carlo-based photon and electron external beam treatment planning. *Medical Physics*, 34(12):4818, 2007.

[65] E. Chung, H. Bouchard, and J. Seuntjens. Investigation of three radiation detectors for accurate measurement of absorbed dose in nonstandard fields. *Medical Physics*, 37:2404–2413, 2010.

[66] D. Sheikh-Bagheri and D.W.O. Rogers. Sensitivity of megavoltage photon beam Monte Carlo simulations to electron beam and other parameters. *Medical Physics*, 29(3):379, 2002.

[67] K. Aljarrah and C. Linac. Determination of the initial beam parameters in Monte Carlo linac simulation. *Medical Physics*, 4(33):850–858, 2006.

[68] D.A. Low, W.B. Harms, S. Mutic, and J.A. Purdy. A technique for the quantitative evaluation of dose distributions. *Medical physics*, 25(5):656–61, May 1998.

[69] J. Pena, D.M. González-castaño, F. Gómez, and F. Sánchez-doblado. Automatic determination of primary electron beam parameters in Monte Carlo simulation. *Medical Physics*, 3(34):1076–84, 2007.

[70] D.A. Low and J.F. Dempsey. Evaluation of the gamma dose distribution comparison method. *Medical Physics*, 30(9):2455–2464, 2003.

[71] D. Sheikh-Bagheri, D.W. Rogers, C.K. Ross, and J.P. Seuntjens. Comparison of measured and Monte Carlo calculated dose distributions from the NRC linac. *Medical physics*, 27(10):2256–66, October 2000.

[72] D.W. Rogers, B. Walters, and I. Kawrakow. *BEAMnrc Users Manual*. National Research Council of Canada, 2009.

[73] P.R. Almond, P.J. Biggs, B.M. Coursey, W.F. Hanson, M.S. Huq, R. Nath, and D.W.O. Rogers. AAPM's TG-51 protocol for clinical reference dosimetry of high-energy photon and electron beams. *Medical Physics*, 26:1847–1870, 1999.

[74] C. McKerracher and D.I. Thwaites. Assessment of new small-field detectors against standard-field detectors for practical stereotactic beam data acquisition. *Physics in Medicine and Biology*, 44(9):2143, 1999.

[75] X.R. Zhu, J.J. Allen, J. Shi, and W.E. Simon. Total scatter factors and tissue maximum ratios for small radiosurgery fields: Comparison of diode detectors, a parallel-plate ion chamber, and radiographic film. *Medical Physics*, 27(3):472–477, 2000.

[76] F. Sanchez-Doblado, G.H. Hartmann, J. Pena, J.V. Rosell, G. Russiello, and D.M. González-castaño. A new method for output factor determination in MLC shaped narrow beams. *Physica Medica*, 23(2):58 – 66, 2007.

[77] H. Bouchard and J. Seuntjens. Ionization chamber-based reference dosimetry of intensity modulated radiation beams. *Medical Physics*, 31:2454–2465, 2004.

[78] D.M. González-castaño, L. Brualla González, M.A. Gago-Arias, J. Pardo-Montero, F. Gomez, V. Luna-Vega, M. Sanchez, and R. Lobato. A convolution model for obtaining the response of an ionization chamber in static non standard fields. *Medical Physics*, 39:482–491, 2012.

[79] A. Djouguela, D. Harder, R. Kollhoff, A. Rhmann, K. Willborn, and B. Poppe. The dose-area product, a new parameter for the dosimetry of narrow photon beams. *Zeitschrift fur medizinische Physik*, 16:217–227, 2006.

[80] J. Fan, K. Paskalev, L. Wang, L. Jin, J. Li, A. Eldeeb, and C. Ma. Determination of output factors for stereotactic radiosurgery beams. *Medical Physics*, 36:5292–5300, 2009.

[81] B. Hundertmark, E. Sterpin, and T. Mackie. A robust procedure for verifying TomoTherapy Hi-Art source models for small fields. *Physics in Medicine and Biology*, 56:3685–3699, 2011.

[82] D. Sheikh-Bagheri and D.W.O. Rogers. Monte Carlo calculation of nine megavoltage photon beam spectra using the BEAM code. *Medical Physics*, 29(3):391–402, 2002.

[83] C. Coles and J. Yarnold. The IMPORT Trials are Launched (September 2006). *Clinical Oncology*, 18:587–590, 2006.

[84] F. Lacroix, M. Guillot, M. McEwen, L. Gingras, and L. Beaulieu. Extraction of depth-dependent perturbation factors for silicon diodes using a plastic scintillation detector. *Medical Physics*, 38:5441–7, 2011.

[85] E. Yorke, R. Alecu, L. Ding, D. Fontenla, A. Kalend, D. Kaurin, M. E. Matson-McGary, G. Marinello, T. Matzen, A. Saini, J. Shi, W. Simon, T. Zhu, and X. R. Zhu. *AAPM Report 87: Diode in-vivo dosimetry for patients receiving external beam radiotherapy*. AAPM, 2005.

[86] F. Sanchez-Doblado, G.H. Hartmann, J. Pena, J.V. Rosell, G. Russiello, and D.M. González-castaño. A new method for output factor determination in MLC shaped narrow beams. *Physica medica*, 23:58–66, 2007.

[87] T S A Underwood, H C Winter, J D Fenwick, and M A Hill. Modifying detector designs for small field dosimetry. *ESTRO 31 Conference, Barcelona, Spain. Radiother Oncol*, 103(S1):S206, 2012.

[88] C. Martens, C. De Wagter, and W. De Neve. The value of the LA48 linear ion chamber array for characterization of intensity-modulated beams. *Physics in Medicine and Biology*, 46(4):1131, 2001.

[89] J. Renaud, D. Marchington, J. Seuntjens, and A. Sarfehnia. Development of a graphite probe calorimeter for absolute clinical dosimetry. *Medical Physics*, 40(2):020701, 2013.

[90] A.S. Beddar, K.J. Kinsella, A. Ikhlef, and C.H. Sibata. A miniature ldquo;scintillator-fiberoptic-pmt rdquo; detector system for the dosimetry of small fields in stereotactic radiosurgery. *Nuclear Science, IEEE Transactions on*, 48(3):924–928, 2001.

[91] M. Guillot, L. Beaulieu, L. Archambault, S. Beddar, and L. Gingras. A new water-equivalent 2d plastic scintillation detectors array for the dosimetry of megavoltage

energy photon beams in radiation therapy. *Medical Physics*, 38(12):6763–6774, 2011.

[92] J. Morin, D. Beliveau-Nadeau, E. Chung, J. Seuntjens, D. Theriault, L. Archambault, S. Beddar, and L. Beaulieu. A comparative study of small field total scatter factors and dose profiles using plastic scintillation detectors and other stereotactic dosimeters: The case of the cyberknife. *Medical Physics*, 40(1):011719, 2013.